

Copyright

by

Zhiping Yang

2009

The Dissertation Committee for Zhiping Yang
certifies that this is the approved version of the following dissertation:

Fracture, Friction and Granular Simulation

Committee:

Michael P. Marder, Supervisor

Harry L. Swinney

William D. McCormick

Jack B. Swift

K. Ravi-Chandar

Fracture, Friction and Granular Simulation

by

Zhiping Yang, B.Sc.(Honors)

Dissertation

Presented to the Faculty of the Graduate School of

The University of Texas at Austin

in Partial Fulfillment

of the Requirements

for the Degree of

Doctor of Philosophy

The University of Texas at Austin

May 2009

Dedicated to my wife Hongwei and son Steven.

Acknowledgments

I would like to say thanks to many people for their continuous support and encouragement.

First and foremost, I want to thank my lovely wife Hongwei Shi for taking great care of me and also bringing me an adorable son Steven. Her patience and endurance contribute to the making of this thesis significantly.

I also want to thank Dr. Marder for being my supervisor and for his continuous support both academically and financially. His ever smiling face and humorous comments encourage me to take on any challenges ahead of me and have fun doing it.

I'd like to thank Dr. Swinney for overseeing Center for NonLinear Dynamics (CNLD). This is a great research center. I'm honored to be part of it. I have learned a lot from those weekly seminars and group meetings. What maybe more important is the spirit of cooperation, presentation and inter-change of ideas. It certainly has widened my eyes and deepened my understanding of science.

I'd like to thank Dr. Robert Deegan for introducing the low temperature fracture experiment to me. Though his design didn't work out as desired, but I learned many valuable experimental skills from him.

I'd like to thank Dr. Hepeng for bringing me to the numerical study of granular systems. His experience and ideas were the fuels that kept me driven.

I'd like to thank Dr. McCormick, Dr. Swift and Dr. Ravi-Chandar for serving as members of my thesis committee. Their careful inspection and valuable comments made this thesis much more valuable.

I'd like to thank all other members of CNLD for many of their creative ideas and suggestions to my research.

Last but not least, I'd like to thank all the technical personnel on the 3rd floor

of RLM. Especially to Allen for machine grounding my steel frames, to Jack for providing instructions of how to operate machines in the student shop and to Jesse for doing Molecular Beam Epitaxy (MBE) on all the silicon samples that I broke.

ZHIPING YANG

The University of Texas at Austin

May 2009

Fracture, Friction and Granular Simulation

Publication No. _____

Zhiping Yang, Ph.D.

The University of Texas at Austin, 2009

Supervisor: Michael P. Marder

This thesis contains three separate yet closely related topics: fracture, friction and simulation of mechanical response of a confined granular medium. The first two are experimental investigations and the last one is a numerical study.

In the fracture part, I will describe how to break a piece of silicon in a controlled way such that the atomic nature of the fracture process can be revealed in a macroscopic experiment. In the friction part, I will present another experiment using almost exactly the same setup as for the low temperature fracture experiment to study the properties of static friction and explore ideas concerning the origin of friction. In the last part, I will construct a confined granular packing and study how pulses and continuous waves propagate through it. All these three topics are relevant to geophysical science. I sincerely hope that my study can ignite some fresh thinking in that area and help other researchers to design models that can make more precise earthquake predictions.

Contents

Acknowledgments	iv
Abstract	vi
List of Figures	x
Chapter 1 Introduction	1
1.1 Fracture	2
1.1.1 Basics of fracture mechanics	6
1.1.1.1 Three modes of fracture	6
1.1.2 A brief review of linear elastic fracture mechanics	6
1.1.2.1 Pioneer work by Inglis	6
1.1.2.2 Energy balance approach by Griffith	9
1.1.2.3 Critical stress intensity factor approach by Irwin	10
1.1.2.4 Beyond the scope of linear elastic fracture mechanics	11
1.2 Friction	12
1.2.1 A brief history of friction	12
1.2.2 Dynamic aspect of static friction and its origin	16
1.2.3 Purpose of the friction experiment	17
1.3 Granular Simulation	18
1.3.1 Introduction to LAMMPS	22
1.3.2 Force-displacement relation and Hertz contact	22
1.3.3 The attenuation problem and the energy dissipation mechanism	23

1.3.4	The resonant frequency shift problem and earthquake triggering . . .	24
Chapter 2	Fracture	25
2.1	Discrete nature of fracture process	25
2.1.1	Theoretical study of fracture process	26
2.1.2	Numerical study of fracture process	28
2.1.3	Previous experimental study of fracture process at CNLD (Center for NonLinear Dynamics)	36
2.2	Experimental study of crystal silicon fracture at liquid Nitrogen Temperature	41
2.2.1	Motivation	41
2.2.2	Experimental setup	41
2.2.3	Potential drop technique	42
2.2.4	The data acquisition circuit	44
2.2.5	Some major difficulties of this experiment	46
2.2.5.1	Wafer not breaking straight	46
2.2.5.2	Wafer sliding	49
2.2.6	Differential loading to catch velocity gap	52
2.3	Data Analysis and Discussion	53
2.3.1	Data of partial cracks	53
2.3.2	Data of a good room temperature crack	55
2.3.3	Data of a good low temperature crack	57
2.3.4	Velocity gap confirmed	58
2.4	Conclusion	58
Chapter 3	Friction	60
3.1	Introduction	60
3.2	The inclined plane experiment	64
3.3	The friction experiment	65
3.4	Modified rate- and state- friction law	67
3.4.1	Rate- and state- equation and its modification	67
3.5	Using the modified rate- and state- equation to fit our data	73
3.5.1	Step Data	76

3.5.2	Continuous data	77
3.6	Conclusion	79
Chapter 4	Granular Simulation	80
4.1	Preparation of a confined granular system	80
4.1.1	LAMMPS' implementation of the force-displacement relation	80
4.1.2	packing generation and boundary conditions	81
4.2	Static properties of the prepared system	83
4.3	Dynamic properties of the prepared system	83
4.3.1	Pulse mode	83
4.3.1.1	speed of a pulse	87
4.3.1.2	attenuation and total absorbing layer	88
4.3.2	Resonance mode	90
4.4	summary and brief report of ongoing studies	102
Chapter 5	Conclusions	103
Chapter 6	Appendix	104
6.1	Wafer preparation for the fracture experiment	104
6.2	Bug report to LAMMPS admins	105
6.2.1	The input scripts are as following:	109
6.3	Graphs of Relative Increase of Oscillation Intensity	112
Bibliography		117
Vita		125

List of Figures

1.1	Glass cups drop on a concrete floor (photo from the World Wide Web)	3
1.2	Creep of a crack at the face of a dam (photo from the World Wide Web) . . .	3
1.3	Surface of a straight crack (photo courtesy of Robert Deegan)	4
1.4	A wavy crack of silicon (photo courtesy of Robert Deegan)	4
1.5	Thermal energy can destroy the velocity gap and make it possible for a crack to run at any speed. Only when it is largely reduced will the velocity gap be detectable. (Graph adapted from Holland and Marder's paper[35].)	5
1.6	Schematic pictures of a bond-breaking process at zero temperature provided an intuitive argument for the existence of a velocity gap.	7
1.7	Basic modes of fracture	8
1.8	Inglis infinite plate problem	8
1.9	Schematic drawing of a crack propagating from x_0 to x_1	9
1.10	ancient people using logs to reduce friction, This picture is adapted from Duncan Dowson's classic book "History of tribology"[17].	13
1.11	Drawing of Leonardo da Vinci, This picture is adapted from Duncan Dowson's classic book "History of tribology"[17].	13
1.12	inter locking mechanism of friction, This picture is adapted from Duncan Dowson's classic book "History of tribology"[17].	14

1.13	Schematic drawing of Bowden and Tabor's experiment of putting two cylindrical rods into a cross configuration and measuring the contact resistance, which was then compared with the real area of contact from the analytical solution given by Hertz[33, 44] (This graph is adapted from Bowden and Tabor's paper[86].)	15
1.14	Colored areas were the real area of contact, which was much smaller than the apparent contact area (The whole picture was the apparent contact area.). (This photo is adapted from Dieterich and Kilgore's paper[16] .)	16
1.15	Part of a 3-D reconstruction of a static granular packing realized by the X-ray micro-tomography method (This picture is adapted from Patrick's paper[21, 72, 84] .).	20
1.16	Birefringent pattern of a photo-elastic disk was used to infer the internal stress state of every individual disks, which was then assembled to find the contact force network of the whole packing (This photo is adapted from Martin van Hecke's paper[6, 89].).	21
2.1	One-dimensional lattice model used to simulate a dynamic fracture process.(This graph is adapted from Marder and Gross's paper[60].)	27
2.2	Solution of the 1-d lattice model gave the first indication of the existence of a velocity gap. A crack would not propagate even the energy stored in the system was more than the minimum energy required to sustain a running crack based on the Griffith's energy balance criterion, which was known as lattice trapping. For a fast running crack (Started at the up right corner of the graph.), if the energy available to the crack tip gradually decreased towards the Griffith's threshold, a stable solution did not exist for v smaller than 0.4, hence the crack would abruptly come to a stop. This range of velocity where no stable solution existed was then called a velocity gap. (This graph is adapted from Marder and Gross's paper[60].)	29
2.3	Silicon fracture simulated with MEAM, which was then compared with experimental results. (This graph is adapted from Swadener's paper[39].)	32

2.4	Comparison of numerical simulation results[35, 7] and experimental results[42] for silicon fracture. All classical Molecular Dynamics simulations disagree quantitatively with experiment (MEAM, IMSW). The tight binding results of Bernstein and Hess appear to be compatible with experiment.	33
2.5	Snapshot of MD simulation with EDIP (Adapted from Bernstein’s paper) . . .	35
2.6	Comparison of the range of SW potential and EDIP (Adapted from Bernstein’s paper)	36
2.7	Gross’s tensile testing machine, “Whomper” (This graph is adapted from Hauch’s PhD thesis[32].)	37
2.8	Hauch’s sandwich design (This graph is adapted from Hauch’s paper.)	39
2.9	Comparison of experimental results to MD simulation results (This graph is adapted from Hauch’s paper[42].)	40
2.10	MD simulation of silicon crack including thermal energy (This picture is adapted from Holland’s paper[35].)	40
2.11	3-D block diagram and 2-D side view of the friction holding system. A silicon sample sits on top of a steel frame whose middle portion is milled out. Two pressure blocks each have two feet; one sits on top of the steel frame and the other on top of the silicon sample right along the edge of the middle window of the frame. Two C-shape clamps each having a pair of bellows complete the force loop. This works much the same way as we use our hand to grab a burger; the C-shape clamp acts as a hand and the steel frame, silicon sample and the pressure block are the contents of the special burger.	43
2.12	Potential map and current flow through a partially cracked silicon wafer (Numerical solution of a boundary condition partial differential equation given by Matlab.)	44
2.13	The relationship between the potential difference of the inner two tabs and crack length under constant current assumption. Each dot represents a solution for a particular crack length and the line is just an interpolation to show the general trend of the data.	45

2.14	Data acquisition circuit for the fracture experiment. The resistance of the wafer is represented by the resistor between A and B. With a constant current source on the order of 1 mA, the potential difference between A and B is measured. Channel 1 picks up the voltage reading directly while channel 2 takes the same voltage data but makes an analog differentiation before the data is recorded.	46
2.15	It is demonstrated through calculations within software package franc2d that if only a few percent of the elastic energy goes into Mode II, the crack will deviate from its original path, which is not desirable in our experiment. . . .	47
2.16	Robert Deegan's three-hole frame design. This design would work if everything functioned ideally, but the reality is that the world we live in is far from ideal. So, the two piezoelectric transducers can be misaligned with respect to each other and not perfectly perpendicular to the major axis of the frame. The frame is very vulnerable to any tiny amount of shear force. So in practice, this design does not work.	49
2.17	Boxed low temperature environment surrounding Whomper, The upper sub-figure is a real photo of the setup; the lower sub-figure is a schematic drawing of the essential components. A stepper motor is connected to the left-most steel rod (orange), a steel bar redistributes the load to two smaller rods (blue) which in turn act upon the steel frame. The steel frame is still the platform for conducting the fracture experiment. A symmetrical design refocuses all the load back to the right most steel bar (orange), which is then fixed to a stationary point on the wall of the outer aluminum structure. Since the stepper motor is also fixed to the outer aluminum structure on a symmetrical point of the opposite wall, the force loop is completed. This design has the advantage of aligning itself and displays much stronger resistance to shear forces than the design in Figure 2.16.	50
2.18	Schematic drawing of mode I crack and quantities used for calculating energy release rate	51
2.19	Bellow for differential loading	54

2.20	Length and velocity records of cracks moving in jerky fashion (partial cracks). Note that the velocity never exceeds 1 km/sec and never reaches a steady state. These experimental signals are characteristic of misaligned samples that leave behind rough fracture surfaces.	55
2.21	A good room temperature break; the crack reaches a velocity over 1 km/sec and holds it for several microseconds. The distance is calibrated by noting the final position of the crack tip after the experiment is completed.	56
2.22	A good low temperature break.	57
2.23	Comparison of the arrests of cracks at room temperature and liquid nitrogen temperature under comparable energy release rates reveals the existence of a velocity gap.	58
3.1	Common understanding of friction (The lower portion of this graph is from World Wide Web.)	61
3.2	Slip-stick motion (This graph is adapted from Cochard's paper[1].)	62
3.3	Rough surfaces in contact as a conventional picture of friction	63
3.4	Inclined plane experiment between a polished silicon wafer and a machine-ground steel surface.	64
3.5	Schematic diagram of the experimental setup of friction. The four rods in blue color are the aluminum holders for the two pairs of inductive sensors, which are machined to exactly the same specification.	66
3.6	The red and gray thin curves were individual readings from each inductive sensor and they varied a lot during the process of inflating or deflating the bellows, but their sum stayed very close to zero as more clearly indicated by the sub-figure, which is a magnified view of the sum of these two curves. . . .	68
3.7	One set of continuous data under the normal force of 120 N. The green curve is the prediction of conventional friction, the black curve is the prediction of the modified rate- and state- friction law treating D_c as a material constant while the red curve is the prediction of the same modified rate- and state-friction law but allowing D_c to vary as a function of normal force.	70

3.8	I sat the silicon sample on top of the steel frame and waited for four different lengths of time before conducting exactly the same experiment. The results bear no indication of aging except for a slight difference between data obtained after waiting for 30 minutes and the rest of them which were obtained after waiting for much longer time. All the rest of my friction experiment waited for more than 24 hours, so aging should not present itself in any of my other data sets.	71
3.9	Step data; The normal force for this data set is 180 N and it was held fixed throughout the experiment.	74
3.10	Slipping of the wafer as the boundary condition was fixed	75
3.11	Illustration of the quantities measured for the friction experiment	76
3.12	Continuous data from experiments where the normal force was constant and shear force increases slowly and linearly. The green curve shows the sample response that would be expected from the conventional theory of static friction. The sample would stretch with the frame up to the limit of static friction and then slide freely. Instead, as shown by the experimental data in blue, the sample always moves less than predicted. I provide two fits to the data based on the modified rate and state friction law. The first of them (black) treats the asperity length D_c as a constant. The second of them (red) allows D_c to vary linearly with normal force. All parameters of the model are held constant across all six panels.	78
4.1	A snapshot of the system and its contact force network	84
4.2	Probability distribution curve	85
4.3	Shape of the cosine pulse	85
4.4	A snapshot of a pulse propagating through the system, What point in time? .	86
4.5	Horizontally averaged y-component velocities at equal time interval (colors to indicate different instants of time.)	87
4.6	Hysteresis loop	89
4.7	sine wave transforms to triangular wave	89
4.8	With total absorbing layer (colors to indicate different instants of time.) . . .	91
4.9	Without total absorbing layer (colors to indicate different instants of time.) .	92

4.10	Horizontal average of y-velocity at resonant condition	94
4.11	Fit the force on the bottom wall	95
4.12	resonance curves at 300 kPa	96
4.13	resonance curves at 3.1 MPa	97
4.14	resonance curve at 11.9 MPa	98
4.15	Frequency shift as a function of amplitudes	99
4.16	Relative increase of oscillation intensity of the whole contact force network .	100
4.17	Oscillation intensity comparison of driving amplitude 3, 10, 30, 100 to 1 . . .	101
6.1	Two identical balls collide	105
6.2	y-force on ball 2 with radius 2	106
6.3	y-force on ball 2 with radius 3	107
6.4	collision simulated in LAMMPS (2-d and 3-d)	110
6.5	A3/A1	113
6.6	A10/A1	114
6.7	A30/A1	115
6.8	A100/A1	116

Chapter 1

Introduction

To start my thesis, I would like to quote Richard Feynman’s comment on what might be the most important scientific discovery of human being[20].

“If, in some cataclysm, all of scientific knowledge were to be destroyed, and only one sentence passed on to the next generations of creatures, what statement would contain the most information in the fewest words? I believe it is the atomic hypothesis (or the atomic fact, or whatever you wish to call it) that all things are made of atoms—little particles that move around in perpetual motion, attracting each other when they are a little distance apart, but repelling upon being squeezed into one another. In that one sentence, you will see, there is an enormous amount of information about the world, if just a little imagination and thinking are applied.”

There is little doubt that the discovery of atoms and the laws governing the dynamics in the microscopic world - quantum mechanics are the most significant achievement of human intelligence. But the microscopic world is so “small” that most of the practical engineering problems start by making the continuum assumption. To many, the atomic discontinuity is just “theoretical”. Out of sight, out of mind.

In this thesis, I will present three separate yet closely related topics that are more or less concerned the effects of atomic discreteness reflected on a macroscopic scale. The three topics are: fracture, friction and granular simulation. In the fracture part, I will describe how to break a piece of silicon in a controlled way such that the atomic nature of the fracture

process can be revealed in a macroscopic experiment. In the friction part, I will present another experiment using almost exactly the same setup as for the low temperature fracture experiment to study the properties of static friction and explore ideas concerning the origin of friction. In the last part, I will present a numerical study of mechanical properties of a confined granular medium.

1.1 Fracture

Fracture is a fascinating topic. Everything breaks, yet things can break in dramatically different ways: some break within a fraction of a second as when glass cups drop on a concrete floor. (figure 1.1), while others can take years, such as the creep of a crack at the face of a dam. (figure 1.2). Some break straight and leave mirror-like surface. One nice example is illustrated in figure 1.3, which is a high resolution image of the crack surface from a straight crack sample (courtesy of Robert Deegan). Others can break in a wavy manner with rich surface features. Dipping a pre-notched hot silicon strip into a bath of cold water can do the trick. Figure 1.4 shows that silicon can be broken in a wavy manner even it was exactly the same material as for the straight crack.[76] (courtesy of Robert Deegan).

In the first part of this thesis, I will describe the searching for an interesting dynamic feature of brittle fracture, namely a velocity gap, which was predicted by Marder in theoretical arguments [61] as well as numerical simulations [35, 34]. The theoretical argument started with an analytical solution of a mass-spring lattice model for Mode I fracture first proposed by Slepian [81]. The solution of the lattice model indicated that the crack speed will be unstable within a certain range (ranging from zero to about 20% of Rayleigh wave speed). That is, you can not have a crack running steadily at that speed. The physical reason for that has to do with the very nature of the fracturing process, which is the successive breaking of inter-atomic bonds. Referring to figure 1.6, suppose at some moment the system is in configuration (a), right after that the bond between the green atom and the atom to its lower left breaks as in (b). Then, the system evolves from (c) to (e) while it prepares for the breaking of the next bond, which is indicated in (f). The intuitive argument is that the process from (c) to (e) can not take too long, otherwise the energy concentrated at the crack tip will be dissipated through vibrations (sound) and the breaking of the next bond



Figure 1.1: Glass cups drop on a concrete floor (photo from the World Wide Web)

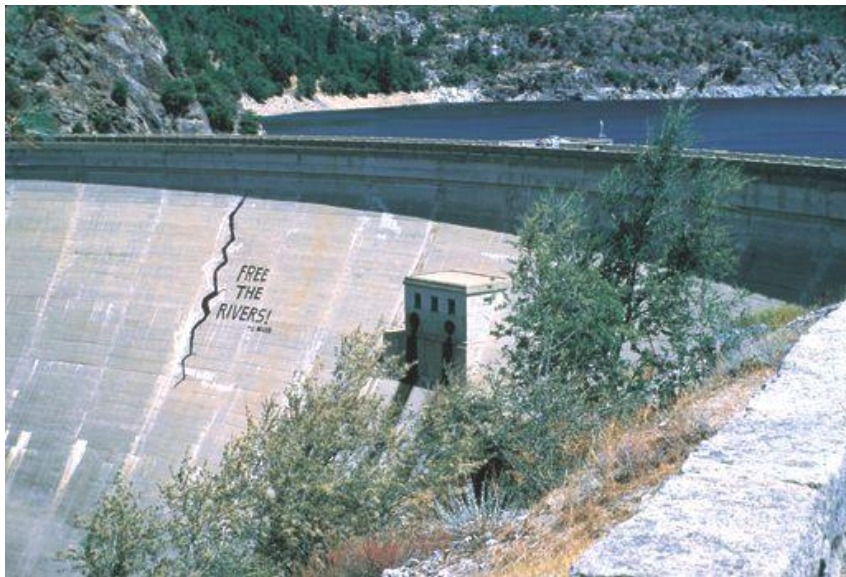


Figure 1.2: Creep of a crack at the face of a dam (photo from the World Wide Web)

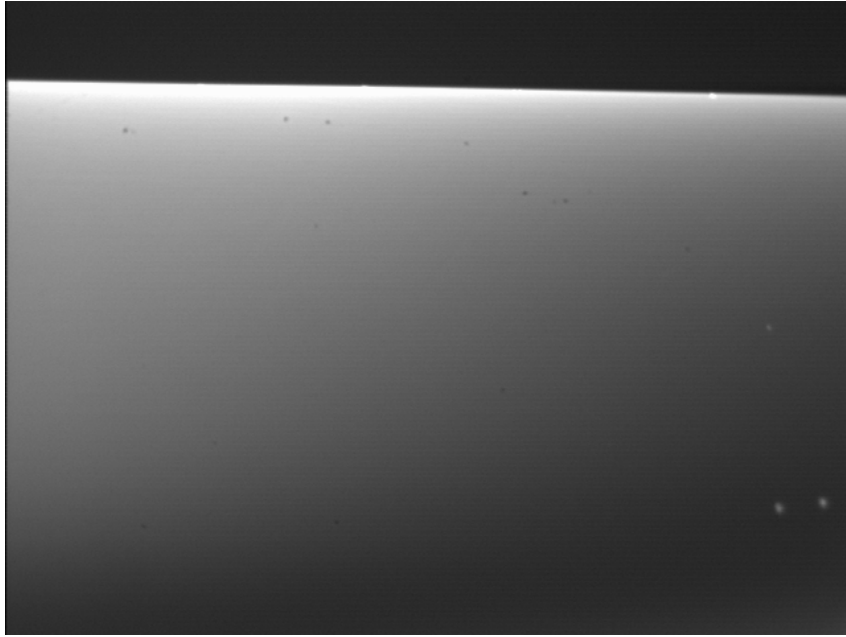


Figure 1.3: Surface of a straight crack (photo courtesy of Robert Deegan)

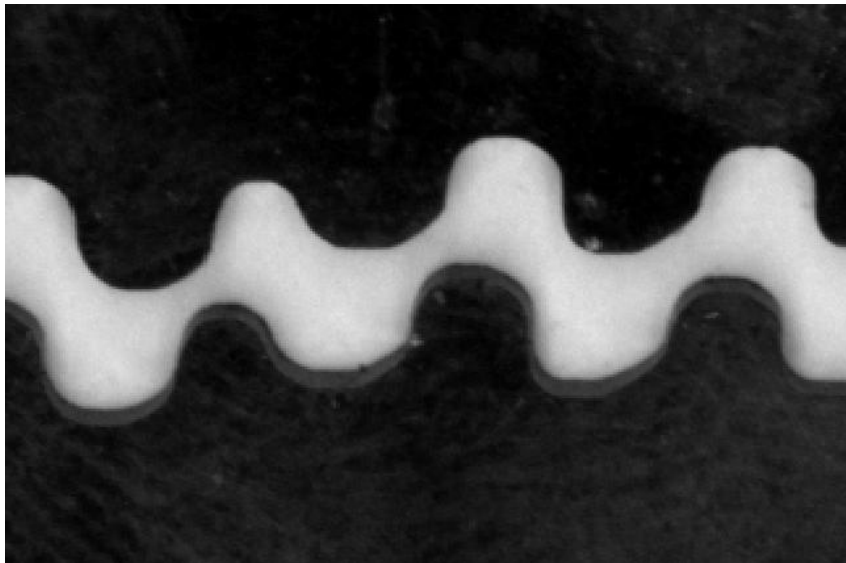


Figure 1.4: A wavy crack of silicon (photo courtesy of Robert Deegan)

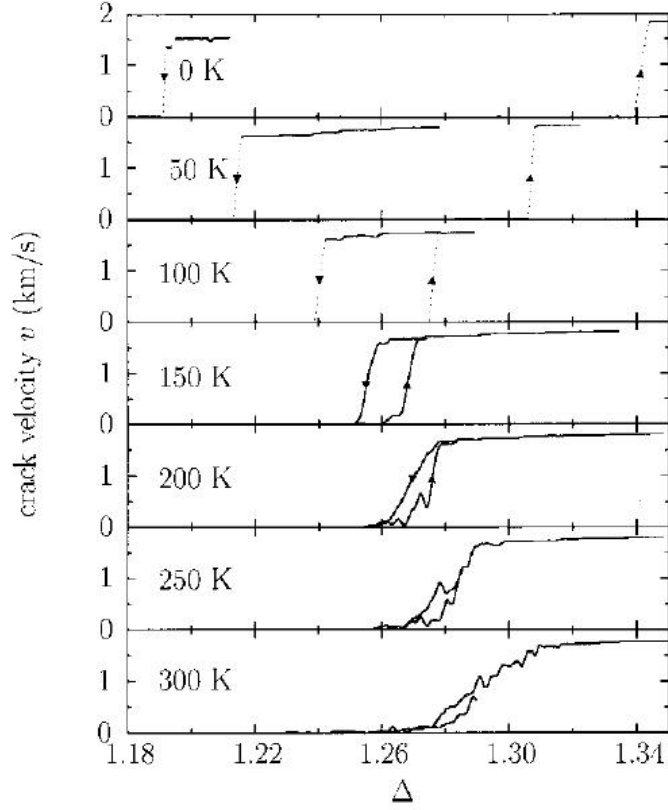


Figure 1.5: Thermal energy can destroy the velocity gap and make it possible for a crack to run at any speed. Only when it is largely reduced will the velocity gap be detectable. (Graph adapted from Holland and Marder’s paper[35].)

could be delayed forever. That also means the crack speed can not be lower than a critical value otherwise the crack will be unstable. The critical value is then called the velocity gap.

The intuitive argument above did not take thermal energy into account, but random thermal fluctuations are able to break bonds. A fracture process due to thermal agitation is also known as creep. For any non-zero temperature (absolute scale), thermal fluctuations will always be present, which is also why I have to conduct the silicon fracture experiment at temperatures less than 100 Kelvin. This conclusion was based on a state-of-art MD simulation of silicon fracture at non-zero temperatures by Holland and Marder[35]. Figure 1.5 represents their main result.

Effort was put to the search for this elusive velocity gap[29, 32, 23] since we physicists

know that any theoretical prediction, no matter how intuitively sound it is, has limited value if it is not backed up by solid experimental evidence.

But, before I go to the details of the experiment, let me first review some of the basics of fracture mechanics.

1.1.1 Basics of fracture mechanics

1.1.1.1 Three modes of fracture

The first thing to know about fracture is that there are three modes of fracture, linearly independent, and any fracture can be a linear superposition of them.[3, 78] They are named Mode I, Mode II and Mode III. Mode I is also known as the opening mode, where the direction of the applied external force is in the same plane as the material and perpendicular to the direction of crack. My experimental study of silicon fracture is done exclusively in this mode. The other two modes are: sliding mode (mode II) and tearing mode (mode III). A graphical illustration of the basic modes of fracture can be found in figure 1.7.

The reason that I chose mode I for my study is that it is the most “clean” mode. Friction between the two crack surfaces does not concern me in that mode of fracture as compared to the other two modes. Also, a numerical study with a matching condition was done by Holland[34, 35] and Marder and can be used for direct comparison.

1.1.2 A brief review of linear elastic fracture mechanics

1.1.2.1 Pioneer work by Inglis

The first attempt to quantify the effect of stress concentration due to a crack-like defect within an elastic body was carried out by C. E. Inglis[37] in 1913. He studied the stress distribution around an elliptical hole in an infinitely large linear elastic plate loaded at its outer boundaries (illustrated in figure 1.8).

By demanding the two semi-axis to satisfy $b \ll a$, the elliptical hole mimics a crack. He showed that the stress maximum at point A (point A is on the edge of the ellipse and directly ahead of the major axis) is given by

$$\sigma_A = \sigma(1 + \frac{2a}{b}) \tag{1.1}$$

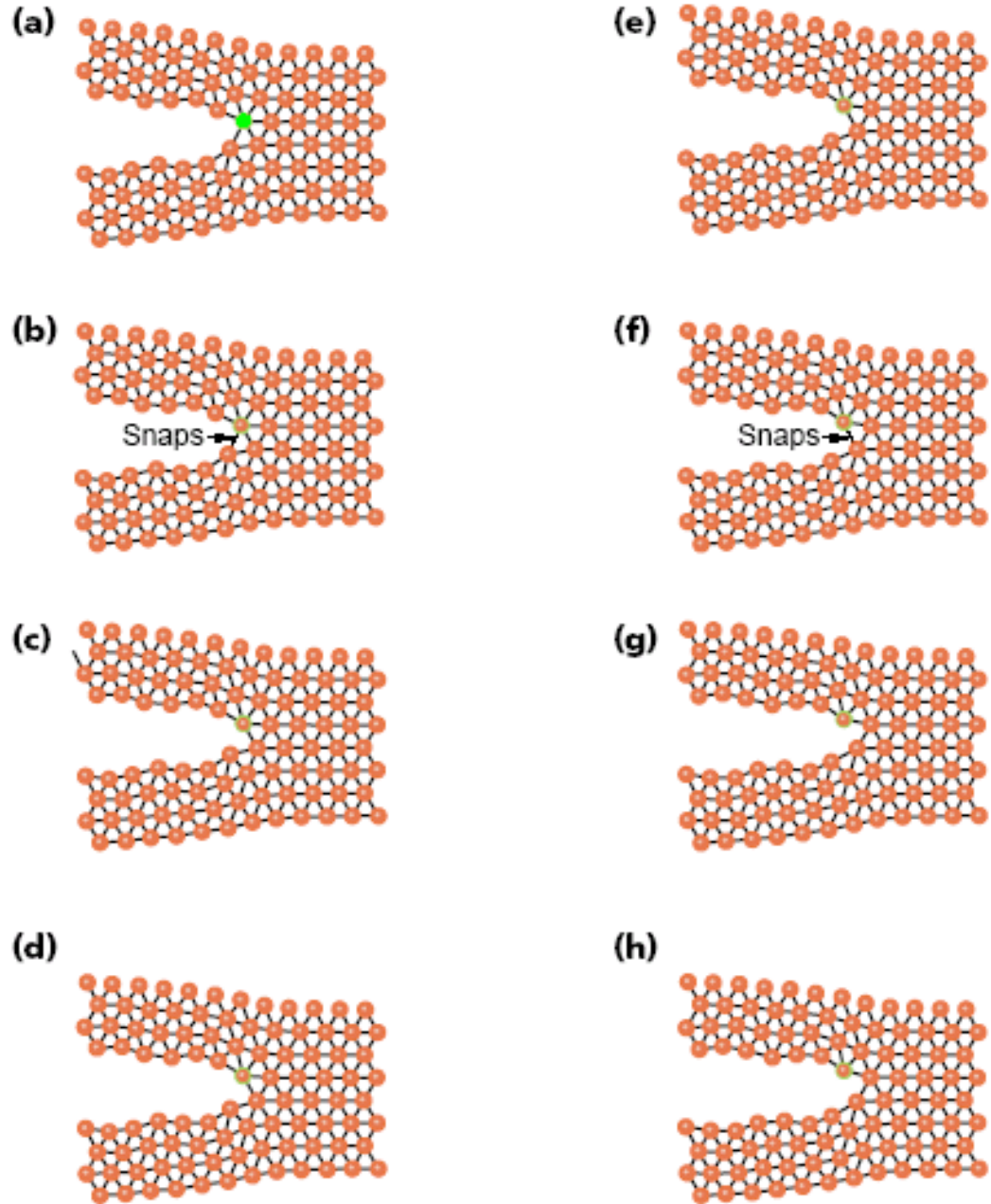


Figure 1.6: Schematic pictures of a bond-breaking process at zero temperature provided an intuitive argument for the existence of a velocity gap.

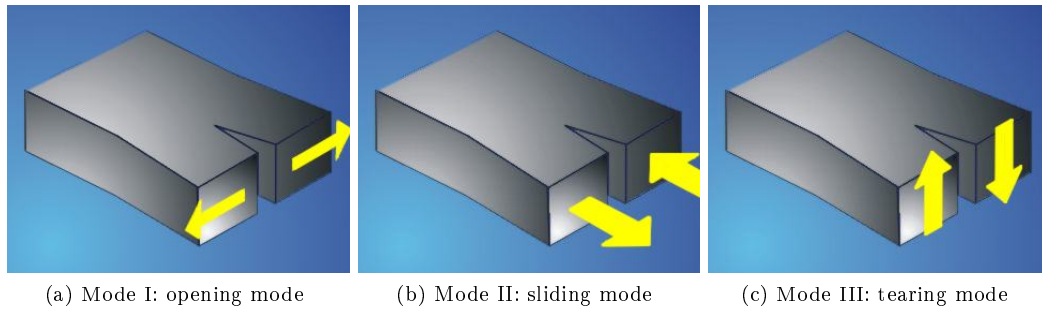


Figure 1.7: Basic modes of fracture

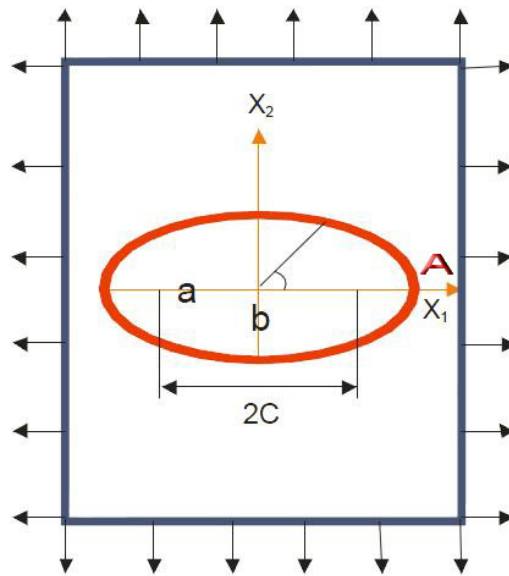


Figure 1.8: Inglis infinite plate problem

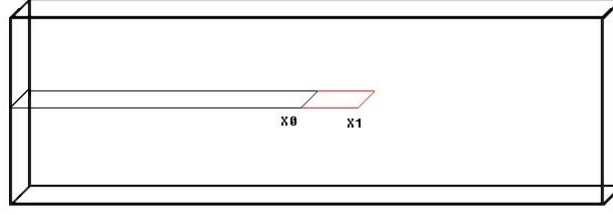


Figure 1.9: Schematic drawing of a crack propagating from x_0 to x_1

Obviously, there is a singularity for stress at point A if b approaches zero and a remains finite. That is of course based on the assumption that the plate is infinitely continuous, which is incorrect for any real material. But, the continuum assumption is so fundamental for any mathematical analysis of this kind, it became a basic assumption for the whole fracture mechanics discipline.

1.1.2.2 Energy balance approach by Griffith

When a crack propagates, new surfaces are created. Surface energy are always positive. Otherwise, the material will spontaneously break into pieces to minimize its total energy. This is also why bubbles are always spherical. They minimize their energy by minimizing the surface. Thus, external energy must be supplied to compensate for the energy cost of these new fracture surfaces.

Based on the energy balance argument, Griffith [27, 28] provided a criterion for the minimum energy release rate required to make a crack propagate in the 1920s.

Referring to a schematic drawing of a propagating crack in figure 1.9, suppose there is a crack front originally at some position x_0 , as it moves to x_1 , two new surfaces are created.

The energy cost of creating these two surfaces is:

$$E = 2\Gamma(x_1 - x_0)t \quad (1.2)$$

where Γ is the surface energy density, t is the thickness of the material.

So, the energy release rate is given by eq. (1.2):

$$\frac{dE}{dl} = \lim_{x1 \rightarrow x0} \frac{\delta E}{\delta(x1 - x0)} = 2\Gamma t \quad (1.3)$$

Of course, the energy release rate calculated this way only provides the absolute minimum energy required to kick off a crack. It certainly does not guarantee that once this minimum energy requirement is met, the crack will have to propagate, and usually it won't. This also leads to a fairly interesting puzzle mentioned in Marder's "condensed matter physics" textbook ([64], page 344). There he argues that, if only surface energy was concerned (which he estimated $\Gamma = 1J/m^2$ for rocks), all rocks higher than 1.4 cm are unstable due to gravitational potential energy. In reality, mountains several kilometers high can stand for millions of years. So, what was missing in this simple argument?

Griffith resolved this puzzle. He was actually the first one to perform a series of fracture experiments on glass fibers and metal bars of different lengths and cross-sections in order to find out the relation between atomic bonding strength and fracture strength of materials. He eventually came to the conclusion that it was not the atomic bonding strength but rather the maximum size of defects that determined the fracture strength of the material.

The key to the puzzle is that there is an energy barrier, a very high energy mountain to overcome in order to get a crack initiated. As I will explain in detail later on, the same crack tip initiation problem caused some technical difficulties for my experimental study of silicon fracture, too.

1.1.2.3 Critical stress intensity factor approach by Irwin

Some 30 years after Griffith's energy balance criteria for crack propagation, Irwin[38] in the Naval Research Lab studied the stress distribution around a crack tip. He found that all stress distributions around a crack tip share a universal functional form as given by the formula below

$$\frac{K}{\sqrt{2\pi r}} f(\theta) \quad (1.4)$$

That is, for any given static load, the leading term in the expansion of stress dis-

tribution in the vicinity of a crack tip will always be a constant (K) divided by the square root of the distance to the crack tip times a function of angle dependence. The value of K is determined by the geometry as well as the loading. What really makes this formula so valuable is the fact that there is a load and geometry independent material constant K_{Ic} , which can be experimentally determined under well controlled external conditions, I indicates that it is for mode I and the subscript c stands for critical. For $K > K_c$ the crack tip is supposed to propagate forward. So, researchers can measure the values of those critical stress intensity factors for many standard materials and publish them. Engineers can then calculate the stress intensity factor for the particular shape and size they want to construct and compare it to the critical stress intensity factor of the material desired. If the value of the stress intensity factor is greater than the critical one, the structure is bound to fail, otherwise, it is safe to use (with proper safety margin).

Irwin then proved that this propagation criteria was equivalent to the energy release rate criteria given by Griffith in equation 1.5, which is close to the relation between force and energy in Newtonian mechanics.

$$G = \beta \frac{K^2}{E} \quad (1.5)$$

Where $\beta=1$ for plane stress and $\beta = 1 - \nu^2$ for plane strain, ν is the Poisson ratio and E is the Young's modulus.¹

1.1.2.4 Beyond the scope of linear elastic fracture mechanics

Since 1950s, Linear Elastic Fracture Mechanics (LEFM) become a mature discipline and research went beyond the linear assumption. Fatigue crack growth, elastic-plastic fracture mechanics, dynamic fracture mechanics and creep and visco-elastic fracture[22] are just a few of the major branches in fracture mechanics and the discussion of them is beyond the scope of this thesis.

¹Plane stress is a condition when the third dimension is much smaller than the other two and plane strain is the opposite extreme.

1.2 Friction

Like fracture, friction is another ubiquitous phenomenon. We can not live without it, yet we lose billions of dollars because of it. We have been studying it since the dawn of modern science, yet some of its fundamental issues are still actively debated in today's scientific literature[26, 47, 24, 67, 79]. In the second part of the thesis I will describe an experiment of dry static friction between two hard surfaces. The purpose of it was originally to troubleshoot the setup for the low temperature fracture experiment, but the result turned out to be valuable on its own. Basically, I found that for shear force much less than the static threshold $\mu_s N$ (where μ_s is the static friction coefficient and N is the normal force), two surfaces will experience a reproducible relative sliding before they became locked into each other. This finding inspired us to re-exam the existing phenomenological theory regarding the origin of friction, namely the rate- and state- friction law.

1.2.1 A brief history of friction

Ancient people accumulated enough empirical knowledge about friction that they were able to apply it in constructing many of the monumental constructions that still puzzle many of today's engineers. The Great Pyramid in Egypt and the Great Wall in China are just two outstanding examples of them. Figure 1.10 shows an example of how ancient people used logs to reduce friction while moving huge stone monument.

The first scientific work on friction is usually attributed to Leonardo da Vinci (1452-1519). He probably did some experiments to study the relationship between the magnitude of a frictional force and the apparent contact area. A good indication of that is some of his remaining hand-drawings, one of which is shown in figure 1.11. This is truly genius considering that it was nearly 200 years before Newton wrote down his equation of motion.

Leonardo da Vinci might well be puzzled to find out that the contact area has very little influence on the amount of frictional force. An intuitive picture of friction he likely had in his mind was more or less like that shown in figure 1.12. Based on this picture, it is easy to believe that the frictional force should be linearly proportional to the contact area, while nature clearly disagrees with our intuitive.

The puzzle of the contact area remains a mystery until Bowden and Tabor[86] pro-

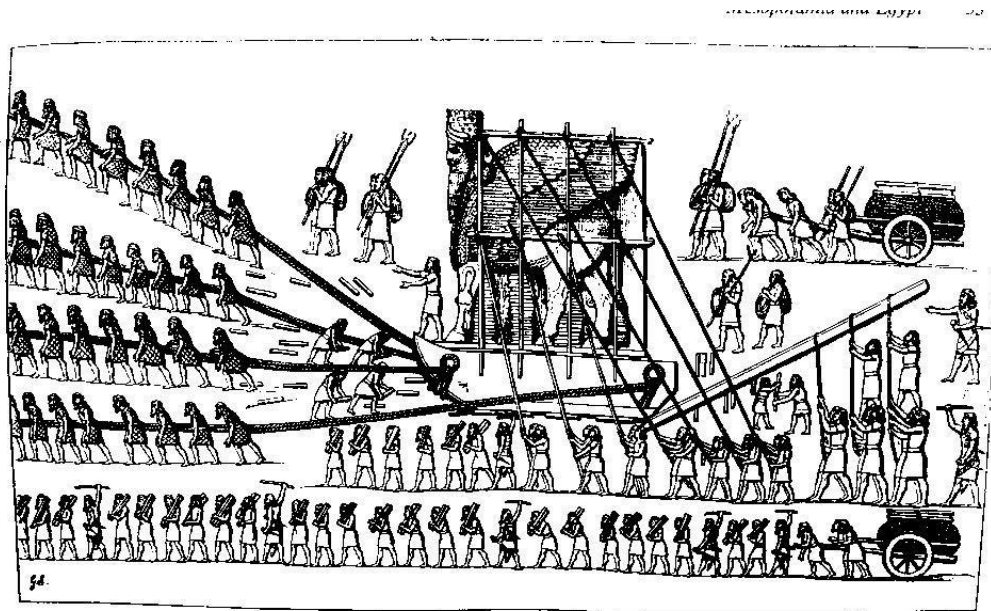


Figure 1.10: ancient people using logs to reduce friction, This picture is adapted from Duncan Dowson's classic book "History of tribology"[17].



Figure 1.11: Drawing of Leonardo da Vinci, This picture is adapted from Duncan Dowson's classic book "History of tribology"[17].

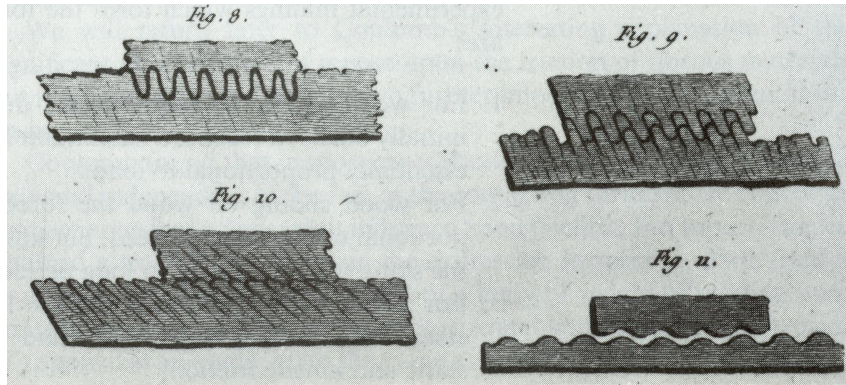


Figure 1.12: inter locking mechanism of friction, This picture is adapted from Duncan Dowson's classic book "History of tribology"[17].

posed in the 1930s-1940s that the real contact area is only a small fraction of the apparent contact area and the size of the real contact area is proportion to the normal load. The experimental method they used was to measure the conductance between two metal parts in contact. First, they put two cylindrical metal bars in cross contact as shown in figure 1.13. The contact area inferred from this setup agreed well with the theoretical calculation based on Hertz contact theory [33, 44] . Then, they put two flat surfaces in contact, the area of contact thus inferred was much less than the apparent contact area. So, they concluded as I quote "The flat surfaces are held apart by small surface irregularities which form bridges of an essentially metallic nature. These bridges flow under the applied pressure or their number increases until their total cross-section is sufficient to enable them to support the applied load."

Bowden and Tabor's idea about surface irregularities and bridges supporting load are further confirmed by direct measurements of the real contact area. An optical means of measuring the real contact area developed by Dieterich and Kilgore[16] works like this: Two transparent flat objects are put in contact and a beam of monochromatic light passes through them. Light is scattered by the rough non-contacting parts of the surface, but transmitted through the real contacts. So, if Bowden and Tabor were right, then most of the film should be dark while only a few scattered spots are visible. Figure 1.14 was one of the resultant photos. Obviously, it looked just as predicted.

Bowden and Tabor's explanation is now widely accepted as the canonical picture

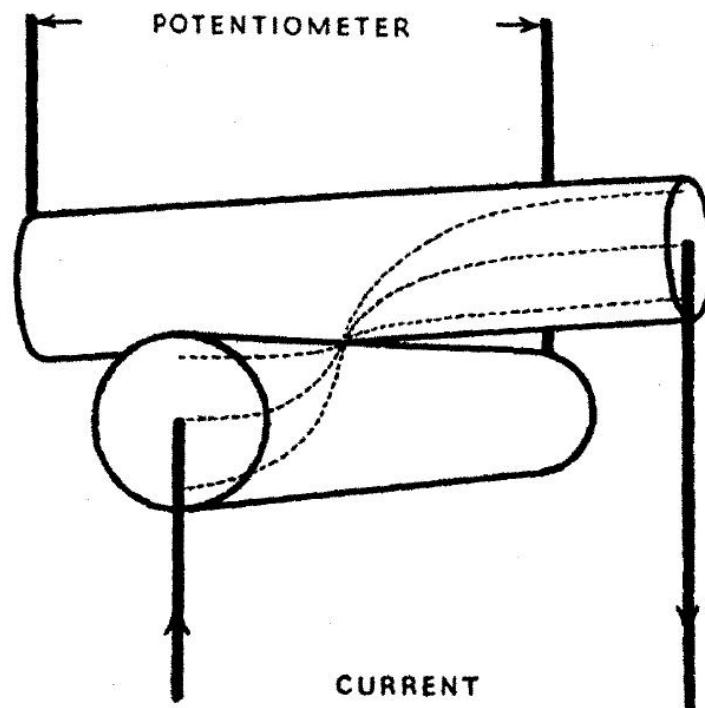


Figure 1.13: Schematic drawing of Bowden and Tabor's experiment of putting two cylindrical rods into a cross configuration and measuring the contact resistance, which was then compared with the real area of contact from the analytical solution given by Hertz[33, 44] (This graph is adapted from Bowden and Tabor's paper[86].)

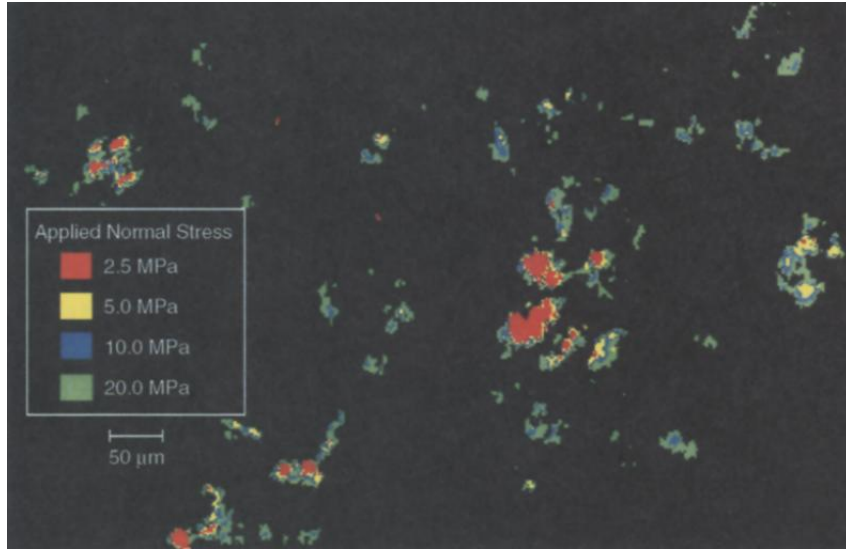


Figure 1.14: Colored areas were the real area of contact, which was much smaller than the apparent contact area (The whole picture was the apparent contact area.). (This photo is adapted from Dieterich and Kilgore’s paper[16] .)

of friction, but it remains a macroscopic theory, a statistical average of multi-asperities; hence it is unable to account for dynamics on the single asperity level and address how friction originated from the atomic length-scale. There are basically three different theoretical approaches to this problem[65, 52, 88, 67]:

1. Phenomenological rate- and state- models[77, 9, 16, 73];
2. Large scale molecular dynamics simulations[87, 8, 43, 70];
3. Minimalistic models[85, 57, 91, 50].

In this thesis I will concentrate on the first approach.

1.2.2 Dynamic aspect of static friction and its origin

Another puzzling aspect of friction is that a frictional force slowly grows with time, also known as “aging”[14, 46]. To fit that into Bowden and Tabor’s picture, you have to imagine that the plastic flow is a very slow process and keeps going even the load has long been stabilized. What is also known is that velocity will destroy the aging history and rejuvenate

the contact[9]. This led Dieterich, Rice and Ruina to propose a phenomenological model that contained a state variable to describe the population of asperities and a rate dependent dynamic equation to describe the dependence of the friction coefficient on the relative velocity. Equation (1.6) is the original form of the rate- and state- equation they proposed.

$$\mu = \mu_0 + A \ln(1 + \frac{v}{v^*}) + B \ln(1 + \frac{\theta}{\theta^*}) \quad (1.6)$$

In its original form, Dieterich, Rice and Ruina kept a static coefficient of friction μ_0 without raising too much doubt about its physical meaning. Basically, it means that for a brand new contact at zero velocity, there is a residual shear resistance, the origin of which is believed to be the cohesive force between atoms of the real contacts. But, what I found in my experiment was that the value of μ_0 was negligibly small and the origin of an apparently nonzero μ_0 could always be traced to a tiny sliding between the two surfaces before they locked into each other and became motionless. The operational regime of my experiment was well within the conventional range of static friction, yet the static friction only appeared by growing from zero to $\mu_0 N$ by means of sliding the two interfaces a tiny distance. We interpreted this as a dynamical origin of static friction ($\mu_0 N$) and we incorporated it into the rate- and state- equation by removing the constant μ_0 and proposing a new functional form of the state variable. The physical picture we had was fairly close to the interlocking process imagined by Coulomb, except that the density of asperities was much lower (to reflect the fact that it is the real contact area instead of the apparent one that supports the load) and it was rate dependent.

1.2.3 Purpose of the friction experiment

The original purpose of the friction experiment was to find out how much the wafer slipped before it cracked in low temperature fracture experiments.

In room temperature fracture experiments, Jens Hauch[42] used super glue to fix the wafer onto the steel frame, and he was able to compensate for the yield of the glue as the frame was stretched. This mechanism wouldn't work for the low temperature fracture experiment because many glues would eventually lose their adhesive power when cooled down. Even if a working glue could be found, it was still virtually impossible to apply the

glue after everything was cooled down. And if you glue them together at room temperature first, the thermal contraction between silicon and steel were so much different that that alone could break the wafer way before the temperature was cold enough to do the experiment. So, Robert Deegan came up with the idea of using friction as the gripping mechanism. He proposed to have all necessary parts cooled down first and then apply a strong enough normal force through a pair of steel blocks to hold the wafer fixed onto the frame. The trick was that the wafer sat loosely on top of the frame while cooling down, which avoided the thermal contraction problem completely. There was a problem in this design however in assuming that the wafer would not slide if a small shear force were to be applied. Based on the conventional knowledge of friction, it was indeed correct to believe that no motion was possible if a shear force less than a certain threshold was applied. But, after breaking a few pieces of wafer, it became puzzling that all of them broke at much higher energy release rate than those of room temperature experiments, while they were expected to be lower.

After careful inspection, it was found that the silicon wafer was sliding on top of the steel frame while the frame was stretched. But, this was not supposed to happen when a strong enough normal was applied based on conventional understanding of static friction. So, a review of the current understanding of static friction was presented in the introduction of the second part of this thesis. Armed with results from my experiment, Marder and I proposed a modification to the standard rate- and state- friction law, which unified the understanding of static and dynamic friction and provided a more realistic physical origin of friction.

1.3 Granular Simulation

Granular materials can be found everywhere around us, such as a pile of sand, a jar of marbles or just a bag of candies. Most of these granular systems are static due to the fact that the interaction between each pair of their constitutive particles are non-conservative. So, either you continuously pump energy into the system (for example, by shaking or rotating the containers) or the system will quickly dissipate all of its kinetic energy and become static. Most of these static granular systems are more or less confined due to the boundaries of their containers or just the weight of the grains on top of them.

To study such a confined granular system, field and laboratory experiments are conducted. Quantities that are commonly measured are usually macroscopic, such as the force acting upon the surface of a piezo-electric transducer or the time it takes for a pulse to travel certain distance (or reflect from a boundary).

Macroscopic quantities are limited in the sense that they are the results of averaging in spacial or temporal directions, but sometime it is the inhomogeneities that are the subjects of interest. So, different experimental methods are implemented to measure microscopic quantities.

X-ray micro-tomography[21, 72, 84] can be used to measure exact position of every particle in a static granular packing, Once that information is obtained, many different characteristic parameters can be calculated, such as the pair correlation function, radial distribution function and contact numbers. Figure 1.15 is a partial reconstruction of the initial packing by the X-ray micro-tomography method.

Another commonly used experimental method to visualize the micro-structure of a static granular packing is the photo-elastic disk method[6, 89]. It is a 2-D system with confined transparent disks which would display unique birefringent patterns depending on the contact forces when imaged through a pair of crossed circular polarizers. By solving an inverse problem of those patterns, Majmudar and Behringer were able to find the normal as well as tangential forces between each pair of contacting disks. Once that information was obtained, it would then be possible to study the contact force distribution or contact force network in different loading conditions, such as bi-axial compression or shear. Figure 1.16 illustrates a typical birefringent pattern of a photo-elastic disk in contact with three neighbors.

An obvious disadvantage of those experimental methods is that they can only deal with static packings, but many interesting features of a granular system are dynamic. Fortunately, there is now a completely different approach to the study of a confined granular system especially for studying dynamic quantities and quantities defined on the microscopic length scale, namely computer simulations.

In the last part of my thesis, I will describe how to apply a general purpose MD (molecular dynamic) code (LAMMPS) to study the motions of particles in a confined granular system. Two major subjects are extensively studied:

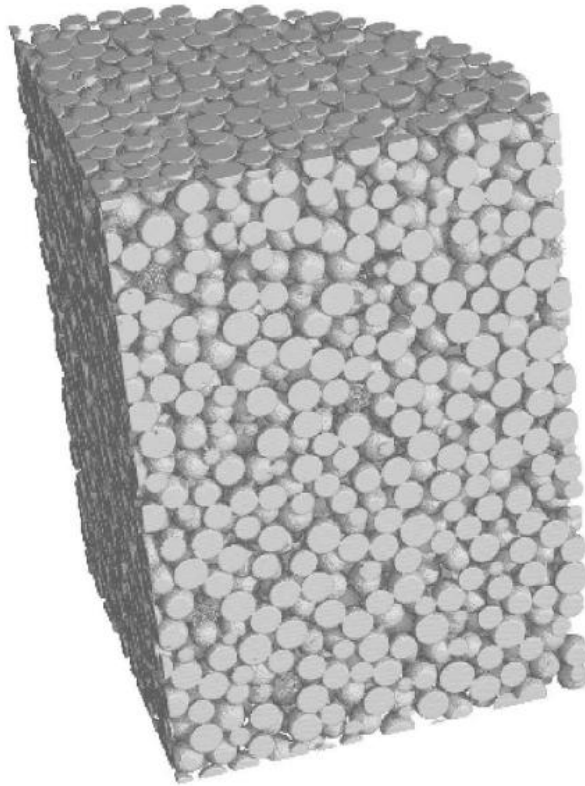


Figure 1.15: Part of a 3-D reconstruction of a static granular packing realized by the X-ray micro-tomography method (This picture is adapted from Patrick's paper[21, 72, 84]).

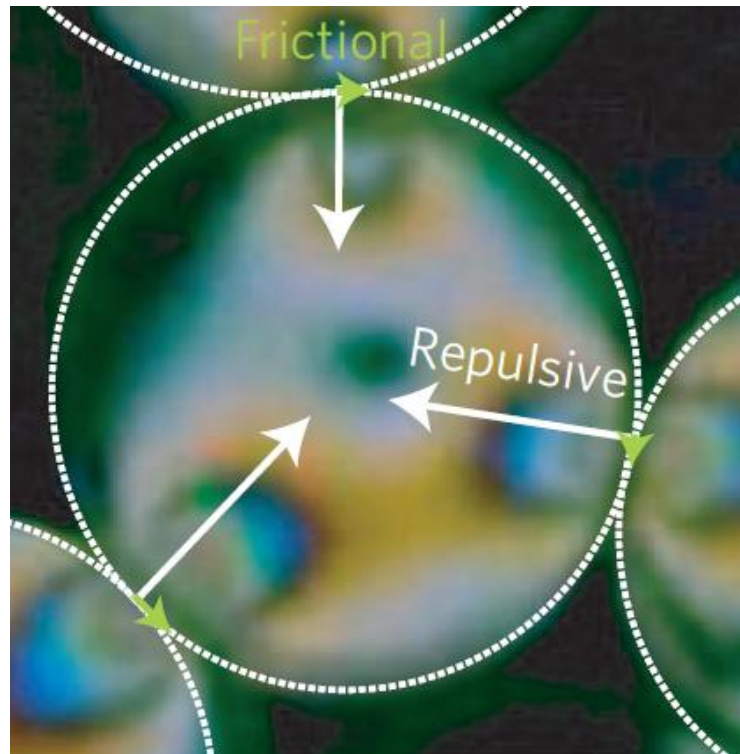


Figure 1.16: Birefringent pattern of a photo-elastic disk was used to infer the internal stress state of every individual disks, which was then assembled to find the contact force network of the whole packing (This photo is adapted from Martin van Hecke's paper[6, 89]).

1. Pulse mode - A single pulse of longitudinal vibration propagates through the system, measuring the rate of attenuation as well as the speed as a function of confining pressures and driving amplitudes.
2. Resonance mode - Based on the speed measured in the first part, the base resonant frequency is estimated and a set of frequency response curves is determined. The response frequency peak moves towards lower value as the driving amplitude increases, which is known as the “resonant frequency shift”.

1.3.1 Introduction to LAMMPS

LAMMPS[75] is the acronym for Large-scale Atomic/Molecular Massively Parallel Simulator. It is a general purpose Molecular Dynamics (MD) simulation package designed and maintained by Sandia National Lab. It is free software under GNU General Public License (GPL). It was originally written in Fortran in the mid 1990s and was re-written in C++ (released to public in 2004). It uses Message Passing Interface (MPI) for co-ordinating memory and data across variable number of CPUs. For more information on LAMMPS, including all versions of its source codes, please visit the following website: <http://lammps.sandia.gov/>

1.3.2 Force-displacement relation and Hertz contact

All MD codes integrate Newton’s second law and update particle positions recursively. The essential differences between them are the force-displacement relations. Those relations were proposed by researchers to model specific systems and their success usually depends upon how well the simulation reproduces a corresponding experiment or how well a prediction of a future experiment it can make.

To model a granular system, it is essential to know how one particle interacts with another, that is, their force-displacement relation. In the dawn of the last century, Hertz[33, 56, 69] solved the problem of calculating the repelling force of two elastic equal spheres in contact. The result of his calculation can be summarized in the following formula:

$$F_{ij} = \frac{4}{3} \sqrt{R_{ij} E_{ij}^*} (R_i + R_j - r_{ij})^{\frac{3}{2}} \quad (1.7)$$

Where R_i , R_j are the radius of two interacting balls and R_{ij} is the reduced radius defined as

$$R_{ij} = \frac{R_i R_j}{R_i + R_j} \quad (1.8)$$

Here E_i^* , E_j^* are the modified Young's modulus and E_{ij}^* is the reduced Young's modulus defined as

$$E_{ij}^* = \frac{E_i^* E_j^*}{E_i^* + E_j^*} \quad (1.9)$$

The definition of the modified Young's modulus is given by

$$E^* = \frac{E}{1 - \nu^2} \quad (1.10)$$

E and ν are the Young's modulus and Poisson's ratio respectively.

1.3.3 The attenuation problem and the energy dissipation mechanism

Macroscopic pulse transmission experiments usually only reveal how much energy was dissipated but are incapable of pointing a finger to a specific mechanism that is responsible for the energy lost. Phenomenological models have been proposed based on empirical knowledge in specific fields. Two widely cited models for energy dissipation in nonlinear elastic materials are the Preisach-Mayergoyz hysteretic elastic unit model (PM model[30, 31, 71, 59]) and the array of energy sinks model[13]. Marder[62] (unpublished) devised a method to differentiate them. He proposed that if a sine wave was to transmit through a medium described by the hysteresis model, the sine wave will soon transform to a triangular wave, while if the same wave is put through a medium described by the array of energy sinks model no change of wave shape should be expected.

Since LAMMPS had proved to generate sensible result in modeling granular systems, it is natural to wonder if it would favor one of the model against another. Also, by looking into the microscopic details of the dynamics, more physical quantities could be revealed and

probably led to more physical models.

1.3.4 The resonant frequency shift problem and earthquake triggering

Another problem that drove me to this field was the earthquake triggering mechanism proposed by Jia and Johnson[45] etc. They argued that based on laboratory results and field data, dynamic strain on the order of 10^{-6} could trigger an earthquake. The reason they put forward was the well known but not well understood phenomenon called resonant frequency shift, or dynamic strain softening. What they assumed was that there exists a fault in a critical (near failure) state. If a fairly weak wave of oscillation hits the fault causing temporary softening of the fault gouge, the softened fault gouge would no longer be able to bear the load and would eventually generate an earthquake.

Since resonant frequency shift was at the heart of their argument, it was reasonable to believe that a clear picture of the microscopic detail of particle motions at resonance and a better understanding of underlining mechanism for the frequency shift could help to build a better model that makes more precise earthquake predictions.

Chapter 2

Fracture

2.1 Discrete nature of fracture process

As mentioned briefly in the introduction, fracture at the smallest scale is a discrete process, which consists successively snapping of inter-atomic bonds. Obviously, linear elastic fracture mechanics (LEFM) and all other fracture theories that are based on the continuum assumption are inadequate for capturing features that are rooted in the discrete nature of fracture process, such as the velocity gap. To follow the dynamics of each and every atom in a dynamic process seems forbiddingly hard, yet Slepian and other pioneer researchers utilized a simple mass-spring model, cleverly manipulated the dynamic equations and provided meaningful solutions as well as intriguing predictions that inspired many young scientists to join this field[80, 60]. Fortunately, with the incredible increasing power of modern computers, scientists are now able to study the fracture process by looking into the very details of those discrete processes without making over-simplified assumptions and make quantitative predictions that can be directly verified by experiments. In this chapter, I will try to present a brief survey of the study of dynamic fracture process from three different points of view:

1. the mass-spring model (theoretical) approach[80, 60]
2. the numerical approach (mainly Molecular Dynamic simulations)[19, 60, 34, 39]
3. review of some previous experiments[42, 36]

2.1.1 Theoretical study of fracture process

I have no intention of presenting a comprehensive review of the theoretical study of fracture process. Instead, I will concentrate on a one-dimensional lattice model that absorbed many of the previous results and had some of its own. The model was proposed by Marder and Gross[60] in 1994 and was built upon the work of Slepian[80] and others.

The lower portion of figure 2.1 is one solution of the model, and the dynamics of the crack tip are magnified to indicate the setup of the equations. The equation concerning the dynamics of the atom $(m, +)$ was given by the following equation:

$$\ddot{u}_{m,+} = \begin{cases} u_{m+1,+} & -2u_{m,+} + u_{m-1,+} \\ + & \frac{1}{N}(U_N - u_{m,+}) \\ +(u_{m,-} - u_{m,+}) & \theta(2u_f - |u_{m,-} - u_{m,+}|) \\ -b\dot{u}_{m,+} \end{cases} \quad (2.1)$$

The trick is to find only the steady state solution and apply the following symmetries

$$u_{m,+} = -u_{m,-} \quad (2.2)$$

$$u_{m,+}(t) = u_{0,+}(t - m/v) \quad (2.3)$$

Applying the Wiener-Hopf methods, an analytical solution of the equations above can be found.

The end product of the lattice model was a prediction of the crack speed as a function of the driving force Δ .¹

Figure 2.2 illustrates the prediction of the one-dimensional lattice model for a situation of $N = 100$ and $v = 0.5$.² Notice that the horizontal line at velocity zero extends far beyond $\Delta = 1$, meaning that excessive energy can be stored in the lattice model without

¹The driving force Δ was defined as a ratio of the displacement of the outer boundary U_N and the minimum value of U_N (indicated as U_N^c) at which enough energy was stored to the right of the crack so as to break the bonds, $\Delta \equiv \frac{U_N}{U_N^c}$.

² N is the number of the atoms above the crack line, and v is the steady state crack speed.

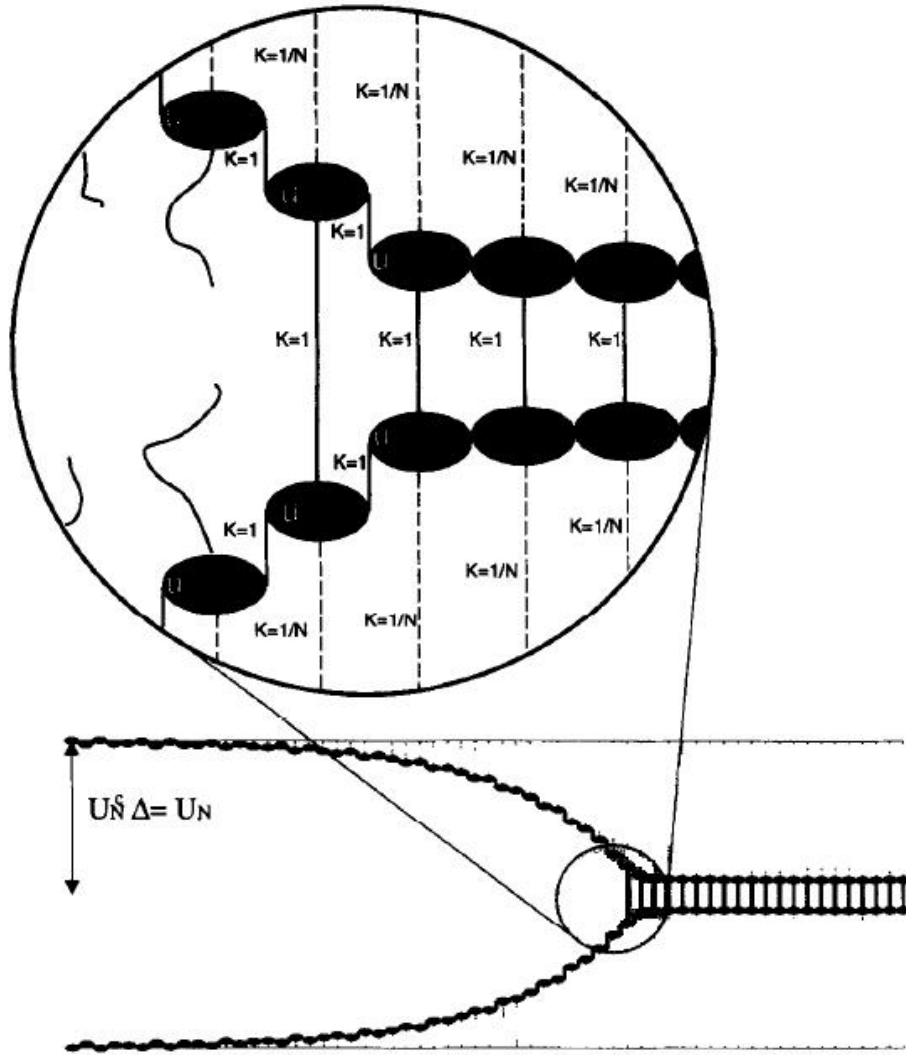


Figure 2.1: One-dimensional lattice model used to simulate a dynamic fracture process. (This graph is adapted from Marder and Gross's paper[60].)

triggering a crack propagating forward. This is known as lattice trapping, first proposed by Thomson *et al.* in 1971. Another interesting feature of the graph is the zig-zag pattern between $v = 0$ to $v = 0.4$. It turned out that those solutions were unstable and hence forbidden in steady state crack propagation (this forbidden speed range is then call “the velocity gap”). Motivated by this finding, Marder *et al* were interested to see if the velocity gap was an artifact due to the over-simplified model or it was a generic feature that exists in more realistic settings. So, they devised a molecular dynamics simulation with much more sophisticated inter-atomic potentials to simulate a propagating crack. Meanwhile, they started to conduct fracture experiment using real silicon wafers.

2.1.2 Numerical study of fracture process

There is no doubt that the laws of physics in the microscopic scale is quantum mechanics and the governing equation for the dynamics of electrons and nucleus is the Schrödinger’s equation. But this equation is analytically solvable only for the hydrogen atom. Various approximation methods are developed to calculate properties of more complex atoms and molecules. One popular example is the density functional theory (DFT) with the local density approximation (LDA), which is believed to be the most reliable techniques available for numerical treatment of materials. However, even that is restricted to perfect crystals and unit cell sizes around 1000 atoms[51]. For problems involving larger numbers of atoms (problems requiring a minimum of about 10^6 atoms to capture just some of the underlying physics, such as fracture or dislocation loops), approximation methods with much greater computational efficiency are certainly needed.

Molecular dynamics (MD) simulation with empirical inter-atomic potentials provides an alternative approach to these problems. Calculations within molecular dynamics are completely classical, with all the information of the interactions between neighboring (not necessarily nearest) atoms contained in the effective inter atomic potentials. Different functional forms of the potentials with different numbers of fitting parameters and fitting strategies give a variety of predictions concerning certain properties of materials. The validity and transferability of these potentials are then checked by comparison to experiments. The advantage of molecular dynamics simulation is its speed and the ability to handle a large number of particles. For the standard of about half a decade ago, $\sim 10^7$ atoms followed

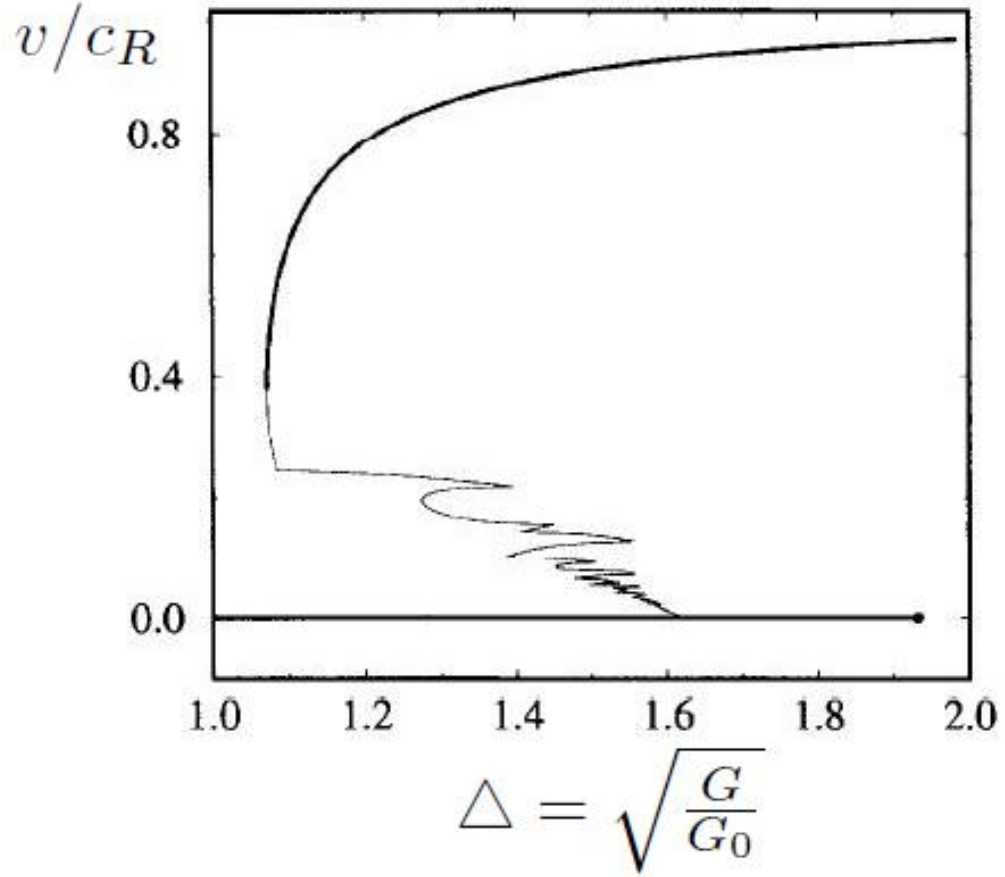


Figure 2.2: Solution of the 1-d lattice model gave the first indication of the existence of a velocity gap. A crack would not propagate even the energy stored in the system was more than the minimum energy required to sustain a running crack based on the Griffith's energy balance criterion, which was known as lattice trapping. For a fast running crack (Started at the up right corner of the graph.), if the energy available to the crack tip gradually decreased towards the Griffith's threshold, a stable solution did not exist for v smaller than 0.4, hence the crack would abruptly come to a stop. This range of velocity where no stable solution existed was then called a velocity gap. (This graph is adapted from Marder and Gross's paper[60].)

for a few tens of nanoseconds was achievable by molecular dynamics with fairly sophisticated inter atomic potential. Today, simulations of billions of atoms for nanoseconds are possible. Rapid brittle fracture of silicon is one typical example of the problems that requires a large number of particles. Experimentally, it involves a macroscopically stressed piece of silicon containing a number of atoms on the order of 10^{22} , within which an atomically sharp crack tip propagates. Although dynamics of the crack tip is determined microscopically by the successive failure of the covalent bonds between atoms, the energy needed to break these bonds is supplied macroscopically. Numerically, many attempts have been performed to simulate brittle fracture of silicon with different inter atomic potentials, but no consensus conclusion are reached yet, partly because none of the existing potentials is particularly superior in predicting the material properties of silicon and many even failed rather badly in reproducing the basic cohesive energy curve. There have been more than 30 empirical inter atomic potentials invented for the description of different aspects of properties of silicon since 1980s. Among them, the Stillinger-Weber potential (SW)[82], the modified embed atom method (MEAM)[12] and the environment-dependent inter-atomic potential (EDIP)[5] are the most frequently used for the description of rapid brittle fracture of silicon.

Though the SW potential[82] has been very successful in predicting many material properties of silicon, such as the elastic constants and thermal coefficients, it failed to predict brittle fracture along the experimentally preferred cleavage planes (111) and (110)[35]. At low or moderate strains a crack will not propagate at all. At high strains, the crack tip region becomes very disordered. The SW potential does give a type of fracture along the (100) plane[2], which is quite rough on the atomic scale. However it is known experimentally that fracture surfaces along the (111) plane can be atomically flat[55].

A simple estimation of the fracture energies along different crystal planes by Griffith's critical energy analysis shows that the minimum energy density required for a crack to propagate along the (111) plane is around $2.78 \frac{J}{m^2}$ and along the (110) plane is around $3.28 \frac{J}{m^2}$, but the required energy density for a crack to propagate along the (100) plane is significantly higher, around $4.54 \frac{J}{m^2}$ based on Hauch's experiments[32]. So, a crack in silicon is energetically favored to propagate along the (111) plane and (110) plane rather than (100) plane, which is in agreement with experimental observations. Whether a crack can propagate along the (100) plane in a brittle manner is still experimentally inconclusive

and numerically questionable. But the failure of prediction of brittle fracture along (111) plane and (110) plane clearly indicates the shortcoming of the SW potential in predicting the mechanical properties of silicon, especially when the system is far from equilibrium. In order to get a brittle fracture of silicon, Marder etc. inadvertently proposed a modified SW potential, in which the coefficient of the three body term had been multiplied by a factor of 2. This modification did predict a brittle fracture along the (111) and (110) planes, but it worsens the likeness to real silicon in other respects such as the melting temperature been raised to approximately 3500K while the experimental value is around 1683K and elastic constants also been shifted some significant amounts[34]. Thus, they concluded that neither the Stillinger-Weber potential nor their modification can be regarded as a satisfactory account for simulation of brittle fracture of silicon.

The embedded atom method (EAM) was invented in early 1980s by M. S. Daw and M. I. Baskes[12] as a semi-empirical model originally designed for metals. The EAM is based on local electron density theory, which has been shown to accurately describe a large number of properties in metals. In the later 1980s, M. I. Baskes modified the original EAM to describe the covalent bonding for materials such as silicon, and called the result the modified embedded atom method (MEAM)[4].

The basic idea behind the EAM is that each atom in a solid can be viewed as an impurity embedded in a host comprising all the other atoms. Because the energy of an impurity is a function of the electron density of the unperturbed host, the cohesive energy of a solid can be calculated from the embedding energy.

The MEAM was applied to molecular dynamic simulations of brittle silicon fracture by J. G. Swadener etc. recently[39]. The simulations produce propagating crack speeds that are arguably in agreement with experimental results. The results of the simulation and comparisons with experimental results are summarized in figure 2.3.

The experimental results are indicated as open squares; The simulation results are open cycles (model height=239Å), full cycles (147Å) and full triangles (112Å); The solid line is continuum prediction.

Actually, Holland and Marder had done a very similar study of brittle fracture simulation of silicon by MEAM a year earlier[35]. Their results, as summarized in figure 2.4, are quite different however. The predicted minimum energy density for a crack to propagate

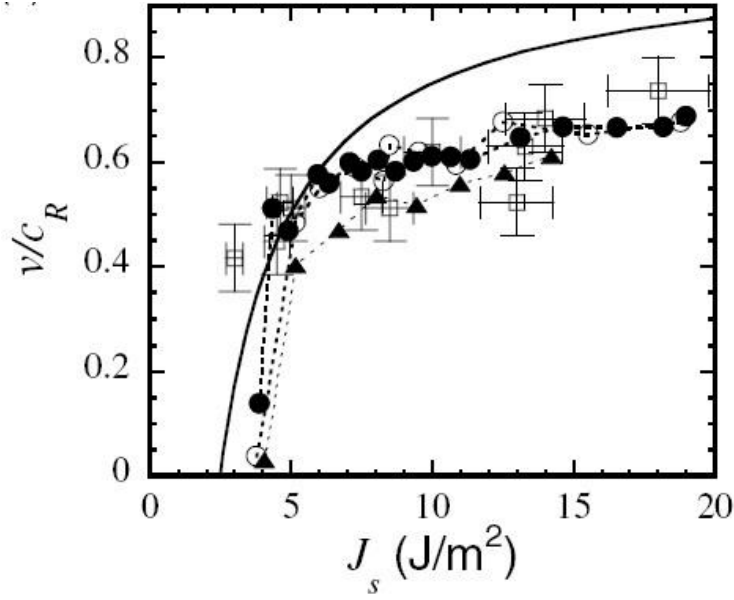


Figure 2.3: Silicon fracture simulated with MEAM, which was then compared with experimental results. (This graph is adapted from Swadener’s paper[39].)

is greater than $5 \frac{J}{m^2}$, while the corresponding experimental value is around $2.5 \frac{J}{m^2}$.

The difference between Swadener’s results and those of Marder’s is not due to the potential, since they were using exactly the same potential. So, Swadener[39] etc. claimed that all previous simulations failed to agree with experiments due to the ignorance of the corresponding variation of the effective Young’s modulus and Rayleigh wave speed as the strain within the silicon strip changed. If all of these changes were evaluated properly with MD simulations adopting the MEAM potential, the simulation would be in agreement with experiments. But, Marder strongly doubted this conclusion. Marder pointed out that some of the formulas used in Swadener etc.’s paper are actually borrowed from continuum theory and not applicable to the special geometry of the relevant problem. The energy stored in the system could be evaluated directly from the simulation rather than applying some approximate formulas as done by Swadener et al. The most serious defect of Swadener et al.’s simulation might be that their system was too small in size and the crack tip had not reached a steady state as the evaluations of the crack speed and fracture energy were performed. On the contrary, Marder[60, 63] et al.’s simulation scheme didn’t have such a problem since they applied a method that continuously cut a portion of the system that had

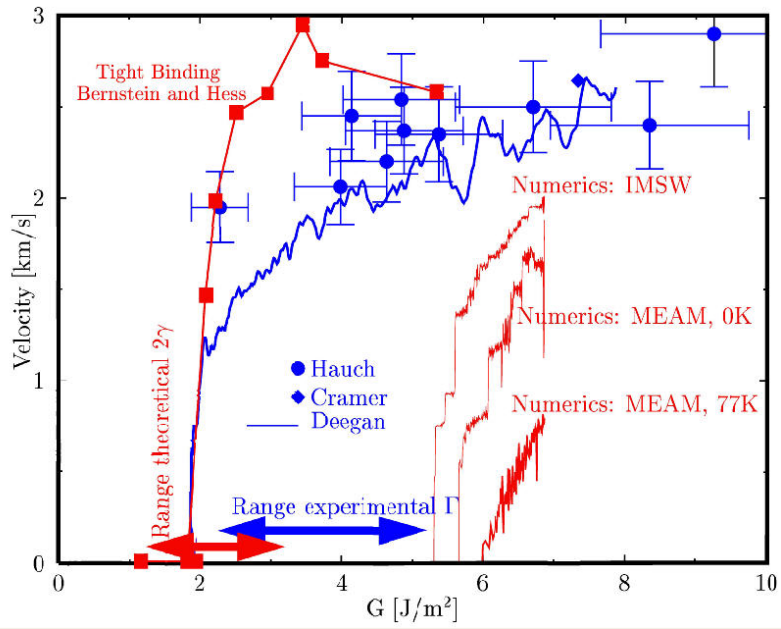


Figure 2.4: Comparison of numerical simulation results[35, 7] and experimental results[42] for silicon fracture. All classical Molecular Dynamics simulations disagree quantitatively with experiment (MEAM, IMSW). The tight binding results of Bernstein and Hess appear to be compatible with experiment.

fully relaxed after the crack propagated through and pasted a portion of stressed material in front of the crack tip. By using this method, they could follow the dynamics of the crack tip for a much longer period of time and found a truly steady state of the crack.

The environment-dependent inter-atomic potential (EDIP) was developed in later 1990s by Martin Z. Bazant[5] etc. The EDIP is similar in form to SW potential but has an environmental dependence. The interaction model includes two-body and three-body terms which depend on the local atomic environment through an effective coordination number. There are 13 adjustable fitting parameters for this potential, half of which can be theoretically estimated. The theoretical base underlying the model include an analysis of elastic properties of the diamond and graphitic structures and inversion of ab initio cohesive energy curves.

The reason that M. Z. Bazant etc. developed a new potential even when there were already dozens of inter-atomic potentials for silicon in the literature was that they were unsatisfied with the transferability of all the existing potentials. Most of the potentials give reasonably good predictions only for limited aspects of silicon properties and it is often unclear whether the good agreement of simulation and experiment is due to the functional form of the potential, or the sophisticated fitting strategy.

EDIP had been used to simulate fracture in silicon by Bernstein and his coworkers recently, but their simulation failed to agree with experiments[7]. The fracture energy they predicted is almost 10 times the energy observed in experiments. Also, the crack tip in their simulation proceeds in a very ductile manner accompanied by significant plastic deformation and disorder, while brittle crack are seen experimentally. A snapshot of their simulation is given in figure 2.5. It is worth mentioning that Holland and Marder had achieved similar results two years before Bernstein etc. during their search for the best potential to describe the brittle fracture of silicon[35].

The failure of all these empirical potentials mentioned above could be due to their short-range cut-off, which produces unrealistically large cohesive force and prevents bonds from breaking[35]. Restricted by the value of the surface energy, the depths of different potentials are pretty much the same no matter how different their shapes or ranges might be. Most of the empirical potentials of silicon such as SW and EDIP include only nearest neighbor interactions, while density functional theory predicts an interaction range considerably

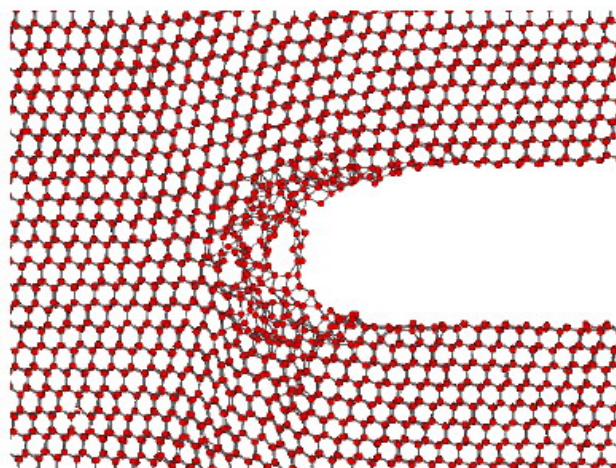


Figure 2.5: Snapshot of MD simulation with EDIP (Adapted from Bernstein’s paper)

longer. A comparison of the ranges of different potentials is illustrated in figure 2.6.

It is obvious that a shorter cut-off will force a potential to rise more steeply, which corresponds to a short-range but stronger attractive force. Therefore, even when it is energetically favorable for the crack to propagate, the stress at the crack tip may not be high enough to break the bond. This is one of the reasons why these empirical potentials failed to simulate the brittle fracture of silicon.

The UER curve on the graph is the universal energy relation curve, which comes from an empirical fit to the cohesive energy curve from density function theory[41].

Though the guess of a proper functional form for the potential is essential for the success of the simulation, it is not the only problem worth concern. The size of the simulation is in no way directly comparable to experiments even for the most powerful computer built to date. In fact, a simulation involving ten billion atoms describes only a cube of matter no more than half a micron along each side. And even for computers powerful enough to handle a system with so many degrees of freedom, they will not be able to follow the behavior of all the particles for much longer than a nanosecond. So, comparison of the simulations with experiments requires a careful scaling analysis. There are two alternative solutions for this problem. One is to couple molecular dynamics with a continuum simulation dynamically[7]. The other one is through a clever scaling argument that reduces the system size significantly and traces the crack tip for much longer time. A cut and paste procedure

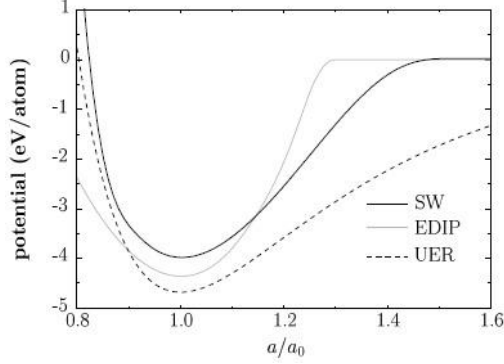


Figure 2.6: Comparison of the range of SW potential and EDIP (Adapted from Bernstein’s paper)

was carefully manipulated to host the crack tip within the central region of the system[34].

There is yet another problem worth mentioning. It is how to determine whether the system has reached the steady state or not. For a system of millions of atoms and driven far from equilibrium, it is a nontrivial task to set a correct criteria for a steady state. If a system is too small in size or the evolution of the system is not traced long enough, it is quite possible that the system is not in a steady state but rather in a transient state.

Despite all the difficulties, numerical simulations of dynamic cracks become increasingly realistic and provide a complementary means to study fracture process on the atomic scale.

2.1.3 Previous experimental study of fracture process at CNLD (Center for NonLinear Dynamics)

It hardly takes any effort to break a silicon wafer in a casual way. As a matter of fact, caution has to be taken to prevent that from happening. Dropping it to the ground it shatters into pieces since it is regarded as one of the perfect brittle materials at room temperature. But, it is rather difficult to break a silicon wafer in a controlled fashion mostly due to the fact that precisely controlled boundary condition is hard to achieve and is even harder to maintain as the crack propagates.

Jay Fineberg and Steven Gross[29] designed a tensile testing machine as schematically illustrated in figure 2.7 and named it “Whomper”. It had a stiff outer skirt made of

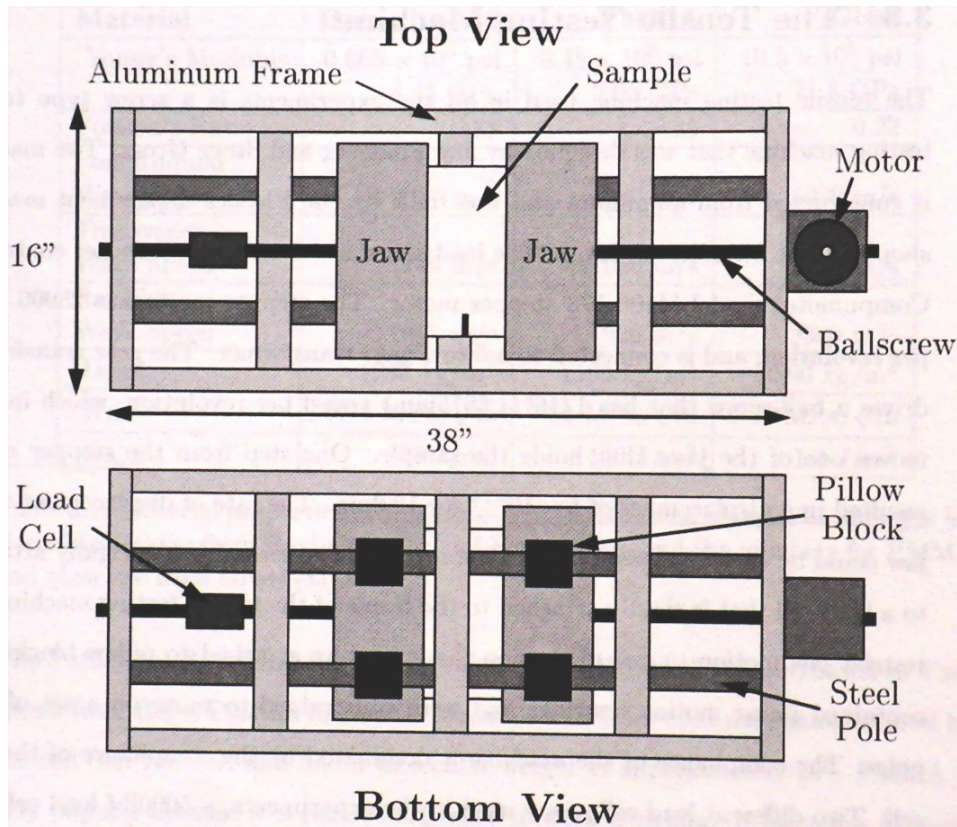


Figure 2.7: Gross's tensile testing machine, "Whomper" (This graph is adapted from Hauch's PhD thesis[32].)

bulk Aluminum. The integrity of the frame was further enforced by three Aluminum bars. A pair of jaws each sitting on top of two pillow blocks were free to move along the long axis but fixed on the other direction to ensure uni-axial loading. To conduct a fracture experiment, a piece of sample was fixed to the jaws with a small crack initiated on one side. A computer controlled stepper motor provided the driving force to tear the sample apart. The crack speed and energy release rate were measured independently during the fracture process and compared to theoretical predictions as well as computer simulations.

Jens A Hauch performed a series of fracture experiments on Whomper in later 1990s. The materials he used included Holimmate-100, PMMA, glass and silicon[32]. For the purpose of searching for the velocity gap, I will only describe the dynamic fracture experiments done in single crystal silicon.

In order to make a direct comparison of the experimental results with the prediction of MD simulation possible, it was necessary to have a fixed boundary as the crack propagates. So, Hauch[42] altered the original design by having the silicon sample sandwiched between two identical frames of steel whose center were milled off as shown in figure 2.8. The two side beams on each steel frame will act as very stiff extension elements when the whole structure was subjected to uni-axial loading along y axis. Only a small fraction of the total load ($< 2\%$) was transmitted through the silicon sample, so to a good approximation the boundary can be regarded as fixed when the crack happens.

The results of Hauch's experiment and comparisons to MD simulations are shown in the figure 2.9. There is an obvious discrepancy between experiment and simulation, especially at the lower limit of energy release rate at which steady fracture could take place. The MD simulation predicted almost twice as much energy release rate as the lowest limit seen experimentally. As stated earlier, this discrepancy led Bernstein and Hess etc. to propose that quantum mechanical calculation is inevitable for a precise account of the fracture dynamics of single crystal silicon.

Unfortunately, Hauch's experiment, which was done at room temperature, wasn't decisive in determining the existence of the velocity gap. Shortly after the propose of the velocity gap, Marder and Holland realized that thermal fluctuations at room temperature are energetic enough to kick off an arrested crack to propagate again. That is, thermal agitation destroyed the visibility of velocity gap and the crack can run at any speed. So, they modified their MD simulation of silicon fracture to include thermal energy effect. Figure 2.10 gives a snapshot of their simulation.

The result of their simulation indicated that it is necessary to conduct the fracture experiment under 100 K in order to see the velocity gap without the disturbance of thermal fluctuation. Figure 1.5 summarized their finding on how thermal energy destroyed the existence of the velocity gap. The basic idea was that for a crack otherwise would have stopped, a random thermal fluctuation snapped the bond right ahead of the crack tip and re-initiated the propagation. Depending on how much thermal energy was available, this process could happen frequently enough as if there was no velocity gap, that was, the crack could run at any speed within the velocity gap. Until temperature was reduced under 100 Kelvin, a random thermal agitation became rear enough such that the velocity gap began

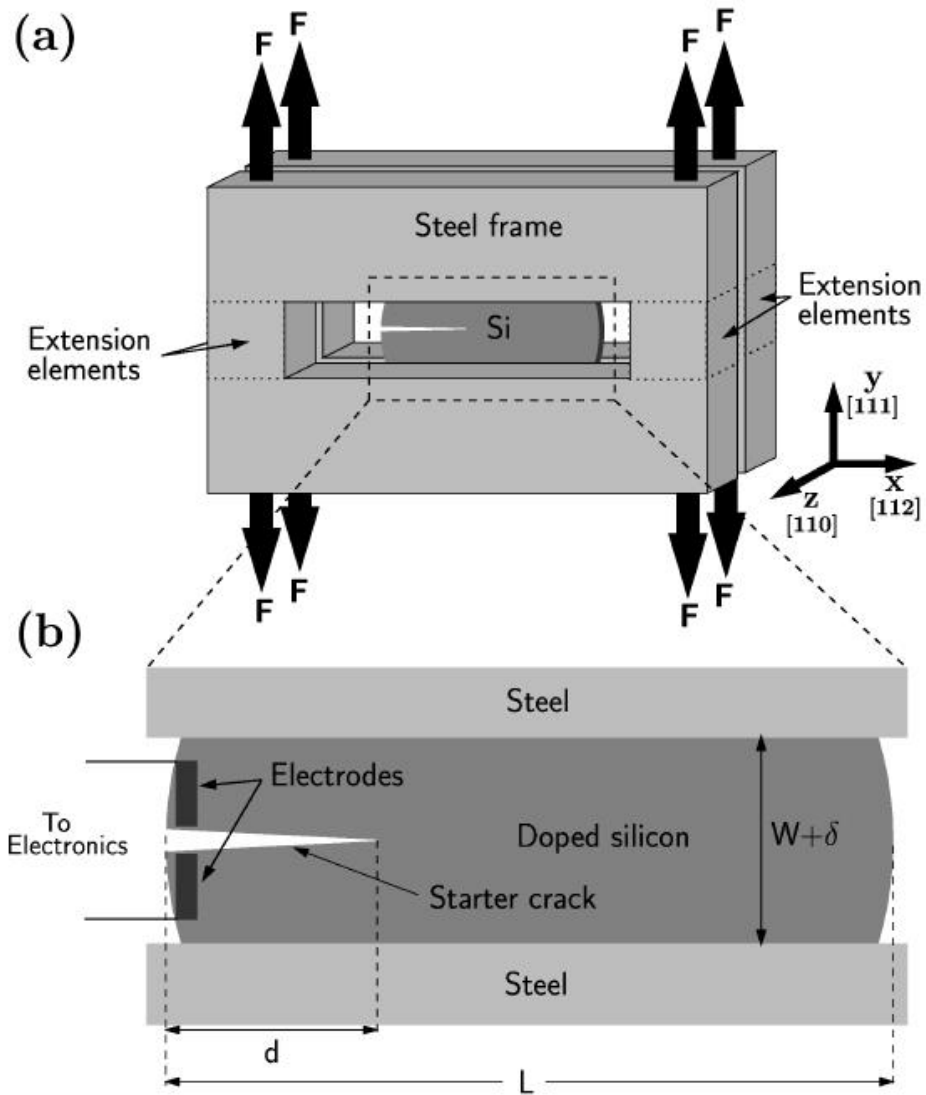


Figure 2.8: Hauch's sandwich design (This graph is adapted from Hauch's paper.)

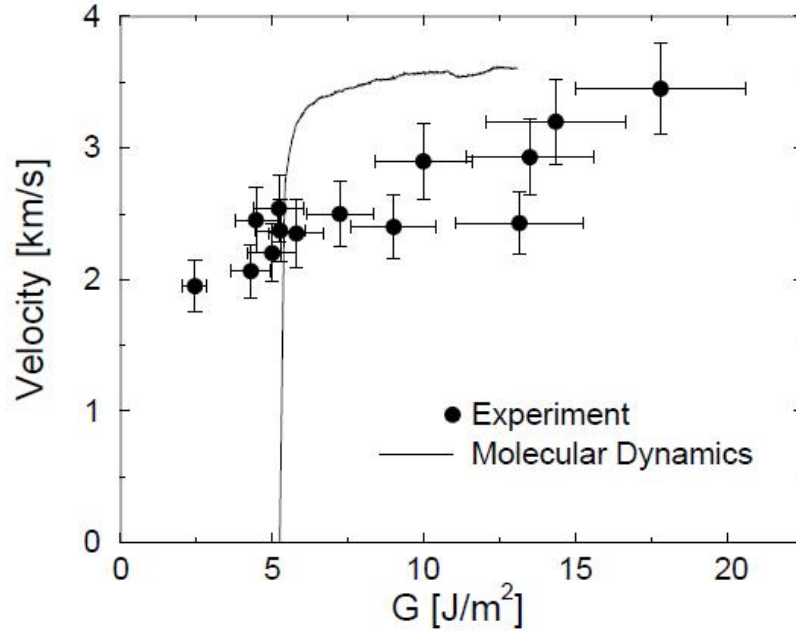


Figure 2.9: Comparison of experimental results to MD simulation results (This graph is adapted from Hauch's paper[42].)

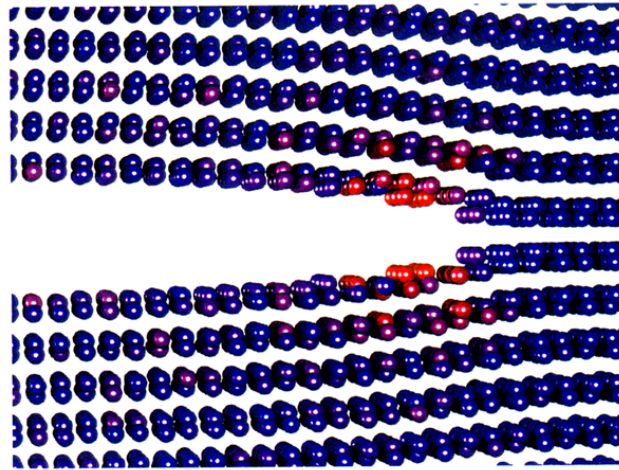


Figure 2.10: MD simulation of silicon crack including thermal energy (This picture is adapted from Holland's paper[35].)

to be detectable, which was the reason that I had to conduct the silicon fracture experiment in liquid nitrogen environment in order to find the velocity gap.

2.2 Experimental study of crystal silicon fracture at liquid Nitrogen Temperature

2.2.1 Motivation

The primary objective of the low temperature silicon fracture experiment is to search for the velocity gap.

2.2.2 Experimental setup

As mentioned earlier, Hauch had done some room temperature fracture experiments on silicon. But, the apparatus he used is incompatible with the requirement of low temperature fracture experiment. The main issue is the great difference of thermal contraction between silicon and steel. It is estimated that if silicon is glued onto the steel frame and then cooled down with it, a few tens of degree Kelvin is enough to break the silicon by thermal contraction alone. Besides, the glue Hauch used would lose its adhesive power before the desired temperature was reached and the Whomper is simply too big to cool down entirely.

To overcome these difficulties, new experimental designs were prepared by Robert Deegan. The basic idea was to cool down first and stretch later. That is, silicon wafer would be put in position and cooled down with the steel frame loosely, some mechanism would then fix it upon the steel frame after the desired low temperature (less than 100 Kelvin) had been reached and stabilized. Most glues don't work in that temperature range, and even if they do, it is nearly impossible to apply them in situ. So, friction was chosen as the mechanism to hold up the silicon wafer to the steel frame in low temperature.

Using friction as the mechanism for holding the wafer to the steel frame was believed to work because we have a method to control the normal force exerted on a pair of steel blocks through silicon wafer onto the steel frame. We can first put the silicon wafer in its position and cool it down. While cooling, nothing but a small residual normal force due to the weight of the pressure blocks is on the silicon wafer. When the desired temperature is

reached and it is time to break the sample, a much larger normal force is applied to the top of the pressure block by inflating a set of four brass bellows, which push the pressure blocks against a pair of C-shape steel clamp fixed to the frame. See figure 2.11 for a graphic illustration of the friction holding mechanism.³

2.2.3 Potential drop technique

It is not a trivial task to measure the speed of a propagating crack in silicon since it is on the order of kilometers per second while the size of the silicon wafer is only a few inches. That is, it all happens within one micro-second if it happened at all. A very fast electrical method must be applied to trigger at exactly the right moment and a fast and large enough data acquisition device is needed to quickly capture, store and transfer data.

The principle of the potential drop technique is fairly simple: as the crack starts to propagate, the resistance of the silicon wafer will change. Using the same principle as the four point probe, a semi-constant current is fed through the outer two tabs of the wafer and the voltage of the inner two tabs is measured. The advantage of this technique is that it is insensitive to the contact resistance of the tabs to the wafer. By monitoring and recording the potential drop across the inner two tabs at a high enough frequency, it is possible to retrieve the information of the position of the crack tip as a function of time and hence the crack velocity.

One necessary step of this technique is to invert voltage readings back to crack tip position on the wafer. It is done by solving a two dimensional PDE with some specific boundary conditions by the finite element method in Matlab.

Figure 2.12 represents a typical snapshot of the solution to the PDE. The geometry exactly mirrors from the physical dimensions of the silicon strip under test. Currents are not allow to flow through any of the outer boundaries. (The crack interface can be viewed as part of the outer boundaries as well since it is implemented by cutting a very thin layer of material off the main body of the strip.) A constant current flows from the up-most tab through the body of the silicon strip and sinks at the bottom-most tab. Potential difference is then measured between the inner two tabs and plotted as a function of crack length in

³Note that for purpose of clarification, only half of the system is shown, which includes one piece of C-shape clamp one pressure block and two brass bellows. Complete system configuration is shown on the side view.

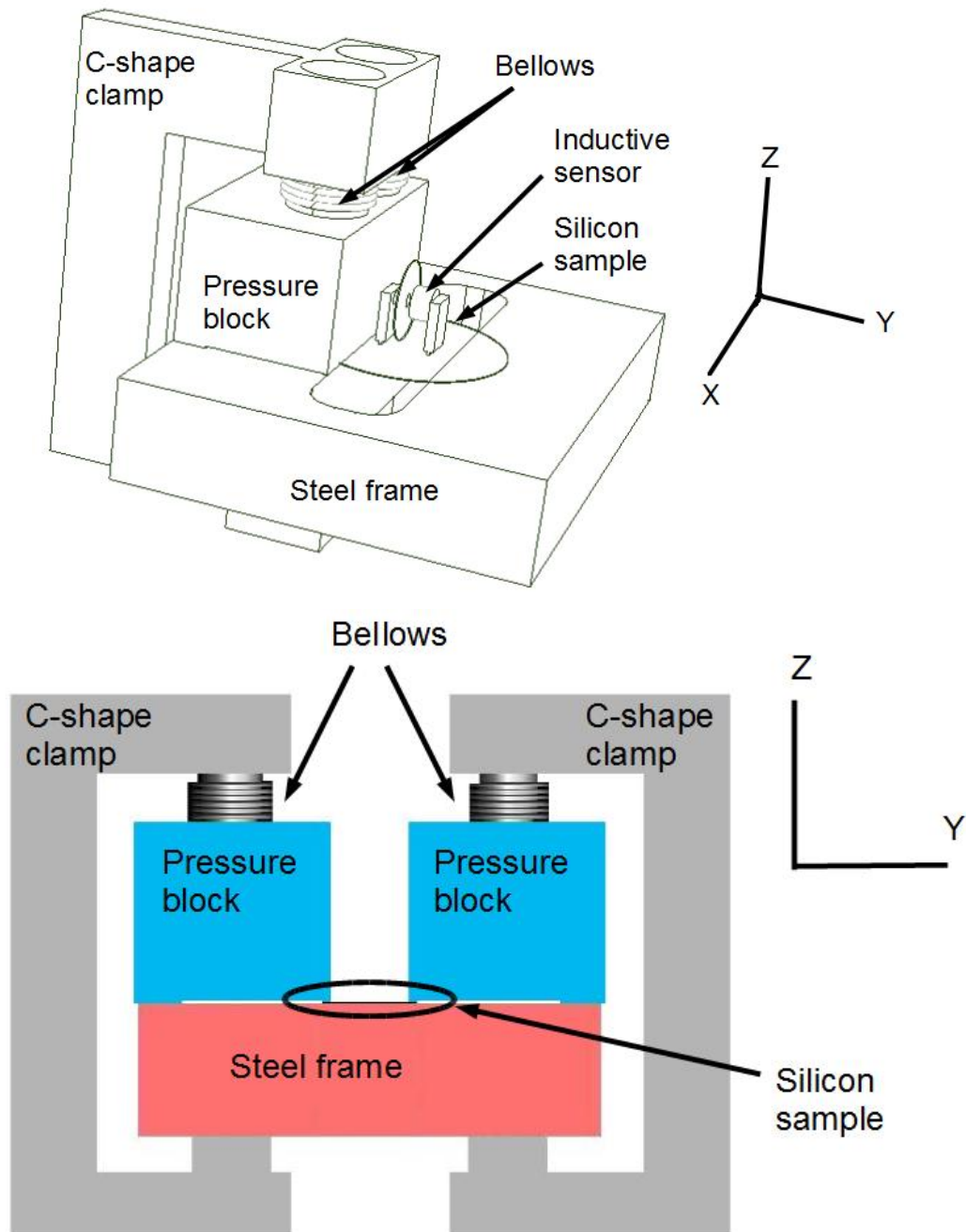


Figure 2.11: 3-D block diagram and 2-D side view of the friction holding system. A silicon sample sits on top of a steel frame whose middle portion is milled out. Two pressure blocks each have two feet; one sits on top of the steel frame and the other on top of the silicon sample right along the edge of the middle window of the frame. Two C-shape clamps each having a pair of bellows complete the force loop. This works much the same way as we use our hand to grab a burger; the C-shape clamp acts as a hand and the steel frame, silicon sample and the pressure block are the contents of the special burger.

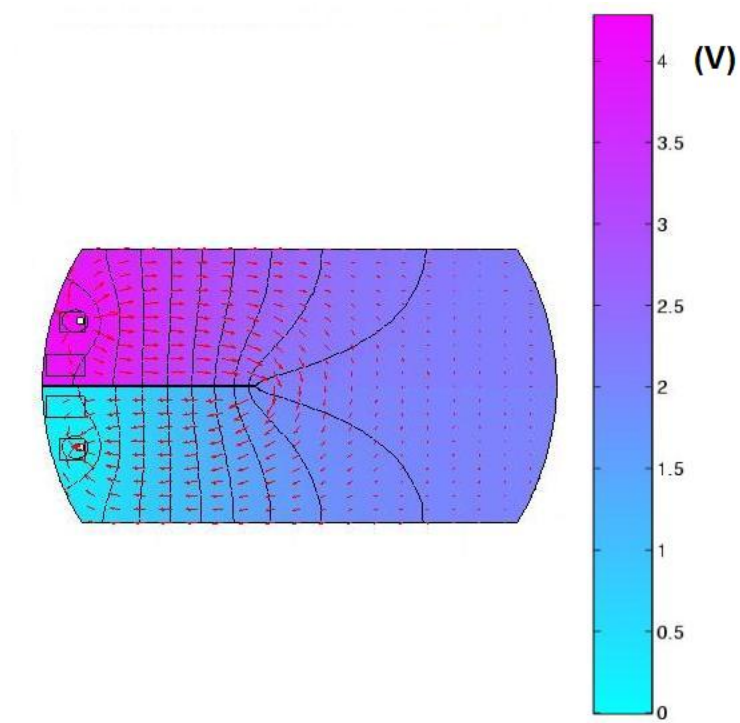


Figure 2.12: Potential map and current flow through a partially cracked silicon wafer (Numerical solution of a boundary condition partial differential equation given by Matlab.)

figure 2.13.

2.2.4 The data acquisition circuit

The electronic data acquisition circuit is shown in figure 2.14. A semi-constant current source connected to the outer two tabs of the wafer and the voltage change across the inner two tabs was monitored by the data acquisition circuit. As the crack starts to propagate, the voltage on the inner two tabs begin to rise. Once it goes over certain tunable threshold, the triggering mechanism flips and a time frame of data is captured and transferred to a PC interface card and recorded to the computer's hard disk. The voltage of the inner two tabs is buffered and directly fed to the computer through channel 1, while an in-line differentiator performs an analog differentiation before the data is fed to the computer on channel 2.

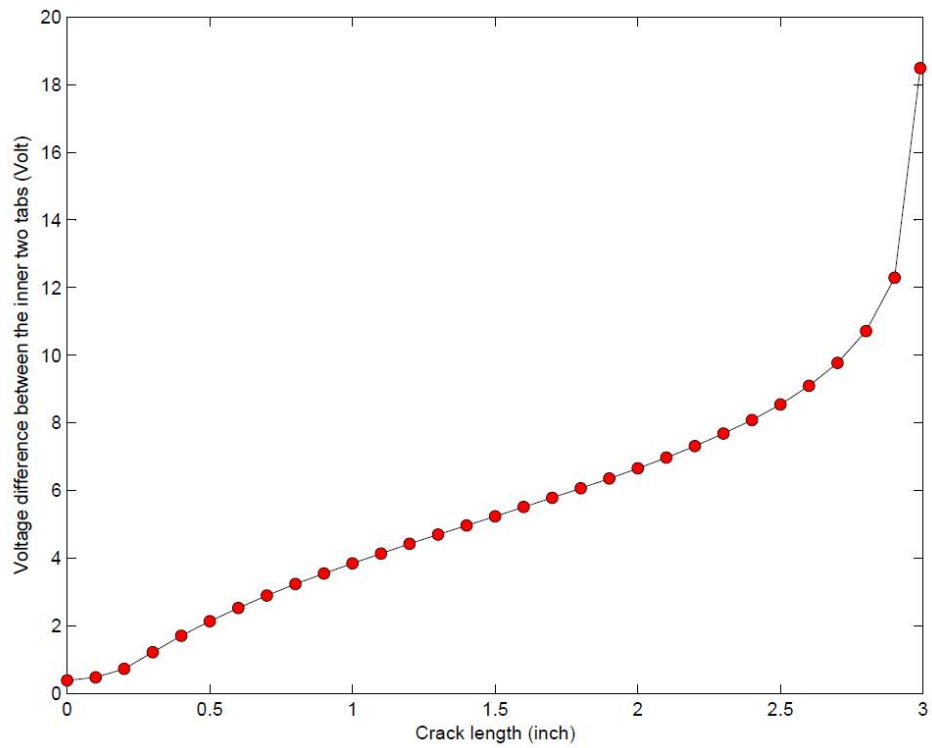


Figure 2.13: The relationship between the potential difference of the inner two tabs and crack length under constant current assumption. Each dot represents a solution for a particular crack length and the line is just an interpolation to show the general trend of the data.

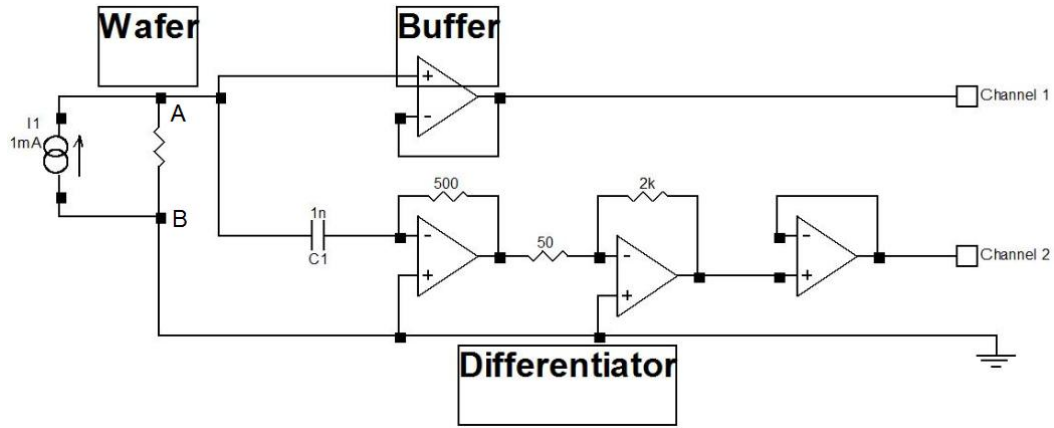


Figure 2.14: Data acquisition circuit for the fracture experiment. The resistance of the wafer is represented by the resistor between A and B. With a constant current source on the order of 1 mA, the potential difference between A and B is measured. Channel 1 picks up the voltage reading directly while channel 2 takes the same voltage data but makes an analog differentiation before the data is recorded.

2.2.5 Some major difficulties of this experiment

2.2.5.1 Wafer not breaking straight

There were two major problems that prevented me from getting the experiment done as it was designed and I spent over half of my PhD life to track them down. The first problem was that the wafer did not break straight. This may sound unlikely for the wafers were pre-cracked in the most preferred fracture plane and subject to a uni-axial loading. Why would it want to go any other directions other than straight down the road? But, that is exactly what it did. Obviously, for that to happen, the opening of the middle window of the steel frame was not purely Mode I. Where were these other modes coming from?

To answer that, I checked three possible sources of imperfection.

First, I checked the crack initiation process. The previous practice was to heat a notched wafer in a boiling water bath and then quickly dip it into icy cold water. This method didn't work very well. Some times it failed to generate an initial crack, while more likely, it would produce an initial crack that is too long (such as half way through). Besides, this method can cause the metal tabs to lose contact with the wafer. So, I chose to use another widely used method for introducing initial crack to a wafer called three-point-

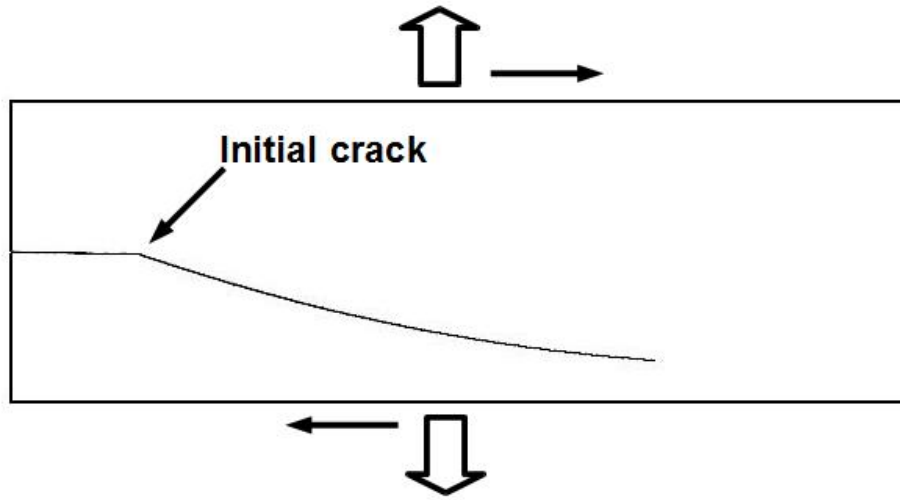


Figure 2.15: It is demonstrated through calculations within software package franc2d that if only a few percent of the elastic energy goes into Mode II, the crack will deviate from its original path, which is not desirable in our experiment.

bending. Basically, one uses a diamond pen to make a tiny scratch at some desired location on the edge, then puts a small cylindrical object (I used a straightened paper clip) directly underneath the scratch. The final step is to gently push down on both sides of the scratch. This method is much more reliable and the initial crack length was partially controllable.

Second, the wafer orientation was suspected. Previously, we used the primary flat indicated by manufactures to do our alignment. But, due to processes of polishing or something else, the flat wasn't straight like a razor blade, especially around the corner. In addition, the uncertainty of the flat was specified as $\pm 1^\circ$ by the manufacturer. One degree may sound negligibly small, but after putting a shear force due to 1 degree misalignment into a finite element fracture code called franc2d⁴, the code produced a badly deviated crack (see figure 2.15 for details).

In order to solve the wafer orientation problem, I decided to create a reference plane by myself. It turned out that all I need to do was to apply three-point-bending a few more times. Instead of just generating a small initial crack, now I broke it all the way through. The flat so created was amazingly straight and flat.

⁴Franc2d is a two dimensional, finite element based program for simulating crack propagation in planar structures developed by researchers in Cornell University. For more information, please visit http://www.cfg.cornell.edu/software/franc2d_casca.htm

Finishing the first two steps did not help too much in getting a straight break, but did help narrowing down the problem.

Finally, I started to suspect the design of the experimental loading device. By looking at Hauch's and Deegan's setup, I eventually realized that there is a stability issue concerning the deformation of the steel frame between these two devices. Hauch's setup is intrinsically stable because the forcing is external to the steel frame and self-correcting to its symmetrical axis. In order to minimize the size of the apparatus to fit it into a small container for the low temperature experimental requirement, Deegan's setup imposes forcing from inside of the steel frame (by galvanizing a pair of piezo-electric transducers or inflating a pair of bellows). That is, the self-correcting mechanism was missing, and to make things worse, he reduced the thickness of the extension element by a factor of 5 to match the much weaker forces provided by the piezo-electric transducer or bellows. That makes his design very vulnerable to shear. The frame is actually unfavorable for expansion; instead the frame will prefer to deform in the shear direction instead of the expansion direction. (Hauch's setup is illustrated in figure 2.7 and 2.8, and Deegan's setup is illustrated in figure 2.16).

I tried many different ways to control the shear deformation of the frame. I tried to rotate the bellows in the side windows hoping to find a balanced configuration such that any mis-alignment of them can be canceled in the shear direction. That didn't work because the tunable angle is very limited due to available space. Besides, for real experimental runs, we would want to create differential loading between these two bellows such that the energy release rate decreases as the crack propagates, so one configuration wouldn't fit them all. I also tried to compensate the shear by measuring exactly how much shear deformation there was and applied a side push to correct it. That worked if the setup was on the optical table, but it is very hard to think of anyway to do this side pushing correction when the steel frame was sealed in a container and immersed in a liquid nitrogen bath.

So, eventually I decided to abandon Deegan's design and shifted back to Hauch's setup. Of course, it is impossible to cool the whole apparatus down to liquid nitrogen temperature, but that is not really necessary. All that is required is to have the silicon sample to crack under 100 Kelvin environment, so I decided to enclose the silicon sample and the steel frame with a very soft Aluminum box and left all the forcing mechanism

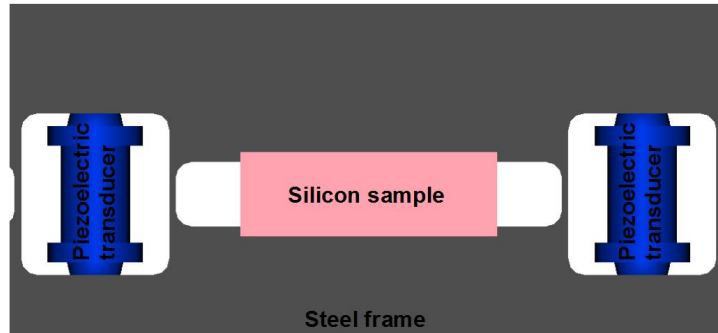


Figure 2.16: Robert Deegan’s three-hole frame design. This design would work if everything functioned ideally, but the reality is that the world we live in is far from ideal. So, the two piezoelectric transducers can be misaligned with respect to each other and not perfectly perpendicular to the major axis of the frame. The frame is very vulnerable to any tiny amount of shear force. So in practice, this design does not work.

out. Then I filled the aluminum box with liquid nitrogen and created a low temperature environment just around the steel frame. (a) of Figure 2.17 is a real photo of my setup (red lines outlined the aluminum box) and (b) is a schematic top view of the setup while the box was outlined by red dashed line. Four threaded steel rods went through small holes cut on the side of the box and connected the steel frame to the forcing bars. The holes were sealed with plastic epoxy commonly used on fish tanks, the coupling of the box to the rest of the system was negligible because the epoxy is very flexible and the spring constant of the box is very small compared to that of the steel frame.

The box setup proved to work. I got some decent straight breaks with clean crack surfaces. But, immediately I ran into another difficulty.

2.2.5.2 Wafer sliding

It seemed that the energy release rate of the modified Whomper was much higher than Hauch used to get. The only difference was that he used glue while I was using static

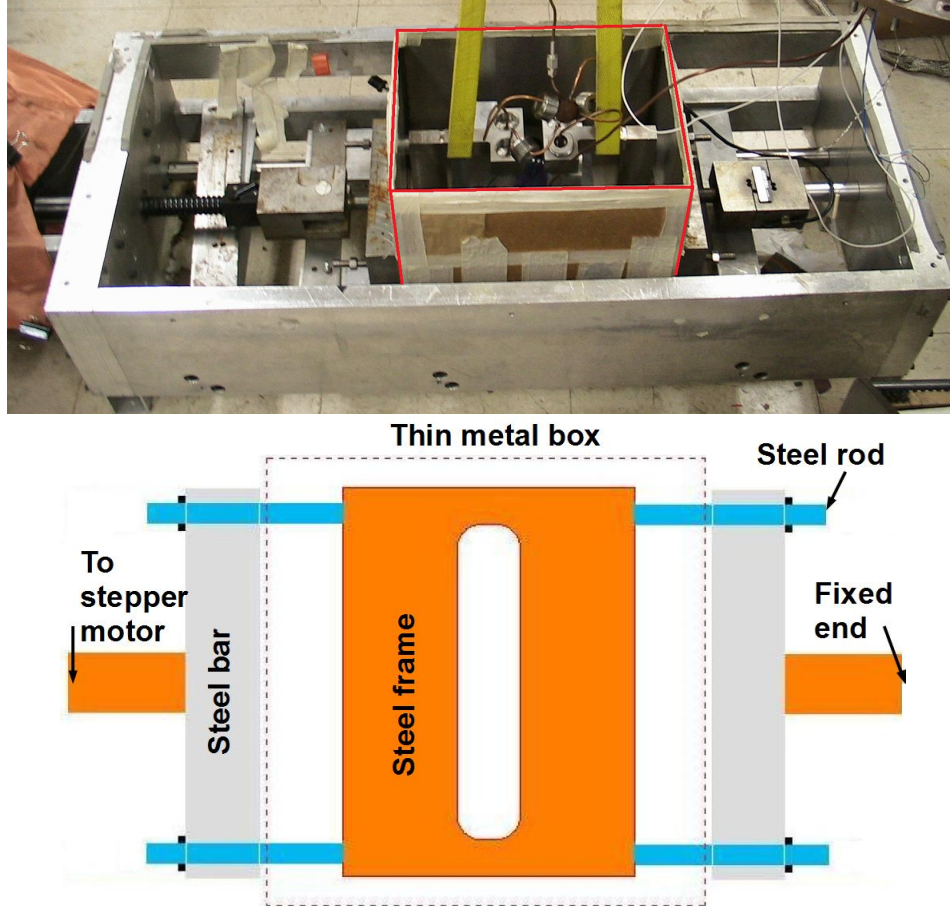


Figure 2.17: Boxed low temperature environment surrounding Whomper, The upper sub-figure is a real photo of the setup; the lower sub-figure is a schematic drawing of the essential components. A stepper motor is connected to the left-most steel rod (orange), a steel bar redistributes the load to two smaller rods (blue) which in turn act upon the steel frame. The steel frame is still the platform for conducting the fracture experiment. A symmetrical design refocuses all the load back to the right most steel bar (orange), which is then fixed to a stationary point on the wall of the outer aluminum structure. Since the stepper motor is also fixed to the outer aluminum structure on a symmetrical point of the opposite wall, the force loop is completed. This design has the advantage of aligning itself and displays much stronger resistance to shear forces than the design in Figure 2.16.

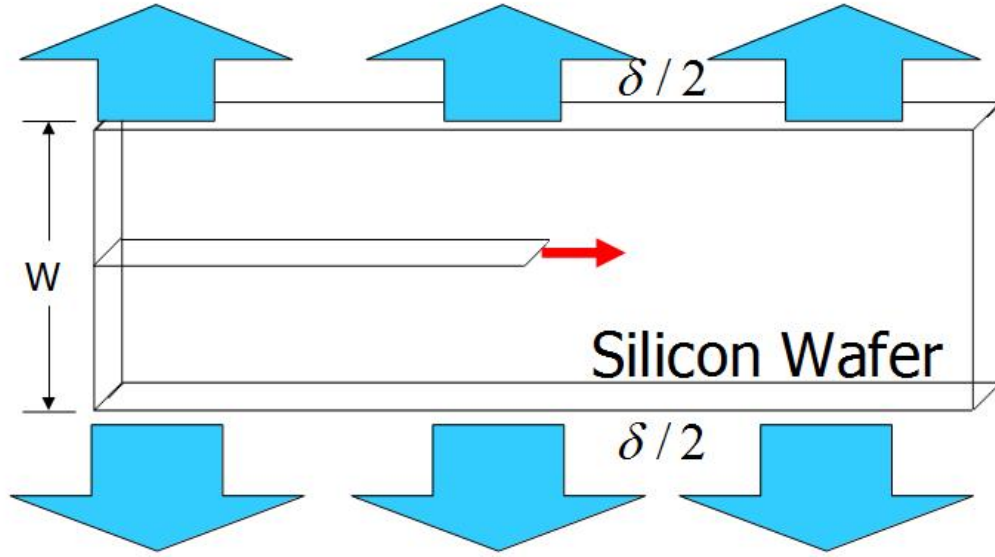


Figure 2.18: Schematic drawing of mode I crack and quantities used for calculating energy release rate

friction to hold the wafer fixed to the frame. So, what was going wrong?

First, let me show how to calculate the energy release rate, which is exactly the same way as Hauch did. Figure 2.18 illustrates a schematic mode I break. The red arrow points to the direction of the crack propagation and all relevant quantities for calculating energy release rate (G) are shown.

The energy release rate for such a system can be calculated by equation 2.4.

$$G = \frac{1}{2} \frac{E\delta^2}{(1 - \nu^2)W} \quad (2.4)$$

Where E is Young's modulus and ν is Poisson's ratio. W is the width of the silicon strip that was stretched, also corresponds to the width of the middle window of the steel frame. Finally, δ is the amount of stretch, which is directly measured by a set of inductive sensor.

For Hauch, since he glued the wafer to the frame, it was just necessary to measure the displacement of the two edges of the middle window of the steel frame for δ .⁵

⁵Hauch actually calibrated the yield of the glue and compensated it in his calculation for δ .

While assuming that static friction with sufficiently strong normal force could hold the wafer fixed to the frame as effectively as glues. I was also measuring the displacement of the edges of the middle window of the steel frame for δ .

An unrealistically high energy release rate could only mean two possibilities:

1. The inductive sensor was not working properly.
2. The wafer was sliding while the frame was stretched. That is, the amount of extension of wafer is less than the relative displacement of the edges.

To rule out the first possibility, I sent the inductive sensor back to the manufacturer and asked for a complete calibration. Also, I did consistent tests between the two (three later) sets of inductive sensors by having them measure exactly the same displacement. I even did a laser interference experiment to calibrate the inductive sensor by myself. The inductive sensor was working perfectly.

So, I had to conclude that the wafer was sliding even when it was well within the static friction threshold. Eventually, I decided that I had to know how much it slides, how fast it was sliding and what was the relation between the amount of sliding and normal force. All of that will be detailed in part III of this thesis.

2.2.6 Differential loading to catch velocity gap

In order to determine whether there is a velocity gap, it is not enough just to have a clean straight break, because that only gives one the crack speed as a function of energy release rate. What is more vital is to see if a steady propagation of crack is possible as the energy release rate gradually reduces below the Griffith's threshold. That is, one has to get a running crack (usually at a speed of 2-3 km/s) arrested before it breaks the wafer through (the total length of a wafer sample is 3 inch, and a seed crack is around 1 inch.). All that matters is the manner the crack stops. If it stops gracefully (reducing speed continuously back to zero), then there is no velocity gap. Otherwise, if the crack speed suddenly drops to zero from some substantially non-zero value, then there is a forbidden range of velocity, hence the existence of a velocity gap.

In principal, the velocity gap should also be observable by examining the way the crack starts. But, the existence of lattice trapping and the fact that the seed crack is not

long enough to maximize the stress intensity factor makes it improper to argue that a rapid rising of crack speed at the beginning of the propagation is due to the existence of a velocity gap. That is, a crack will always start to propagate only when the energy release rate right ahead of it is substantially more than the minimum to support a crack to propagate.

The experimental method of creating a gradually decreasing energy release rate is to have a differential loading, that is, to stretch the wafer harder on one end (the end where the seed crack was implanted) and less on the other end. It was relatively easy for Deegan to create and manage a differential loading (refer to his design in figure 2.16) because a gas regulating system was built to control the gas pressure of individual bellows, hence the force exerted by each bellow can be separately controlled. In order to realize differential loading in my setup, I inserted a weak bellow into one end of the rectangular hole of the steel frame (figure 2.19 provides a close up look of the bellow in action). While conducting the experiment, I first drove the motor to stretch the wafer to about the Griffith's threshold, and then slowly inflated the small bellow until the wafer cracked.

2.3 Data Analysis and Discussion

After all the efforts of troubleshooting and perfecting every step of the experiment, I got a success rate of 1 out of 10. (Not that bad considering that the previous overall record was less than 1 out of 100.) So, before I show the only sets of good data, let me show how a typical bad set of data looks.

2.3.1 Data of partial cracks

For both room temperature and low temperature fracture experiment, most commonly seen are those of partial cracks as shown in figure 2.20. Partial crack is a term used in this thesis to stand for a particular fracture experiment where the crack propagates in a jerky fashion that it starts and stops multiple times and usually never reaches speed higher than 1 km/s. For those partial cracks, there are features on the crack surfaces resemble those reported by Ilan Beery et al[36], and indeed those cracks ran at a speed of a few tens to a few hundreds of meters per second as they had discovered, but that doesn't mean that there isn't a velocity gap, because those cracks never ran at a steady state. Whether it is

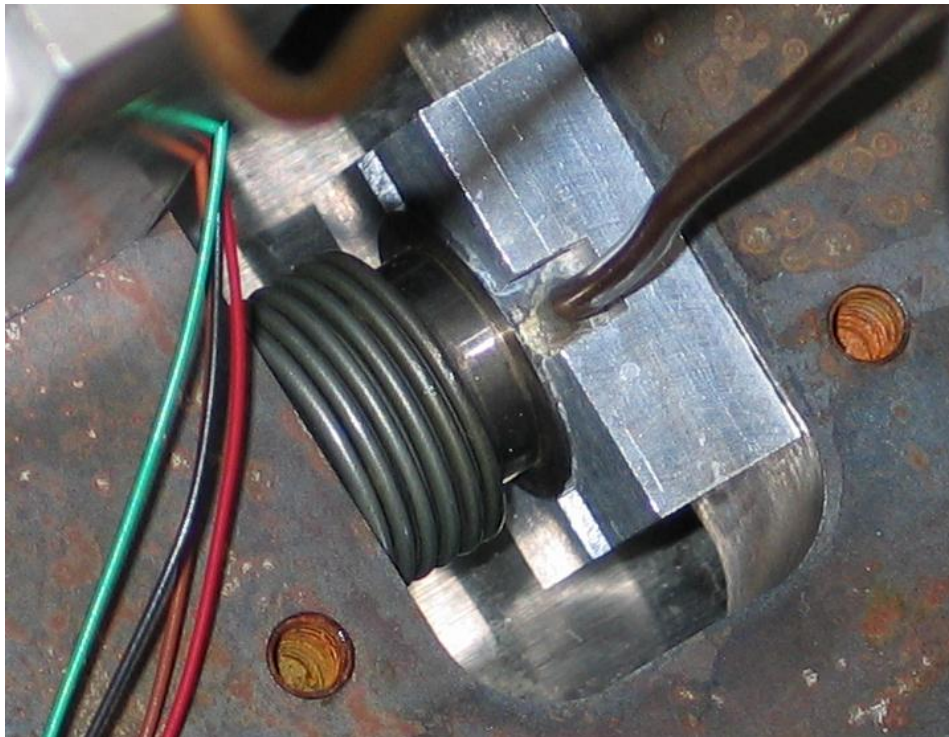


Figure 2.19: Bellow for differential loading

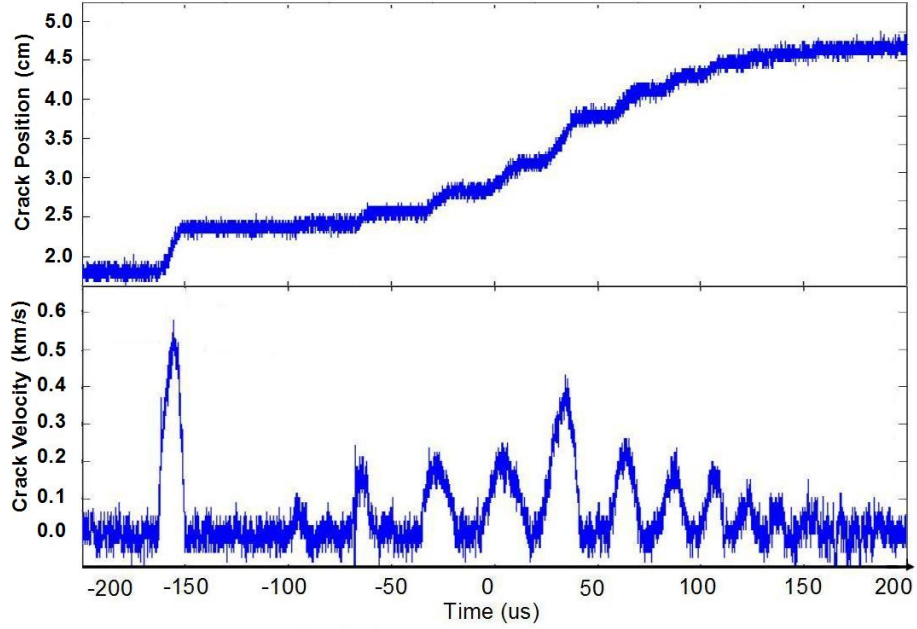


Figure 2.20: Length and velocity records of cracks moving in jerky fashion (partial cracks). Note that the velocity never exceeds 1 km/sec and never reaches a steady state. These experimental signals are characteristic of misaligned samples that leave behind rough fracture surfaces.

actually another manifestation of velocity gap remains to be carefully examined.

2.3.2 Data of a good room temperature crack

Figure 2.21 shows a typical data set for a good room temperature crack of silicon, which contains only one propagation process and has stabilized voltage reading before and after it. The upper panel is the crack tip position as a function of time and the lower panel is the corresponding velocity profile of the crack. In order to produce this, the resistance of the crack is measured before and after the crack. That information combined with the resistivity of the wafer are used to construct a similar curve as shown in figure 2.13, which serves as the conversion table to translate the voltage readings to crack tip positions. The velocity profile is obtained by doing an analog differentiation on the same voltage data and applying the same conversion rules.

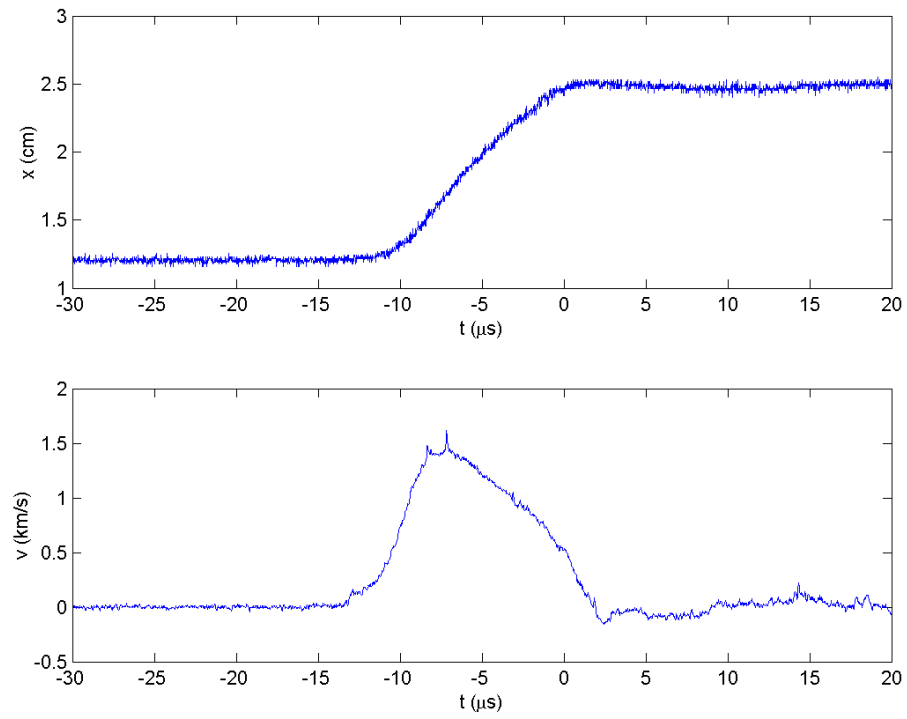


Figure 2.21: A good room temperature break; the crack reaches a velocity over 1 km/sec and holds it for several microseconds. The distance is calibrated by noting the final position of the crack tip after the experiment is completed.

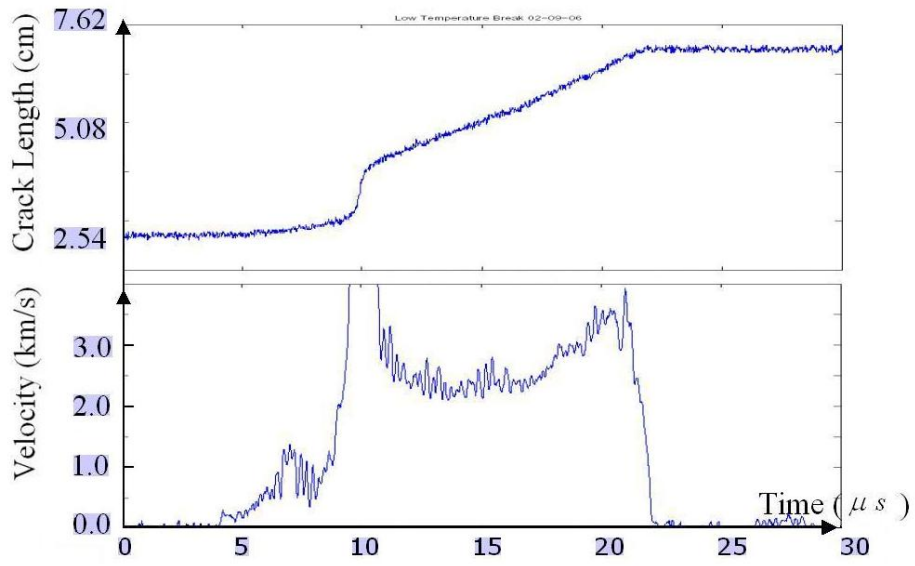


Figure 2.22: A good low temperature break.

2.3.3 Data of a good low temperature crack

Figure 2.22 shows a good data set of low temperature crack. Even though the silicon sample is exactly 7.62 cm long and it seems that this crack runs dangerously close to that limit, it is obvious that this crack is arrested because otherwise the voltage reading will shoot over limit and the data will present a huge vertical jump instead of the flat plateau seen in this case.

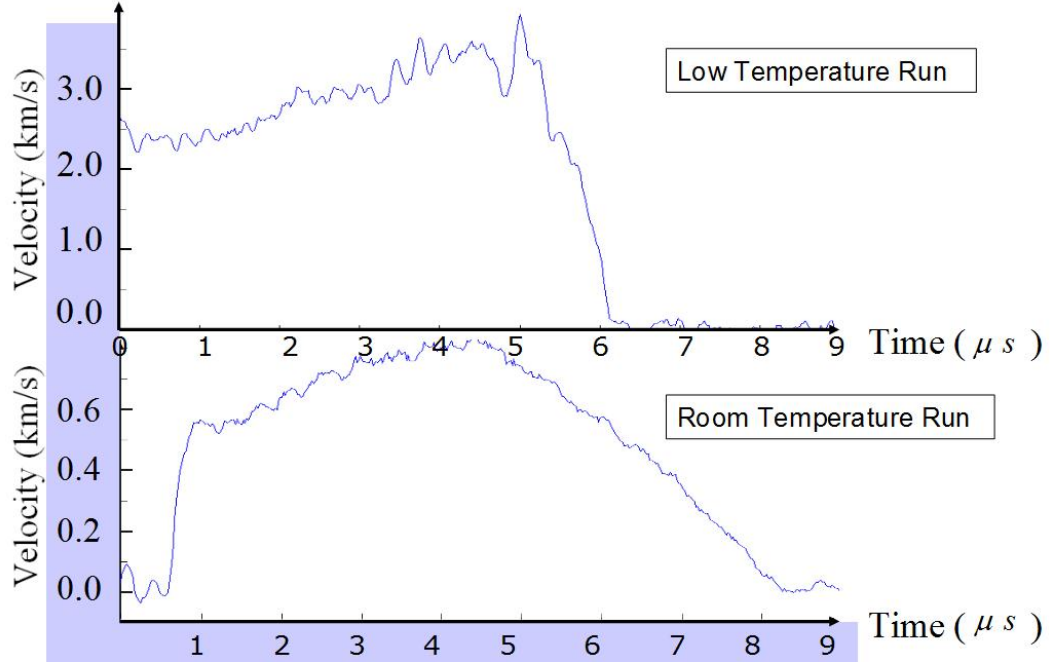


Figure 2.23: Comparison of the arrests of cracks at room temperature and liquid nitrogen temperature under comparable energy release rates reveals the existence of a velocity gap.

2.3.4 Velocity gap confirmed

Comparing the manner the crack was arrested at room temperature and liquid nitrogen temperature (figure 2.23) provides the best indication yet obtained that a velocity gap does exist. For the arrest at room temperature, it takes about $4 \mu s$ for the crack to descend from 0.8 km/s to zero. While arrest at low temperature takes only about $1 \mu s$ and it jumps from above 3 km/s back to zero. The gradual arrest at room temperature is attributed to thermal fluctuation effects and the abrupt arrest at low temperature is believed to be a strong evidence for the existence of a velocity gap.

2.4 Conclusion

After several years of struggle, I managed to obtain two sets of good data that indicate the existence of a velocity gap. In combination with a small number of runs previously obtained

by Deegan, they constitute the best evidence to date that low-temperature fracture of silicon differs from room-temperature fracture. All low-temperature breaks arrested more quickly than all room-temperature breaks. Unfortunately, the small number of cases where the phenomenon has been seen and doubts cast by the difficulty of the experiment have left us reluctant to publish. In addition, sliding between frame and sample, which will be documented in the next Chapter, left us without clear knowledge of the precise value of the energy release rate in those few good runs we obtained. Thus despite the effort put into this experiment, I have been forced to leave it still incomplete.

Chapter 3

Friction

3.1 Introduction

The purpose of this Chapter is to discuss a set of experiments concerning frictional motion over very small distances. As mentioned in the introduction, the original purpose of the friction measurements was to calibrate the energy release rate for our low temperature experiment which used friction as the gripping mechanism. But, as the attempts to characterize friction proceeded, they became valuable findings on their own. A conventional picture of friction that most people have in mind is illustrated in figure 3.1. For a small enough applied shear force, static friction force is always equal and opposite of it and hence no motion will occur. As the shear force increases to a value that exceeds the limit of static friction, motion begins. The maximum static friction is determined by the static coefficient of friction multiplied by the normal force ($\mu_s F_n$). Due to the fact that the dynamic coefficient of friction is usually smaller than the static coefficient of friction, the motion will accelerate a bit at the beginning. But, then the dynamic coefficient of friction increase as the relative velocity increases. The interplay of these two factors can produce a slip-stick motion. One typical example was shown in figure 3.2[1].

Few people have ever asked why there is always an equal and opposite static friction force when a small shear force is applied. Or, what is the origin of a static friction force? Some who did ask found themselves facing a dilemma that there shouldn't be any static

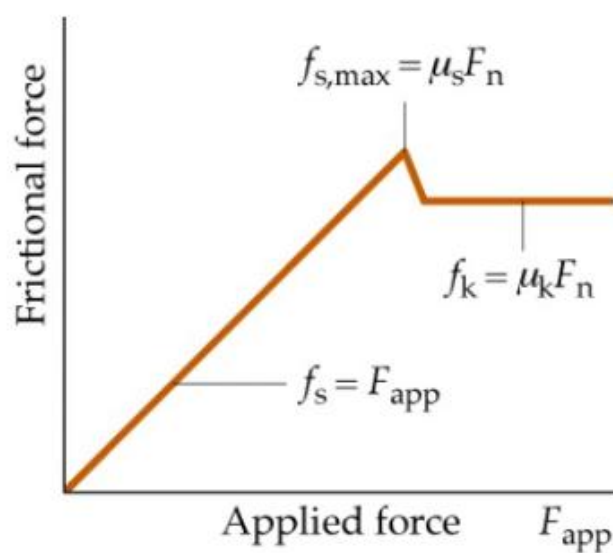
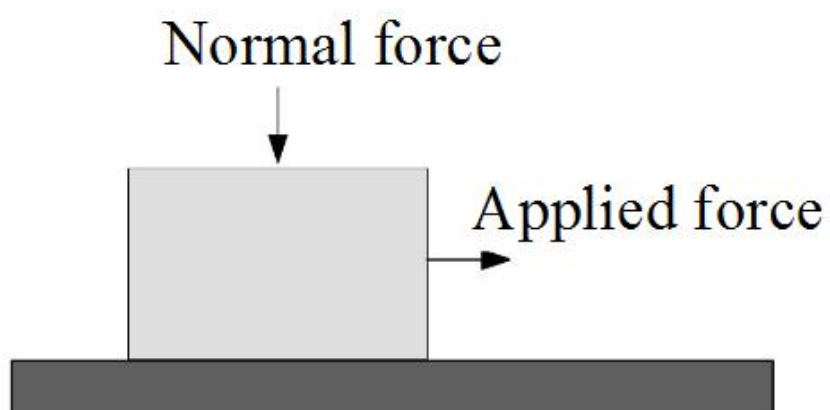


Figure 3.1: Common understanding of friction (The lower portion of this graph is from World Wide Web.)

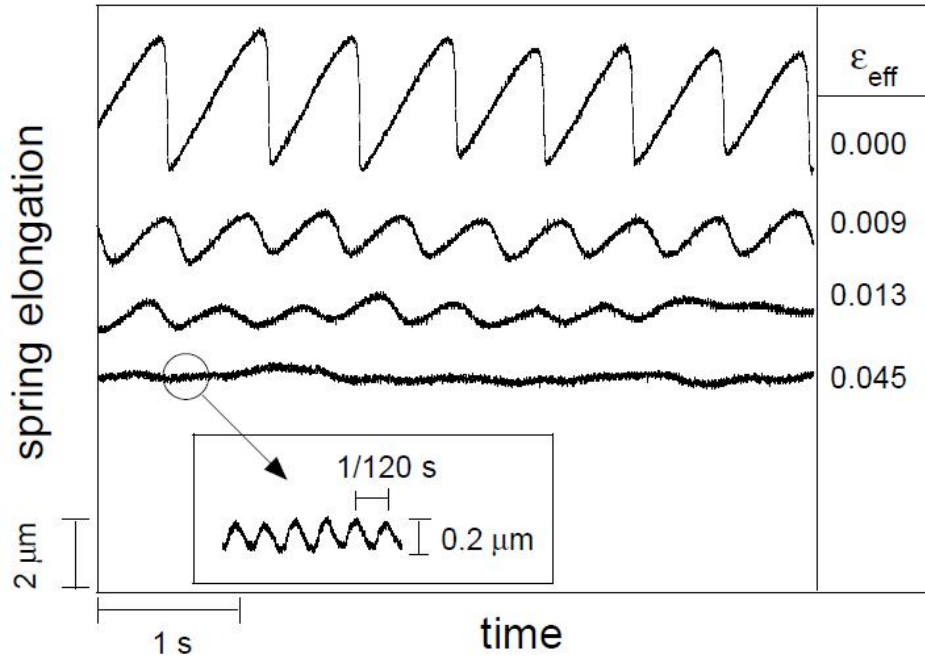


Figure 3.2: Slip-stick motion (This graph is adapted from Cochard's paper[1].)

friction. The argument goes like this:

Most macroscopically flat surfaces look like endless hills and valleys on a microscopic length-scale. When two such surfaces come in contact, only a small portion of the surface is touching the other side as illustrated in figure 3.3. Based on this picture, it is tempting to think of the origin of the static friction as purely geometrical. That is, one needs to provide energy to push one hill to climb over the other. But, the energy is recovered once it passes the highest point of the other hill and starts going downward. Statistically speaking, at any time there will be equal number of hills to climb over one another compared to the hills going down the valley. So, in the macroscopic limit there shouldn't be any energy required to move one surface against another, because there is no energy lost in this picture.

So, does geometry matter at all? I believe it does. In reality, there aren't just hills and valleys, there are also rocks and rivers. That is, there are all kinds of contamination on most surfaces. Robbins[91] et al. argued that if there are particles in between two surfaces moving against each other, then there will be a net energy loss and hence friction. But,



Figure 3.3: Rough surfaces in contact as a conventional picture of friction

again you will need to have the surfaces in relative motion to have friction, which can not explain the origin of the static friction.

A more physical argument for the origin of static friction will have to consider the dynamics on the microscopic level. Once two hills are pressed into each other such as the one circled in red line in figure 3.3, atoms on the surface of one object get close enough to feel the Van der Waals force due to the atoms on the surface of the other object. The detachment of the Van der Waals bonding could cause atoms to vibrate more violently and dissipate energy through mechanical (sound), thermal (heat) and even electrical (ripping electrons from one material to another) means. This still sounds like a physical argument for dynamic friction, and indeed it is. But, now I will argue that it also helps explain the origin of static friction (or just friction in a more unified sense).

When two surfaces just come into contact, a population of asperities has been born. There will be a distribution in sizes of asperities as well as a distribution of shear strengths. And that population will grow due to slow plastic flow, which is known as aging.¹

But, as soon as a shear force is applied, the population of asperities will start to reflect its existence. The two surfaces will move against each other a little bit to create more asperities and certainly some asperities begin to break. It really is a dynamic process which happens on a microscopic scale. If the net gain of asperities is enough to counter-balance the shear force, then the system will be stable and will not show visible motion, which is then still categorized as static friction. The system will be unstable only when the shear force is not counter-balanced by asperities growing. Actually, when the relative motion is quick enough the creation of asperities will be less than the breaking of asperities, which is also why dynamic coefficient of friction is usually smaller than the static coefficient of friction. Once that happens, macroscopic motion starts. Depending on the surface conditions such

¹Maybe just enlarging some of the real contact areas, but in the sense of an average size of asperities it is equivalent. Basically, it is the increasing of the real contact area.

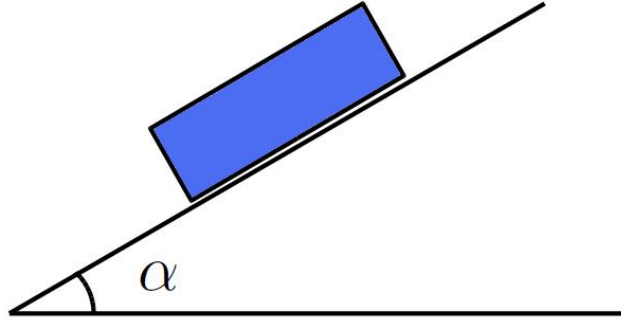


Figure 3.4: Inclined plane experiment between a polished silicon wafer and a machine-ground steel surface.

as flatness, lubrication, and contamination, it could end up smooth sliding motion or a slip-stick motion.

To make a unified approach to the origin of friction, friction can be understood as a dynamic process of continuously forming and breaking of tiny inter-facial cracks on the microscopic length-scale.

3.2 The inclined plane experiment

As the starting point to understand why the silicon samples of our low-temperature experiment were sliding against the steel grips intended to hold it in place, I performed an inclined plane experiment to measure the conventional coefficient of static friction.

The setup of this experiment is very simple (figure 3.4). I put a wafer on the steel frame and slowly increased the incline angle α . The surfaces in contact are exactly the same pair as those I put to measure how much the silicon sample slides. The silicon sample was doubly polished (industrial standard) and the steel frame was machine ground to a surface flatness of less than a micron.²

It is clear that the static friction coefficient can be found by the following equation

²I also conducted the inclined plane experiment for a rough steel surface (sand papered, used type-400.), which only raises the static coefficient of friction by about 20%.

$$\mu_s = \tan(\alpha) \quad (3.1)$$

where α is the maximum incline angle before the wafer begin to show macroscopic slipping.³

The static coefficient of friction so found is 0.18 ± 0.014 (The experiment was repeated 12 (N) times, and the reported value is the mathematical average and the uncertainty of it which is the standard deviation divided by $N^{\frac{1}{2}}$).

3.3 The friction experiment

Additional friction experiments were performed in exactly the same manner as for the fracture experiment except that the wafer was not pre-cracked and two pairs of inductive sensors were glued to the wafer as shown in figure 3.5 to provide careful measurements of sliding between the sample and the grips.

During the experiment, a pair of normal forces N was applied through the pressure blocks to press the silicon sample onto the steel frame. The steel frame was then stretched by a stepper motor. S_{ext} represented how much the stepper motor retracted and was also directly measured as the control parameter of the experiment. S_f represented how much the edges of the middle window of the steel frame was displaced. Additionally, the sample extension S was directly measured by the inductive sensors. If conventional understanding of static friction were correct, then S would equal S_f as S_{ext} began to increase until it reached a point that the internal stress of the silicon sample provided a shear force greater than $2\mu N$.⁴ Once that point was reached S would stay a constant value while S_{ext} and S_f could keep increasing. However, my experimental results indicated that this simple picture was incorrect. Especially since slipping started at the very beginning as S_{ext} started to increase I concluded that a static coefficient of friction μ_0 might not exist at all; instead static friction has a dynamic origin.

³In order to get a reasonably distributed result, I glued the silicon wafer to a metal block. Otherwise, the weight of the wafer is so small and its thickness so thin compare to the other two dimensions that the result scatters over a very wide range.

⁴The reason for a factor of 2 was that there were two interfaces (both sides of the silicon sample were in touch with the same type of steel) contributing static friction.

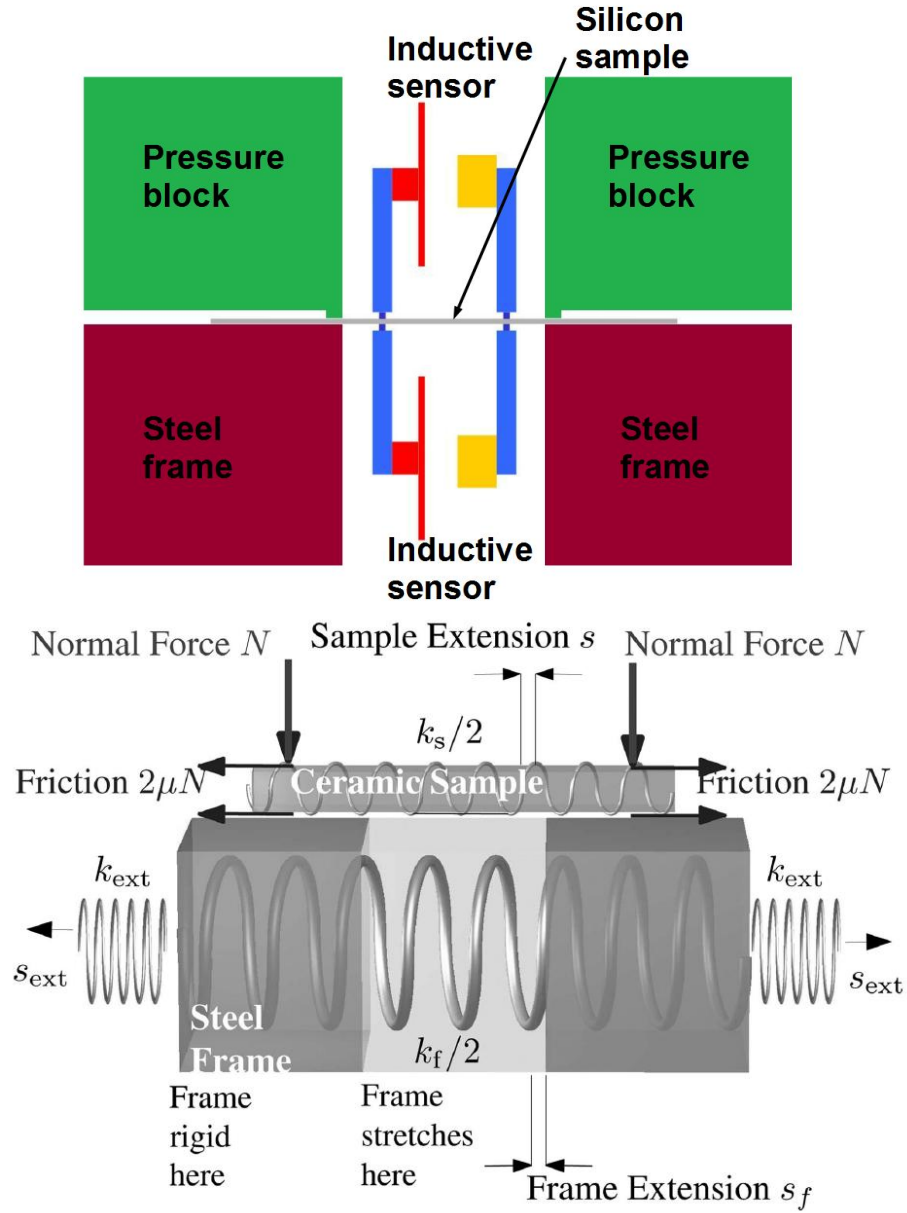


Figure 3.5: Schematic diagram of the experimental setup of friction. The four rods in blue color are the aluminum holders for the two pairs of inductive sensors, which are machined to exactly the same specification.

The reason for using two pairs of inductive sensors instead of one was that the wafer bends slightly when a normal force is applied. This bending will then be magnified (due to the long arm of the holder of the aluminum target) and picked up by the inductive sensor. Obviously, the symmetrical setting of the inductive sensors can be used to eliminate the bending effect (by taking the average of the reading from both sensors). Figure 3.6 shows how much the bending was picked up by individual inductive sensor and how good the cancellation was. The reason for such a good cancellation is that the two sensors have exactly the same height as measured from the surface of the wafer (machining accuracy limit 1/1000 of an inch) and close (see footnote) to exactly the same distance apart. This geometry guarantees that a small deflection due to the bending of the wafer creates equal amount of contraction or elongation of the distance between the inductive coils and their perspective targets. So, the summation of the reading of the two sensors is very close to zero as indicated by the blow-up of figure 3.6. (The two humps in the data was due to the inflation and deflation of the gripping bellows.) ⁵

3.4 Modified rate- and state- friction law

3.4.1 Rate- and state- equation and its modification

The rate- and state- friction law was first proposed by Dieterich[15] in the 1970s based on experimental findings. The dynamics between two contacting surfaces in the microscopic length-scale must be very complicated as it involves forming and breaking of asperities (micro inter-facial cracks) and unavoidably some surface contamination, such as finger oils, water molecules, dust and debris from the broken asperities etc. But a surprisingly simple model with only two macroscopic parameters can describe the motion rather well. The two parameters are the relative velocity and a state variable that evolves as the surfaces slide.

In general, the friction coefficient μ can be understood as the ratio of horizontal force F to normal force N ,

$$\mu = \frac{F}{N} = A \ln(1 + \frac{v}{v^*}) + B \ln(1 + \frac{\theta}{\theta^*}) \quad (3.2)$$

⁵An extra factor of 1.0945 was multiply to the blue curve to reflect a small distance mismatch between holders.

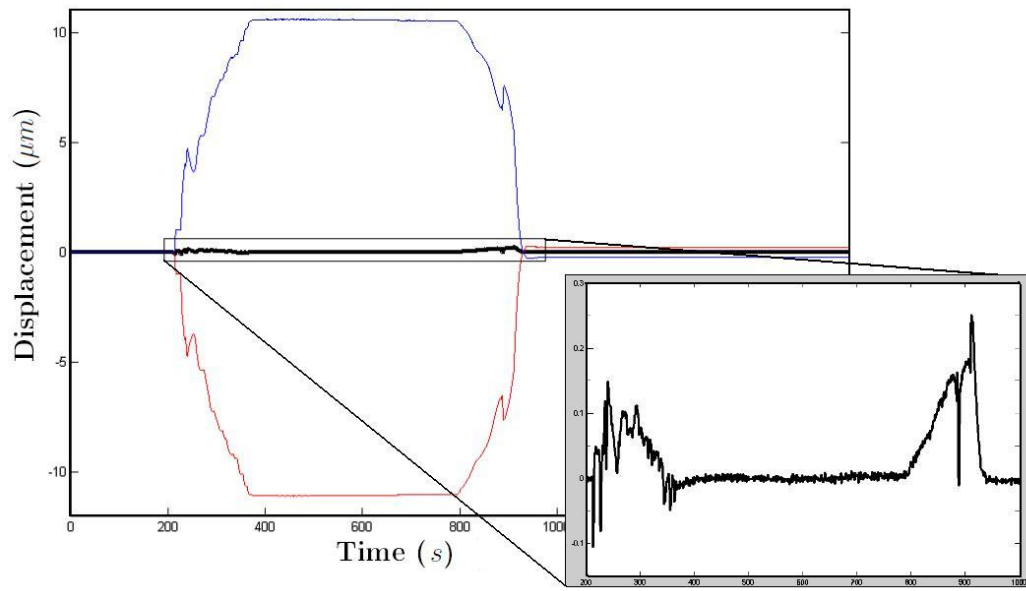


Figure 3.6: The red and gray thin curves were individual readings from each inductive sensor and they varied a lot during the process of inflating or deflating the bellows, but their sum stayed very close to zero as more clearly indicated by the sub-figure, which is a magnified view of the sum of these two curves.

Here A , B , v^* and θ^* are constants, v is the relative velocity of sliding, and θ is a state variable that carries all the information about the population of asperities. This expression differs slightly from the original version because a static coefficient of friction μ_0 is missing. Based on experimental findings, the static friction is an ill defined term and actually comes from the dynamics of the relative sliding. That is, if the state variable and relative velocity vanish, the friction force vanishes as well. This choice is motivated by our inability in experiment to observe any lower threshold of horizontal force below which there is not at first some sliding, which can be most clearly seen in the continuous data (figure 3.7) where the slope of the data (blue curve) is never as steep as the green curve (were there a non-zero static coefficient of friction). The green curve is what one will expect assuming the conventional understanding of static friction is correct. That is, the sample extension S will follow exactly as how much the middle gap of the steel frame is displaced until it reaches a point that the internal stress of the silicon sample is greater than the threshold of static friction. Once that point is reached, S will become a constant even though the steel frame is stretched further. The deviation of the real data (blue curve) to the conventional prediction (green curve) at the very beginning of the curve (Data close to the origin is when internal stress of the sample would be very small.) suggests the absence of the static coefficient of friction. Etsion and Lee and Polycarpou[11] have reported the same phenomenon.

To complete the theory, it is necessary to propose a dynamic equation for the state variable. There are two common expressions for it.

A first form is from Dieterich[15], and is

$$\frac{d\theta}{dt} = 1 - \frac{v}{D_c} \theta \quad (3.3)$$

Where, D_c is a constant that describes a sliding length over which the asperity population reaches a statistical steady state. Another was discussed by Ruina[77] and is

$$\frac{d\theta}{dt} = -\frac{v}{D_c} \theta \ln\left(\frac{v\theta}{D_c}\right) \quad (3.4)$$

These two expressions behave differently in the static case where $v = 0$. The first, Eq. 3.3, predicts aging, which means that the state variable increases linearly in time if the system is stationary, and the friction coefficient increases logarithmically. The second, Eq.

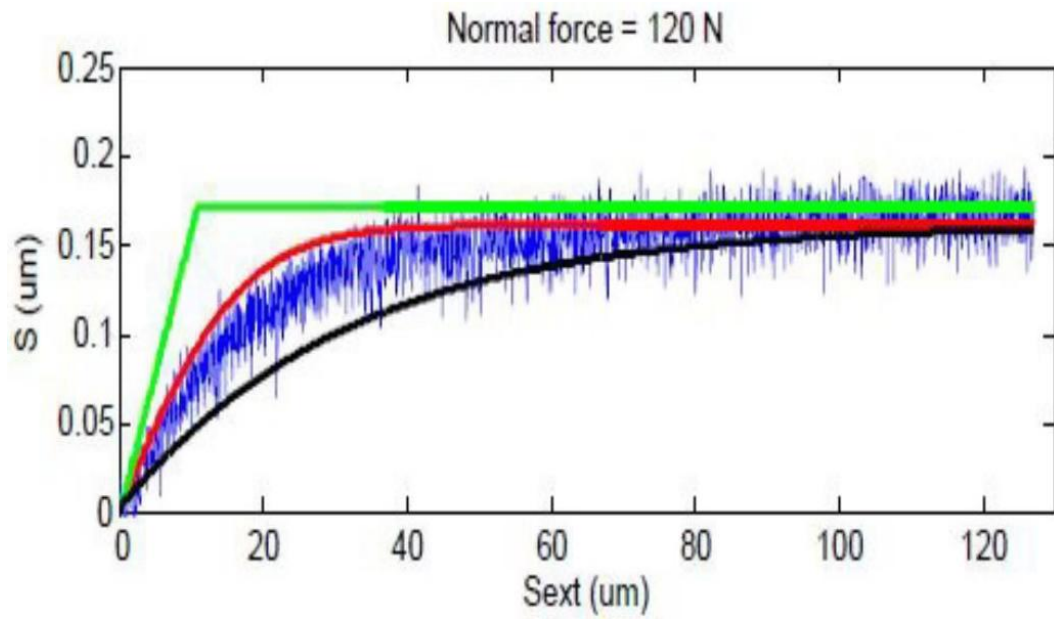


Figure 3.7: One set of continuous data under the normal force of 120 N. The green curve is the prediction of conventional friction, the black curve is the prediction of the modified rate- and state- friction law treating D_c as a material constant while the red curve is the prediction of the same modified rate- and state- friction law but allowing D_c to vary as a function of normal force.

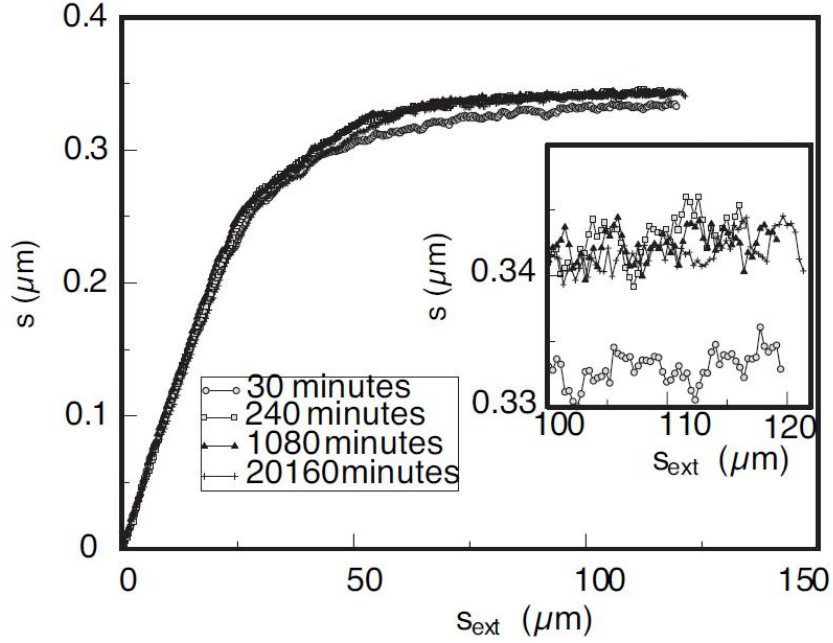


Figure 3.8: I sat the silicon sample on top of the steel frame and waited for four different lengths of time before conducting exactly the same experiment. The results bear no indication of aging except for a slight difference between data obtained after waiting for 30 minutes and the rest of them which were obtained after waiting for much longer time. All the rest of my friction experiment waited for more than 24 hours, so aging should not present itself in any of my other data sets.

3.4, predicts that when the sample is not sliding the state variable does not evolve.

There is compelling experimental evidence dating back to Coulomb that the strength of static frictional contacts increases over time[14]. However, this evidence was obtained in specific experimental systems such as wood on wood or rock on rock. Berthoud et al. (17) show that aging rates of polymeric systems drop rapidly as a function of temperature below the glass transition temperature. Thus for a system such as ours, with large yield stresses and far from any melting temperature, one might expect aging effects to be very small. We show in Fig. 3.8 that the experimental results of silicon on steel we have studied give no evidence for aging on a time scale ranging from half an hour to 2 weeks.

Because of the absence of aging in our experiments, we have looked for a generalization of both Dieterich and Ruina's equations. We suppose that there are two state variables θ and ϕ , where ϕ is proportional to the aging time of contacts, and θ describes how the

contacts evolve during sliding.

Equations implementing this idea are

$$\frac{d\theta}{dt} = \frac{v}{D_c} \left(\frac{1 + \phi}{1 + v/v_\theta} - \theta \right) \quad (3.5)$$

$$\frac{d\phi}{dt} = \alpha N / \tau - \frac{v\phi}{D_c} \quad (3.6)$$

where N is the normal force, τ is a yield stress, and α is dimensionless.

Ruina similarly presents equations for a pair of state variables. To understand the behavior of these equations, it is useful to consider a situation where the horizontal force increases slowly from zero and then holds at a constant final value F . For almost all initial conditions, the sample initially begins to slide with nonzero velocity v and then heads toward solutions where v and θ are time-independent. The time-independent solutions are of two forms. If F is below a critical threshold, the final solution has $v = 0$ and is given by $F = B \ln(1 + \theta/\theta^*)$. This solution corresponds to a system gripped by static friction. However, these solutions are only stable so long as θ is less than a critical value of $1 + \phi$. When F/N is larger than $B \ln(1 + (1 + \phi)/\theta^*)$, the steady solutions instead have nonzero v and $\theta = (1 + \phi)/(1 + v/v_s)$. This situation corresponds to sliding friction.

The critical shear force that divides these two regimes is

$$\mu_s = \frac{F}{N} = B \ln(1 + (1 + \phi)/\theta^*) \quad (3.7)$$

which we identify with the static coefficient of friction. If instead one waits for a long time (T) before beginning to ramp the force up from zero, ϕ increases by $\alpha NT/\tau$, the critical shear force increases by the log of this value, and thus the equations can describe the phenomenon of aging.

In view of the fact that our experiments show no aging, we simplify to

$$\frac{d\theta}{dt} = \frac{v}{D_c} \left(\frac{1}{1 + v/v_\theta} - \theta \right) \quad (3.8)$$

and the expression for the static coefficient of friction simplifies to

$$\mu_s = \frac{F}{N} = B \ln(1 + 1/\theta^*) \quad (3.9)$$

The transition to sliding at this critical force value can be either sub-critical or super-critical depending on the values of A and B.

3.5 Using the modified rate- and state- equation to fit our data

We now apply the modified rate- and state- friction equation to fit our data.

First, we write down equations correspond to the experimental geometry shown in lower portion of Figure 3.5. We assume that the experiment is symmetrical about the horizontal midpoint and focus on the right-hand side. The amount the sample has slipped is $x \equiv S_f - S$. Denote the force of friction by μN . In our experiments, $s > 0$, and friction pulls the right-hand side of the sample to the right. Assuming that none of these quantities changes sign, and neglecting inertia, mechanical equilibrium requires

$$k_s S = 2\mu N \quad (3.10)$$

$$(S_{ext} - S_f)k_{ext} = 2\mu N + S_f k_f \quad (3.11)$$

To simplify the equations further, define

$$C_{ext} = \frac{k_s k_{ext}}{k_s + k_{ext} + k_f} \quad (3.12)$$

$$C_x = \frac{k_s(k_f + k_{ext})}{k_s + k_{ext} + k_f} \quad (3.13)$$

Thus, the two mechanical equilibrium equation can be transformed as

$$2\mu N = C_{ext} S_{ext} - C_x x \quad (3.14)$$

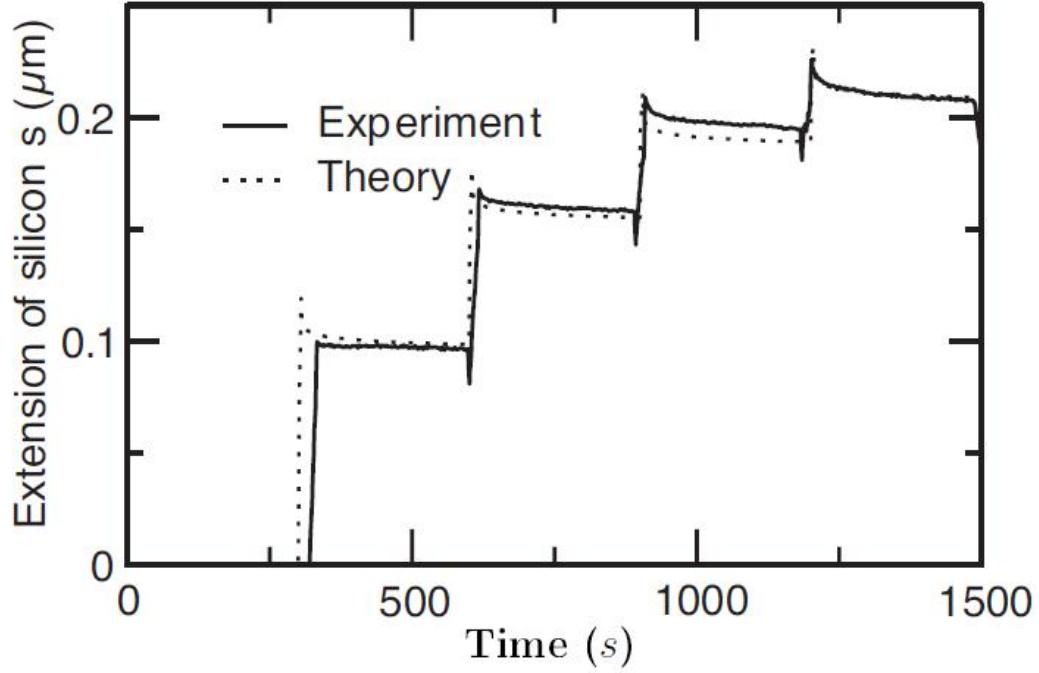


Figure 3.9: Step data; The normal force for this data set is 180 N and it was held fixed throughout the experiment.

coupling this to the dynamic equation of θ (eq. 3.8), proposed functional form of μ (eq. 3.2) and recognizing the definition of relative sliding velocity as $\frac{dx}{dt} = \frac{d(S_f - S)}{dt} = v$ give us a complete set of equation to describe the sliding motion between two surfaces.

In the limit when one increases S_{ext} very slowly and measures S , which was the condition for the continuous data, a closed form solution for S_{ext} can be obtained as

$$S_{ext} = \frac{k_s S}{C_{ext}} - \frac{C_x D_c}{C_{ext}} \ln(1 + \theta^* (1 - e^{k_s s / 2BN})) \quad (3.15)$$

So, we first fit the continuous data with the quasi-static solution given by eq. 3.15. The result was shown in figure 3.12. with the spring constants measured independently (The spring constant of silicon was calculated from its Young's modulus and Poisson's ratio). The best fits to these experiments set the values of D_c and θ^* , and B is determined from Eq. 3.9.

To obtain the rest of the fitting parameters, we have relied upon direct integration

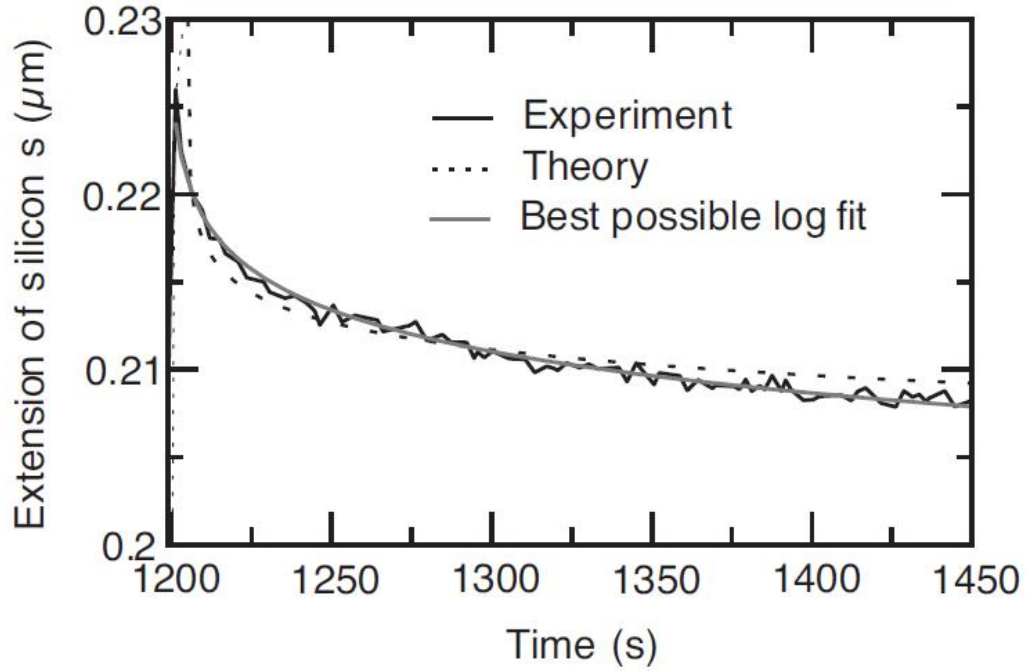


Figure 3.10: Slipping of the wafer as the boundary condition was fixed

of the dynamic equations. Figure 3.9 compares experimental results in which one repeatedly stretches the sample and waits a fixed period of time. The parameters (A and v) are determined by searching for the best fit. When slipping velocities v are much larger than the cutoff velocity v^* , the dynamic equation has solutions where the slip x is logarithmic in time, which was confirmed experimentally as shown in Figure 3.10 (which is a magnified “step” in figure 3.9), this logarithmic slip is observed until displacements become too small to measure accurately. Thus, we cannot really determine the cutoff velocity v^* but only say that it is less than $10^{-5} \mu\text{m/s}$.

Figure 3.11 indicates the physical quantities that I measured for the friction experiment. k_s is the spring constant of the sample (calculated from Young’s modulus and Poisson ratio), k_f is the spring constant of the frame (measured independently). and k_{ext} is the overall compliance of the rest of the system (measured independently). Sample extension S is how much the sample was stretched, S_{ext} is how much the overall system was stretched, and S_f is how much the middle window was displaced. S_{ext} can be viewed as the control variable and S can be taken as the response. The normal force N became a tunable

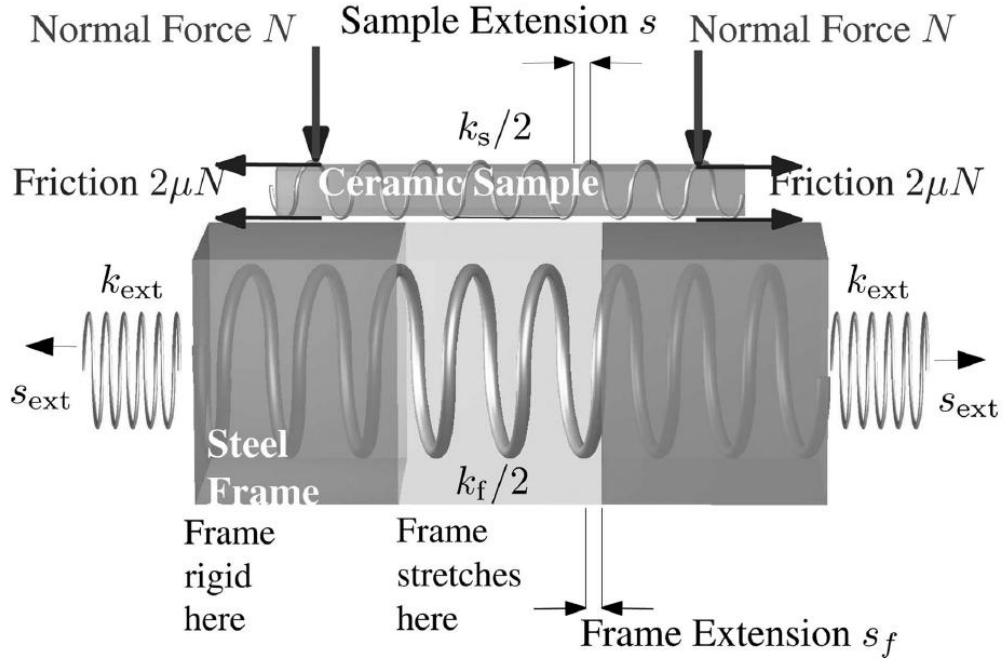


Figure 3.11: Illustration of the quantities measured for the friction experiment

parameter. If N is zero, the wafer should not be stretched at all, because the only force that stretches the wafer was the friction force. On the other hand, if N is very large S should approach S_f .

I used two slightly different ways to conduct the experiment:

3.5.1 Step Data

In the first, I ramped up S_{ext} as quickly as the machine was capable of responding and then stopped for a fixed period of time. The distance between the edges of the middle window was fixed during that time as confirmed independently while measuring the compliance of the frame.

A typical step data set is shown in figure 3.9. The normal force for this set of data was 467 N. The theoretical fit was based on the modified rate- and state- friction law.

A simple calculation can demonstrate that the conventional understanding of friction will fail to predict the behavior shown in figure 3.9.

It is well known that the Young's modulus of single crystal silicon in the [111] direction is 168.9 GPa. So, the spring constant of the wafer sample is

$$k_s = E_{[111]} * \frac{A}{W} = 168.9 \text{GPa} * \frac{3.0 \text{inch} * 380 \mu\text{m}}{1.3 \text{inch}} = 1.48 \text{e}8 \frac{N}{m} \quad (3.16)$$

For an extension of $0.2 \mu\text{m}$, the shear force will be

$$k_s * S = 1.48 \text{e}8 \frac{N}{m} * 0.2 \mu\text{m} \approx 29.6 \text{ N} \quad (3.17)$$

The static threshold is supposed to be

$$2 * \mu * F_N = 2 * 0.18 * 467 \approx 168 \text{ N} \quad (3.18)$$

That is, the conventional understanding of static friction will predict that the wafer shouldn't slide at all (even at the maximum stretch of the experiment), while the experiment showed quite the opposite, and the continuous data will further illustrate that the sliding happened almost immediately after the frame was stretched at which moment the shear force due to the extension of the wafer was nearly negligible.

3.5.2 Continuous data

To further validate the proposed rate- and state- friction law, I also conducted a series of experiment where the change of S_{ext} was continuous and fairly slow (5 times slower than the "jump" of the step data). Figure 3.12 shows the data and three different ways of fitting. The green curve gives the prediction of the conventional understanding of friction. The black and red curve were based on the proposed friction law. The difference is that the black curve held D_c as a constant while the red curve allowed D_c to be proportional to the normal force. D_c is one of the fitting parameters in the dynamic equation for the state variable. (Please refer to equation 3.4.) The physical meaning of D_c is believed to be a characteristic length-scale of the asperities. It is not clear why allowing D_c to be proportional to normal force gives a slightly better fit.

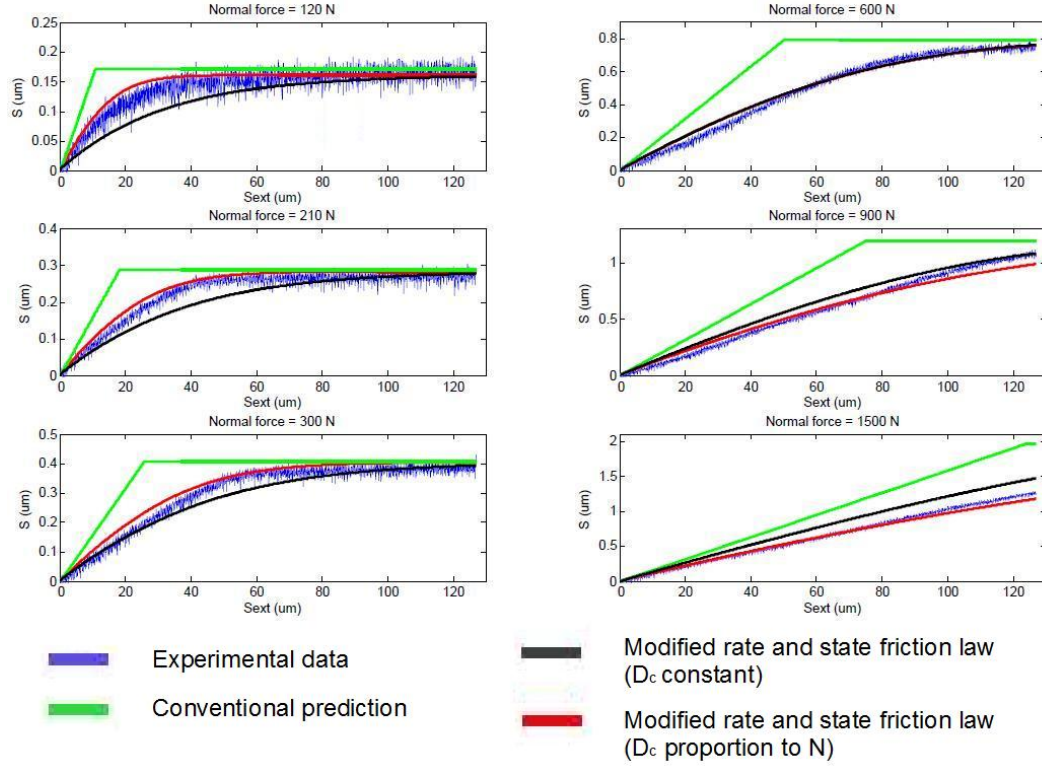


Figure 3.12: Continuous data from experiments where the normal force was constant and shear force increases slowly and linearly. The green curve shows the sample response that would be expected from the conventional theory of static friction. The sample would stretch with the frame up to the limit of static friction and then slide freely. Instead, as shown by the experimental data in blue, the sample always moves less than predicted. I provide two fits to the data based on the modified rate and state friction law. The first of them (black) treats the asperity length D_c as a constant. The second of them (red) allows D_c to vary linearly with normal force. All parameters of the model are held constant across all six panels.

3.6 Conclusion

For hundreds of years, there have been certain basic facts about friction that have not been questioned. One of them is that for any given level of normal force, there is threshold in shear force below which no motion is possible. Once this threshold is reached, the solid will begin to slide, and dynamic friction takes over. Even specialists in the modern theories of friction have retained the concept of static friction in their models.

With the experiments reported in this Chapter, I have shown that the distinction between static and dynamic friction is not well defined, and only seems natural when measurements of motion are not sufficiently accurate. When motions are measured down to the nanometer scale, objects supposedly held still by static friction are not really static at all. They move in predictable and reproducible ways. Furthermore, the mathematical laws that govern their motion appear to be identical to those now thought to describe dynamics friction. Some further work here is called for, since we have not yet shown that the parameters in the mathematical models we use simultaneously describe the very slow motions investigated here and the more rapid motions traditionally used to obtain rate and state theories of friction. However it seems we have obtained a unified picture of static and dynamic friction, one where the different types of motion are due to different force levels and loading histories. This work has been published in PNAS[93].

Chapter 4

Granular Simulation

Experimental study of the internal structures of a granular system is difficult. Nevertheless, Behringer[6, 89] etc. used the birefringent pattern of photo-elastic disks to study the force chain distribution in a 2-D system. Seidler[21, 72, 84] etc. applied X-ray micro-tomography to measure the position of every granular particle in a 3-D packing. Those experimental techniques are great for studying static properties, but are difficult to implement for studying dynamic properties. There is an experimental setup that is designed specifically for dynamic purposes, which is a huge 2-D air-table run by Trodec[40] etc., but their main focus is to study the motions of particles in the gas phase.

MD simulations of granular system have become a complementary tool for scientists to study detailed particle motions at the microscopic length-scale in order to better understand some of the intriguing properties of a granular system.

4.1 Preparation of a confined granular system

4.1.1 LAMMPS' implementation of the force-displacement relation

The version of LAMMPS I used was last updated on Sep-28-2008. In that version of LAMMPS, the force-displacement relation between two granular particles was not correctly implemented in the sense that the calculated result did not match the equations given by the manual. So, I modified the source to implement the Hertz contact force correctly and

ran all my simulations on it. (Please refer to appendix 6.2 for details of the modification.)

After the modification, the interaction between two balls are described by the following formula:

$$\overrightarrow{F_{Hertz}} = \sqrt{d-r} \sqrt{\frac{R_i R_j}{R_i + R_j}} [(k_n(d-r)\overrightarrow{n_{ij}} - m_{eff}\gamma_n\overrightarrow{V_n}) - (k_t(d-r)\Delta\overrightarrow{s_t} + m_{eff}\gamma_t\overrightarrow{V_t})] \quad (4.1)$$

Where $d = R_1 + R_2$ is the contact distance between two balls of radius R_1 and R_2

r is the distance between the centers of contacting balls, $r = \sqrt{(x_1 - x_2)^2 + (y_1 - y_2)^2}$

k_n is the elastic constant for normal contact, $k_t = \frac{2}{7}k_n$ (LAMMPS convention)

γ_n is the viscoelastic constants for normal contact, $\gamma_t = \frac{1}{2}\gamma_n$ (LAMMPS convention)

$m_{eff} = m_i m_j / (m_i + m_j)$ is the effective mass of two balls of mass m_i and m_j

V_n is the normal component of the relative velocity, and V_t is the tangential component of the relative velocity

$\overrightarrow{n_{ij}}$ is the unit vector between the centers of two balls

$\Delta\overrightarrow{s_t}$ is the tangential displacement vector (truncated to satisfy a frictional yield criterion)

Obviously, the first term in the square bracket is the normal force and the second term is the tangential force. The implementation of the tangential force is still not very physical. It simply relates the tangential spring constant and tangential viscoelastic constant to their respective normal direction constants by two arbitrary ratios $\frac{2}{7}$ and $\frac{1}{2}$ (This limitation has been lifted in the newer version). This convention has been commonly used in literature, but a more physical implementation, such as that proposed by Mindlin[69] and Dereciwicz[68] should be implemented to generate more accurate results. Due to the time constraint, I didn't implement Mindlin tangential force to my modified code, instead I stuck to LAMMPS convention for the tangential force calculation.

4.1.2 packing generation and boundary conditions

To minimize the complexity and maximize efficiency LAMMPS left out all the pre- and post- processing to supplemental codes and software. So, I used another program called

PFC2D.¹

The initial configuration of the system was a 2-D granular gas. A loose granular packing containing 5,000 balls in a 10 cm by 10 cm 2-D simulation box was ported from PFC2D with volume fraction about 0.78 (The packing is not confined yet.). The horizontal direction is defined as the X-axis and the vertical direction is defined as the Y-axis. It was a poly-disperse granular system with ball diameters evenly distributed between 0.06 cm to 0.08 cm. The material properties of the constitutive grains were assigned based on the properties of common glasses, which has Young's modulus $E = 72 \text{ GPa}$ and Poisson's ratio $\gamma = 0.1$. The initial temperature of the system was zero (all velocity components of all balls were set to zero). The coefficients of friction in ball-ball interaction and ball-wall interaction were all set to 0.1 from the beginning of the simulation. To confine the system, the top wall was moved to the negative Y direction gently using a half period cosine profile, $y = A \cos(\frac{2\pi}{T}t)$; $A = -0.1 \text{ cm}$ $T = 0.08 \text{ s}$ while the bottom wall was fixed throughout the simulation. A periodic boundary condition was applied to the horizontal direction. That is, if a ball moves out from the left boundary of the simulation box, it will re-enter the simulation box from the right at the same height. The integration time-step for the underlying Newtonian dynamics is set to 2.0×10^{-8} second, which is smaller than the time for a pulse to travel through the minimum ball radius. Tests using smaller time-steps show no significant difference in dynamics. That is, 2.0×10^{-8} second is a small enough time-step to have a converging numerical result. This downward movement of the top wall was repeated several times to reach a desired final location. Then the system was relaxed while the boundaries were all held fixed. A stable reading of force acting on the bottom wall was reached as the system quickly dissipate its kinetic energy. After that, the system was subject to 100 cycles of large amplitude high frequency (amplitude as large as $1 \text{ e} - 4 \text{ cm}$ and frequency as high as 1 MHz) vibration from the top wall to further ensure that the micro-configuration was stable and wouldn't collapse if pulses or sine waves were to transmit through the system later. Finally, the system was relaxed² again for much longer time such that virtually all kinetic energy was damped out. The system was then ready to be studied.

¹PFC2D is itself a fully functional commercial MD code. I was able to obtain a demo version of it and ran many of the prove-of-concept test script on it. For more information on PFC2D, please visit the vendor's website : <http://www.winternet.com/~icg/pfc.html>.

²All relaxation was done while holding all boundary conditions fixed.

4.2 Static properties of the prepared system

A snapshot of the prepared system and its contact force network³ is illustrated in figure 4.1. One obvious characteristic of the contact force network is the spacial heterogeneity. To further quantify the contact forces, a common practice was to plot the probability density function (PDF). Figure 4.2 was the corresponding probability density function for the contact forces shown in figure 4.1. It is generally agreed that the PDF should have a peak or plateau for forces less than the average and an exponential tail for forces greater than average[66, 74]. Figure 4.2 indicated that my system fit that character rather well especially for the inset, which was a semi-log plot of the same distribution curve with a linear fit for forces that were greater than average.

The contact force network has been extensively studied. Hecke[89] argued that there is a subtle change in the tail of the distribution curve that determined the onset of jamming.

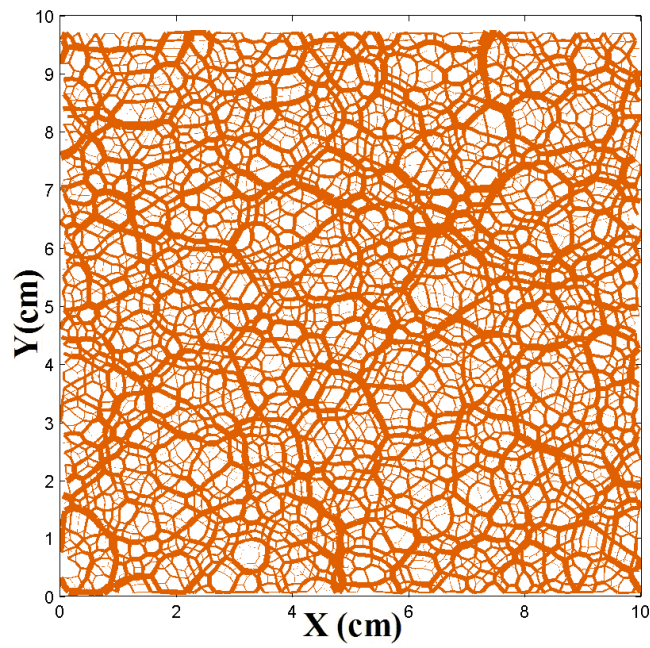
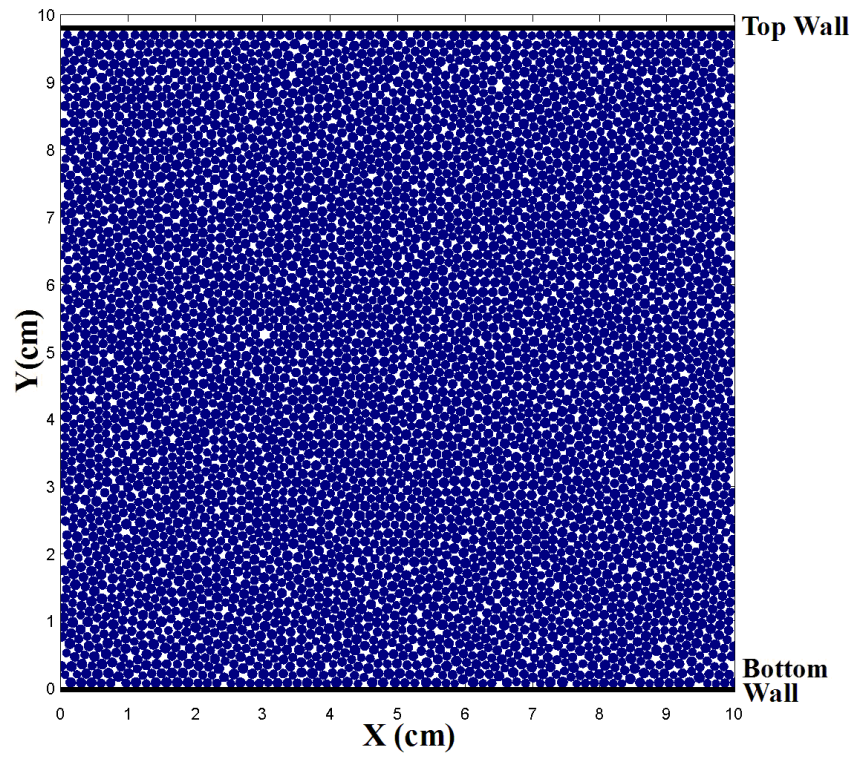
4.3 Dynamic properties of the prepared system

4.3.1 Pulse mode

One of the easiest way to probe a granular system was to send a pulse through it and measure quantities such as the pulse speed, the attenuation rate etc. The pulse I sent through the confined granular system was a one-period cosine wave as illustrated in figure 4.3. The method of generating such a pulse was to move the top wall exactly as the plotted cosine pulse and held it fixed before and after the pulse.

Figure 4.4 was a snapshot of a pulse propagating through the system. The horizontal direction was defined as x-axis and the vertical direction was defined as y-axis. The color code corresponding to the magnitude of the y-component of the particle velocity. Floaters were usually moving at much higher speed comparing to those “jammed” particles. That is why their color was out of the spectrum.

³Only normal forces were plotted and discussed here.



84
Figure 4.1: A snapshot of the system and its contact force network

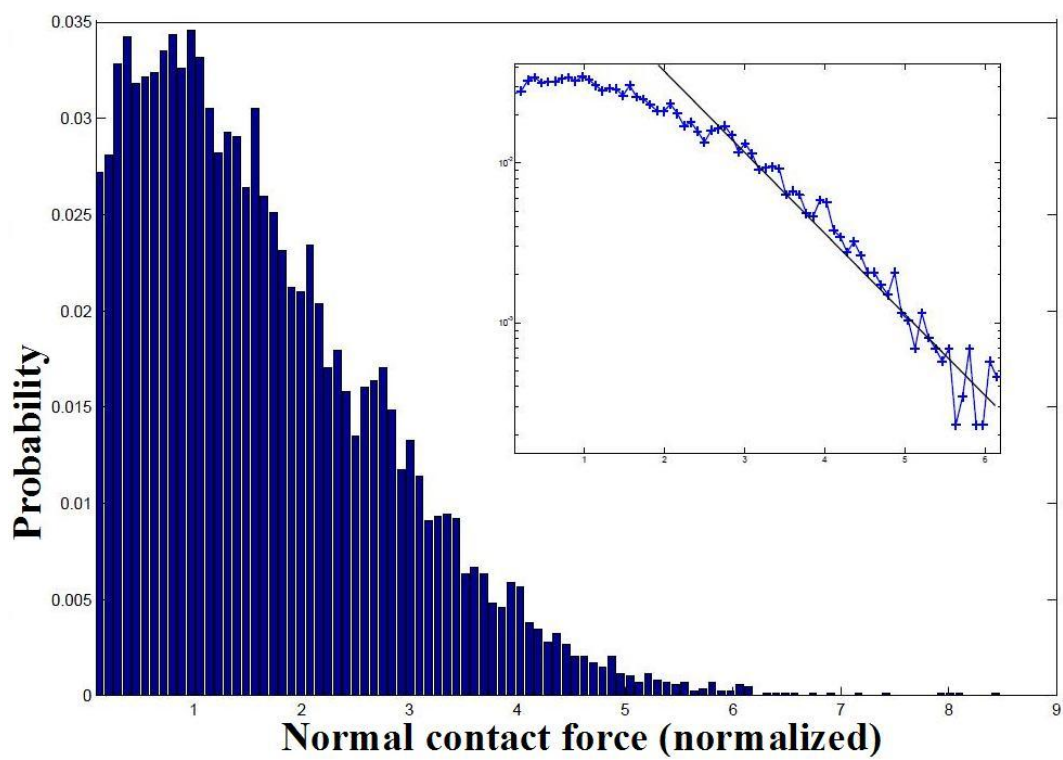


Figure 4.2: Probability distribution curve

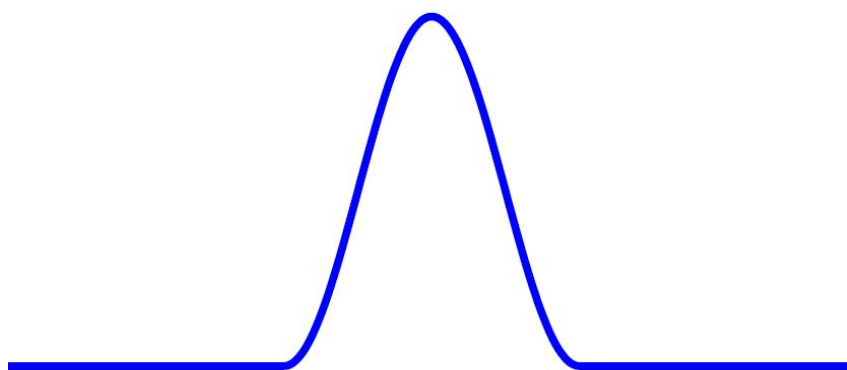


Figure 4.3: Shape of the cosine pulse

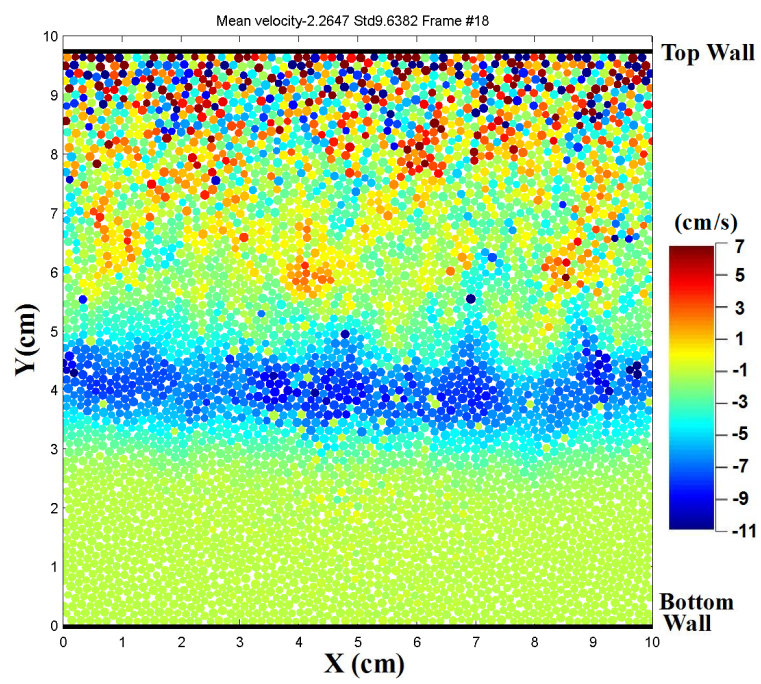


Figure 4.4: A snapshot of a pulse propagating through the system, What point in time?

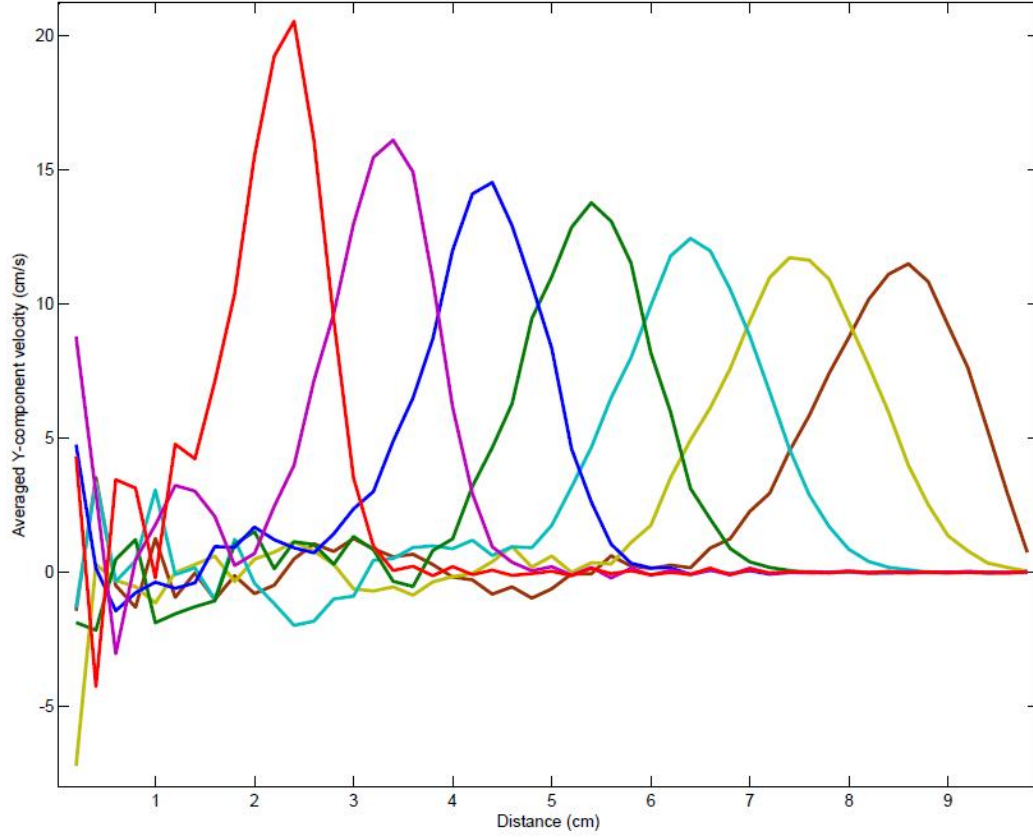


Figure 4.5: Horizontally averaged y-component velocities at equal time interval (colors to indicate different instants of time.)

4.3.1.1 speed of a pulse

To measure the speed of a pulse, it is necessary to define “the arrival of the pulse”. Some common choices were the first raise of 10% of peak magnitude, the peak itself or the first zero after the peak[18]. Depending on the choices, the measured pulse speed could differ by 10% or more.

I used the peak as “the arrival of the pulse” and estimated the speed of the pulse in figure 4.5 to be 1.0×10^5 cm/s. Because the peak moved about 5 cm between the first peak and the second last peak and the time spacing between them was 5.0×10^{-5} second (1.0×10^{-5} second

interval). This speed was then used to make an estimation of the base resonant frequency (the first harmonic) utilizing the following formula

$$f = \frac{v}{2L} \quad (4.2)$$

where v is the speed of the pulse and L is the length of the system.

So, this would predict a resonance peak at $1.0e5/(2 * 10) = 5$ kHz, which is a bit lower than it actually is (~ 4.96 kHz).

The behavior of pulses propagating in a granular system have been extensively studied[92, 25, 18]. It was generally accepted that the speed of a pulse in a granular media is proportional to the power of confining pressure:

$$v \propto p^\alpha \quad (4.3)$$

and the power coefficient α is somewhere between $\frac{1}{4}$ and $\frac{1}{6}$.

4.3.1.2 attenuation and total absorbing layer

A puzzling experimental finding in geophysics community is that the attenuation rate is linearly proportional to frequency over a wide range (as much as 9 decades)[58, 83, 49, 10, 62]. Commonly used dissipation models are unable to explain it. In the quest for a satisfactory dissipative model, Marder finds two possible candidates. One is a hysteresis model and the other is a model of array of energy sinks. He believes that both models work in some degree depending on the physical situation to be modeled. And, he also proposes a method to distinguish one model from another.

A simple discrete one-dimensional version of a hysteresis model can be described by the following equation[53]:

$$\ddot{u}_i = F(E_i, \dot{E}_i) - F(E_{i-1}, \dot{E}_{i-1}) \quad (4.4)$$

Here

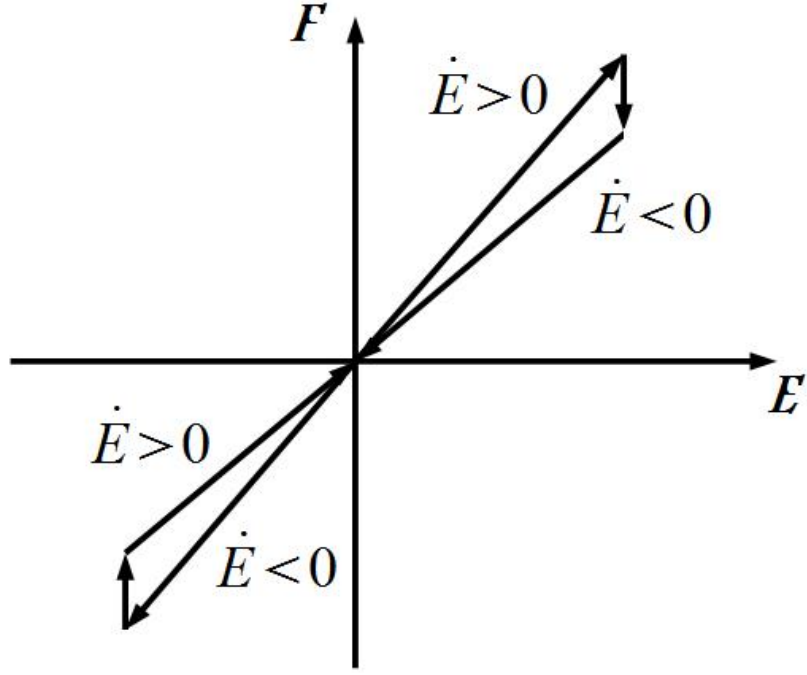


Figure 4.6: Hysteresis loop

Figure 4.7: sine wave transforms to triangular wave

$$E_i = u_{i+1} - u_i \quad (4.5)$$

is the extension of the bond between particle i and $i + 1$, and $F(E_i, \dot{E}_i)$ is the force between them.

To create hysteresis, the forces between neighboring particles assume the following form

$$F(E, \dot{E}) = E + b|E|\frac{\dot{E}}{|\dot{E}|} \quad (4.6)$$

A hysteresis loop of this form of forces is shown in figure 4.6.

A numerical solution of this model (figure) shows a propagating sine wave transforms to triangular wave within 20 wavelengths.

Another competing model is the arrays of energy sinks model[13]. It describes the interaction between any two mass points by a large number of over-damped dissipative modes. The solution of this model shows no sign of change of waveforms.

So in order to find out which one of them gives a better description of the energy dissipation mechanism in the granular packing that I constructed numerically, all I need to do is to send a sine wave through the packing and look for changes in the waveform (if any).

Preliminary results indicate that the wave doesn't change its shape even after hundreds of periods, which is clearly in favor of the array of energy sinks model.

One prerequisite of this study is to construct a total absorbing layer in order to mimic an infinite medium that an outgoing wave never reflects back. Walker and Wax[90] showed in 1940s that an exponential impedance could provided a total damping to transverse acoustic waves in isotropic non-homogeneous medium. Khilla[48] showed in 1980s that an exponential impedance could provided a total damping in a transmission line. But, a total absorbing layer has never been attempted in a granular simulation.

The current release of LAMMPS is unable to assign a spatially varying damping coefficient, but it is not that hard to insert a few blocks of code to make that happen. The modified LAMMPS evaluates a viscous force based on where the contact locates and by setting an exponentially increasing viscous coefficient in certain region one gets a total absorbing layer.

Figure 4.8 and figure 4.9 demonstrates how well the total absorbing layer works. The absorbing layer is between 0 to 50 mm with exponentially increase viscous coefficient from 50 mm downwards. A pulse is propagating from the top to the bottom (from above 100 mm to 0 mm). In the system with a total absorbing layer, there is almost no reflected wave. While in the system without a total absorbing layer, a reflected wave exists. (Dashed line indicates reflected wave.)

4.3.2 Resonance mode

Paul A. Johnson and his coworkers argued that there was a new class of materials called Nonlinear Mesoscopic Elastic (NME) , whose behavior could not be fully appreciated by classical nonlinear theory (Landau nonlinearity)[31]. The range of this new class was fairly wide, including sand, rocks, soils, cement, concrete, artificial granular packings, and dam-

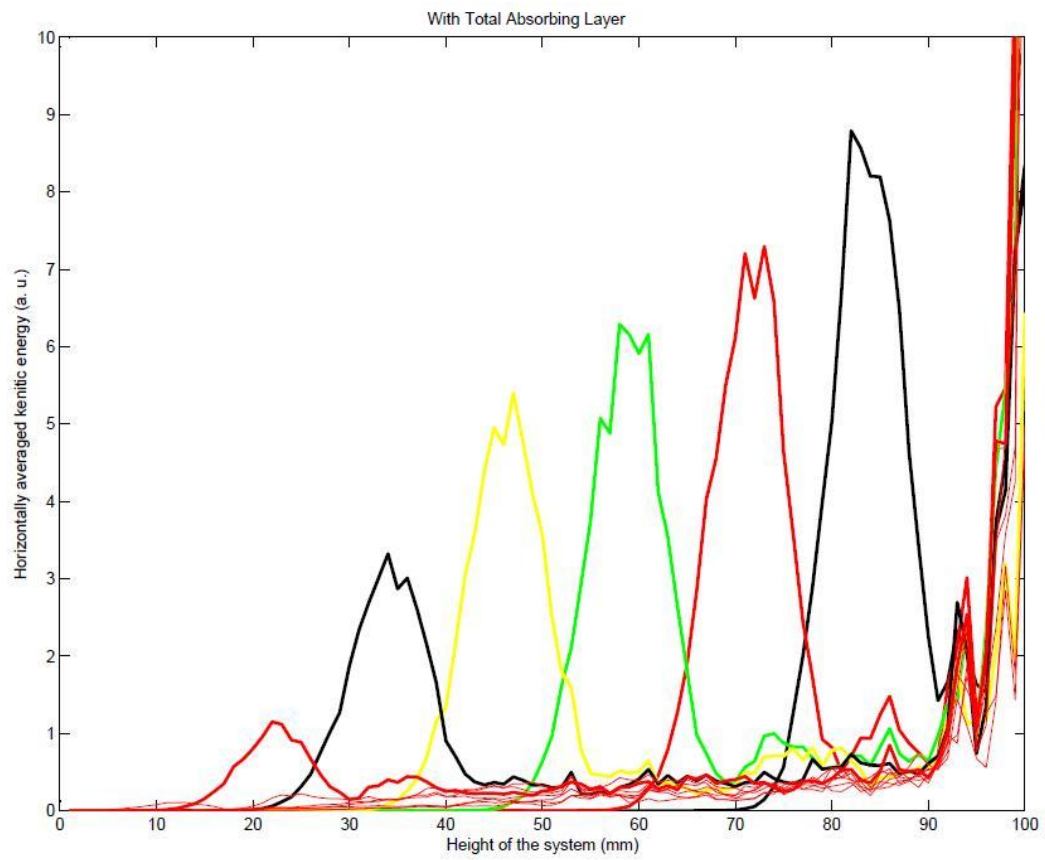


Figure 4.8: With total absorbing layer (colors to indicate different instants of time.)

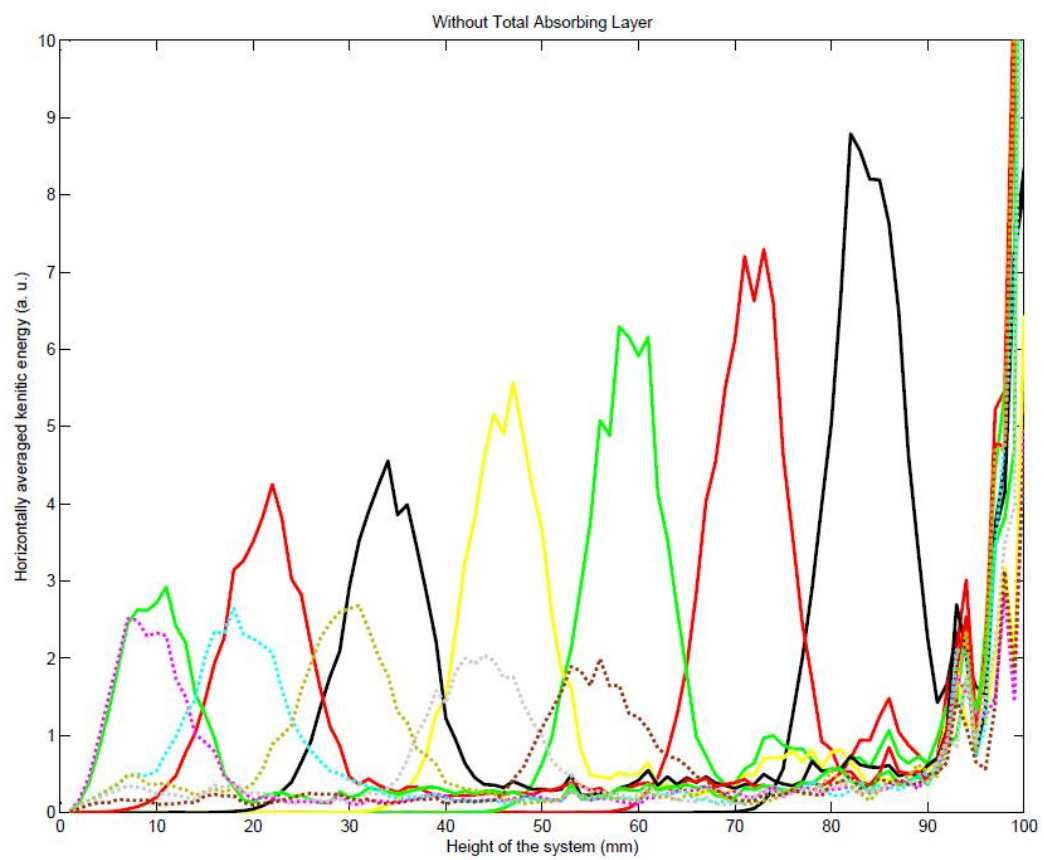


Figure 4.9: Without total absorbing layer (colors to indicate different instants of time.)

aged materials. The unique characteristics of them included hysteresis, end-point memory, harmonic generation and resonant frequency shift etc.

Resonant frequency shift was a well known phenomena in the geophysics community, which is the downward shift of resonant peak as driving amplitudes increase also known as dynamic softening. But, it was not very clear what was the underlying mechanism. Experimental investigation was difficult due to the fact that it was a differential effect. In the case of 2-D photo-elastic disks, the contact force network might be relatively easy to figure out compared to finding out how some tiny extra load was re-distributed. Besides, it is dynamical and only significant in statistical measure.

MD simulation of a confined granular system provided a powerful alternative and much more detailed information regarding the microscopic dynamics, whose collective effect made the resonance curve shift on the macroscopic scale.

Using the estimated resonance frequency from time-of-flight measurement as a reference point and driving the top wall with a single harmonic motion at frequencies close to the resonance, I was able to find a steady state for the confined granular system at frequencies around the first harmonic .

To drive the system at a particular frequency f , I set the motion of the top wall to follow exactly as

$$y = y_0 + A \sin(2\pi ft) \quad (4.7)$$

where y_0 is the equilibrium position of the top wall maintaining a confining pressure, A is the dynamic amplitude, amplitude of 1 corresponds to a dynamics strain of $5.0\text{e-}8$.

To ensure that the system was driven at the first resonant peak, I plotted the horizontal average of the y-component of particle velocities at different instants. Figure 4.10 shows one of such plots. The fit is a sine wave (half period). This demonstrates clearly that the system is indeed oscillating at its first harmonic.

The response amplitude was measured by fitting the force on the bottom wall with a single frequency sine curve. It is possible to have higher harmonics to be generated, but their magnitude was ignored for the current study. Figure 4.11 was a typical least square curve fit to the force on the bottom wall. The fit was a search for the best amplitude to

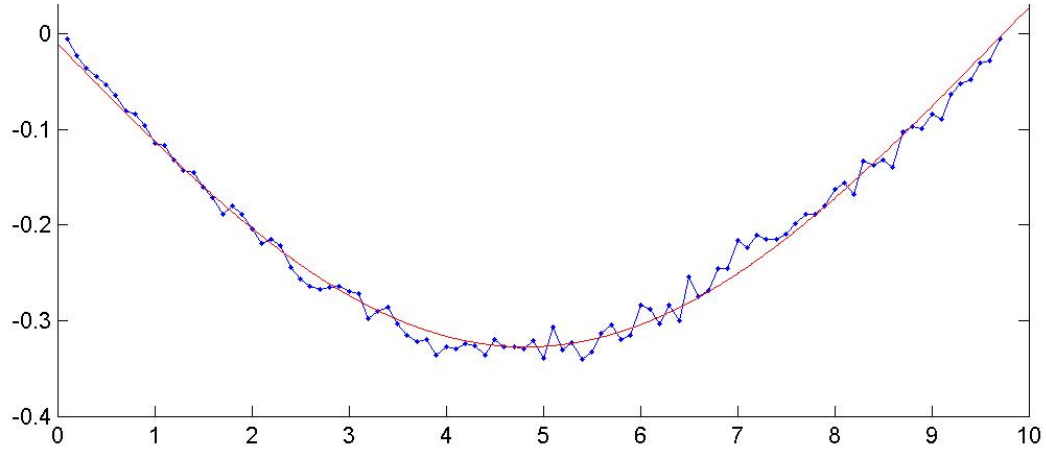


Figure 4.10: Horizontal average of y-velocity at resonant condition

minimize the sum of the squared distances between the data points and the curve.

I studied three different confining pressures, which were estimated to correspond to 300 kPa, 3.1 MPa and 11.9 MPa respectively in 3-D by assuming the disks to have unit thickness even though they had different diameters. For each confining pressure, five resonance curves were measured with driving amplitude to be 1, 3, 10, 30 and 100 respectively.

To find the position of resonant peak, I fitted each individual resonance curve with the equation 4.8, which was the frequency response function of amplitude for a forced damped oscillator.⁴

$$A(f) = \sqrt{\frac{A(f_0)}{1 + [2Q(f - f_0)/f_0]^2}} \quad (4.8)$$

To summarize those resonance curves, I plotted the resonant peaks (normalized to the resonant frequency of amplitude of 1) as a function of driving amplitude as shown in figure 4.15. The blue, red and green curves were the normalized⁵ peak positions as a function of driving amplitudes for confining pressures of 300 kPa, 3.1 MPa and 11.9 MPa respectively.

To understand the mechanism of resonant frequency shift, I studied the contact force network of different driving amplitudes for the packing under 300 kPa confining pressure

⁴The resonance curves deviated slightly from the resonance curves of a classical damped oscillator, but the fits were good enough for estimating the peak positions.

⁵Divide the peak positions of higher amplitudes by the peak position of the smallest amplitude $A = 1$ for each confining pressures.

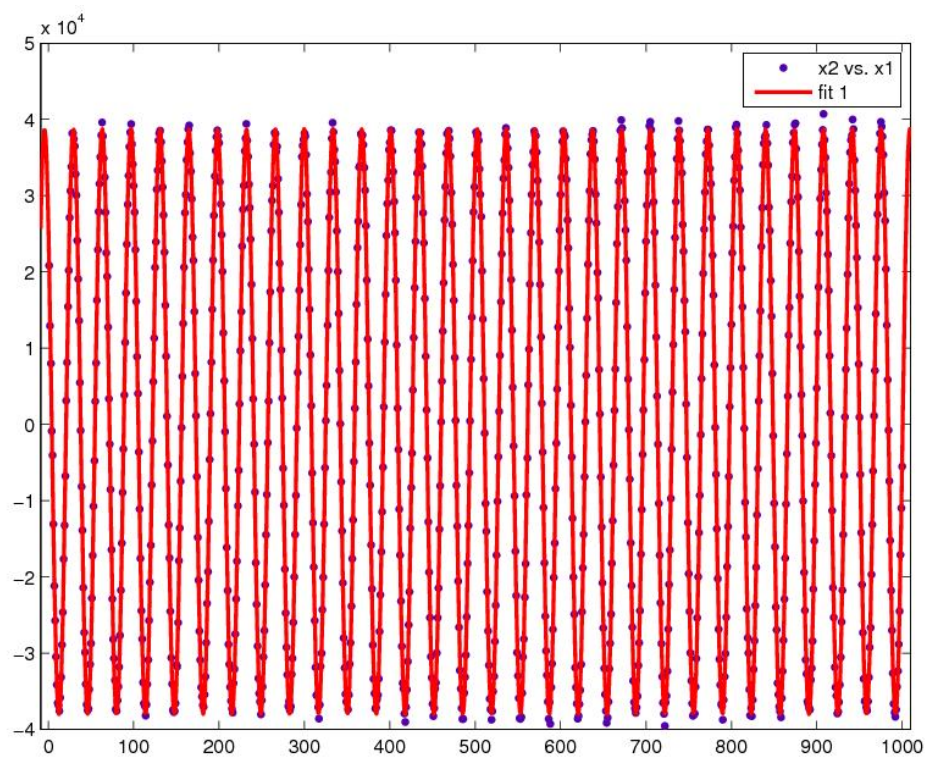


Figure 4.11: Fit the force on the bottom wall

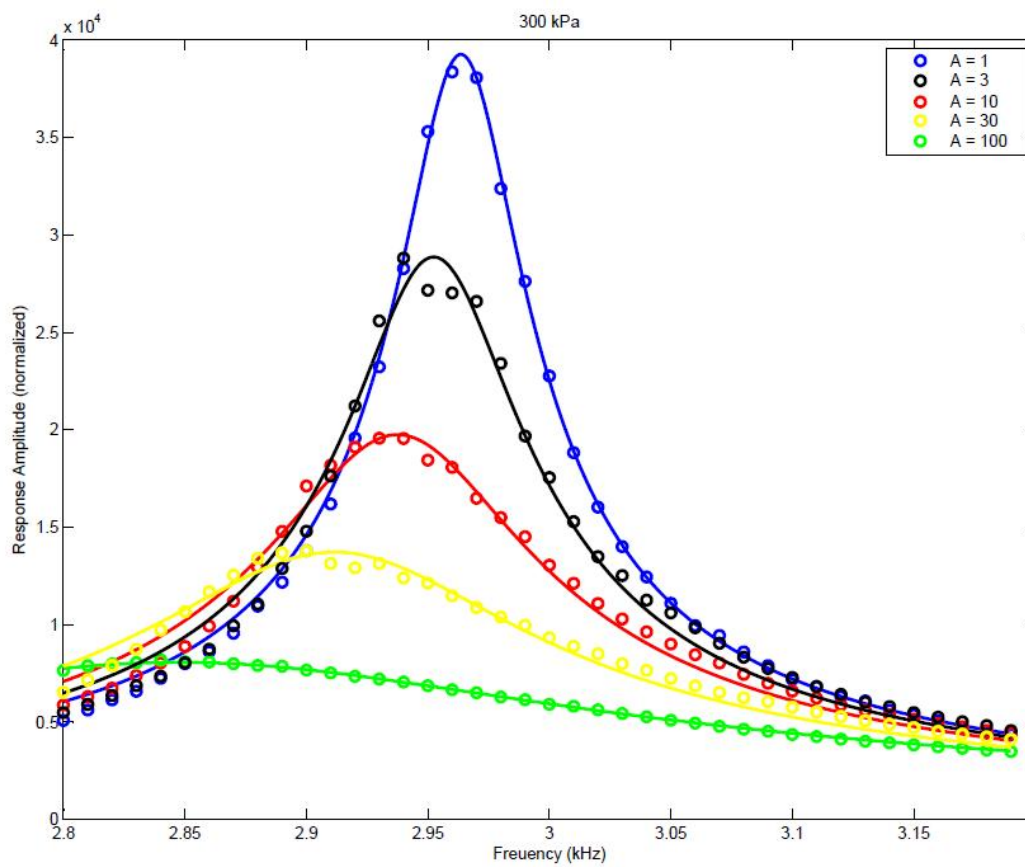


Figure 4.12: resonance curves at 300 kPa

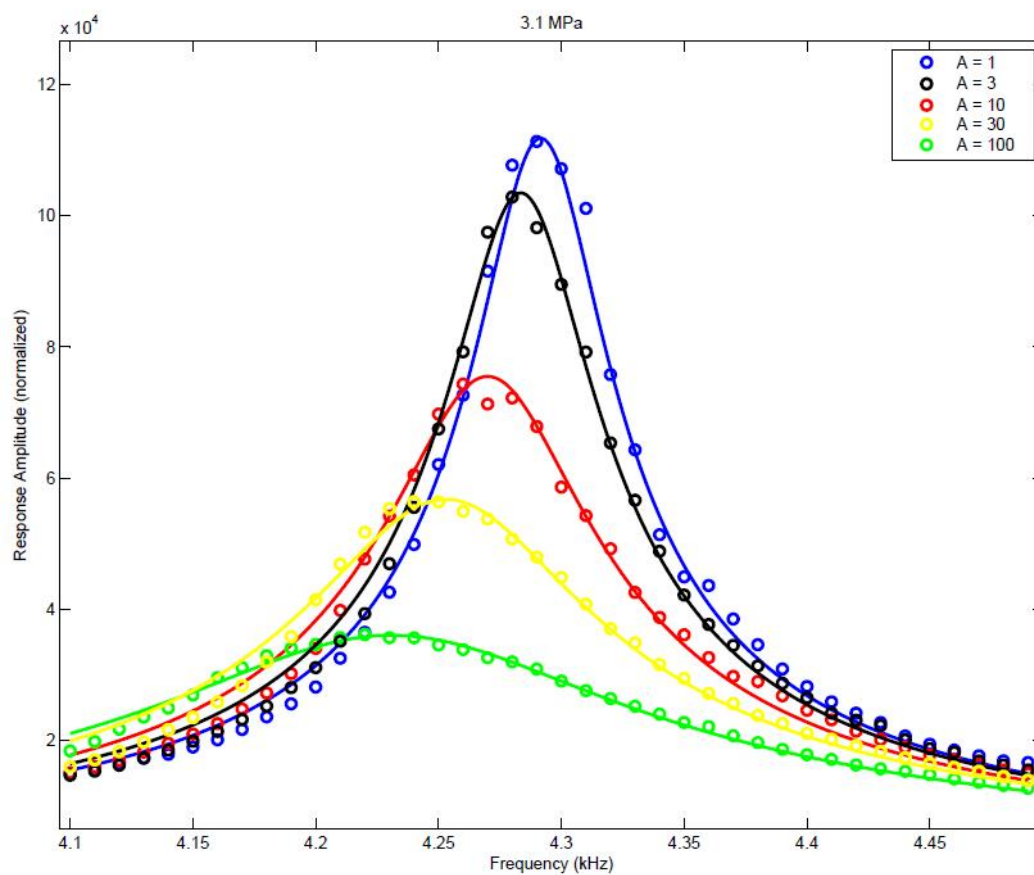


Figure 4.13: resonance curves at 3.1 MPa

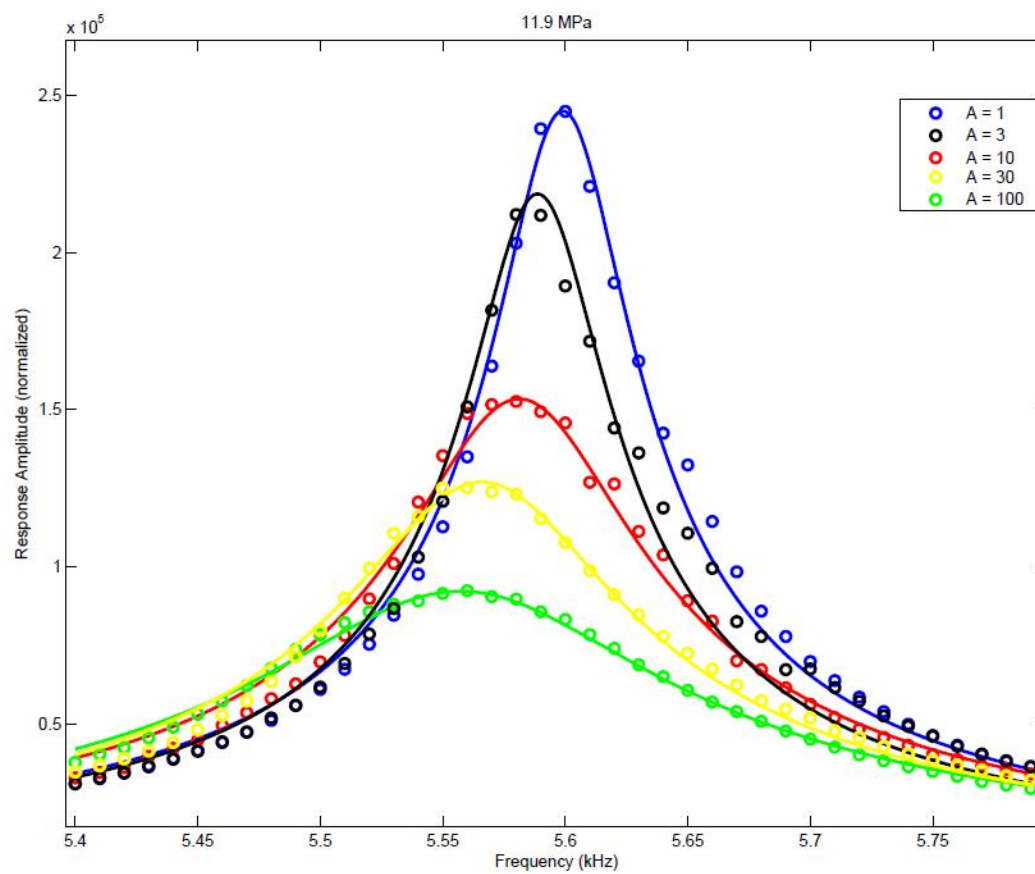


Figure 4.14: resonance curve at 11.9 MPa

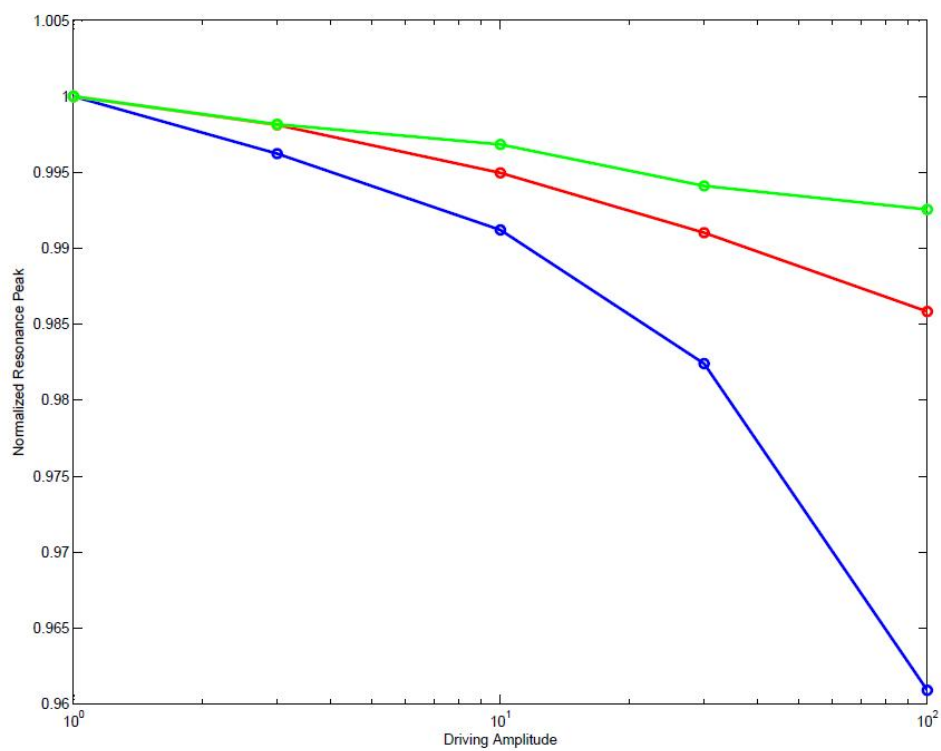


Figure 4.15: Frequency shift as a function of amplitudes

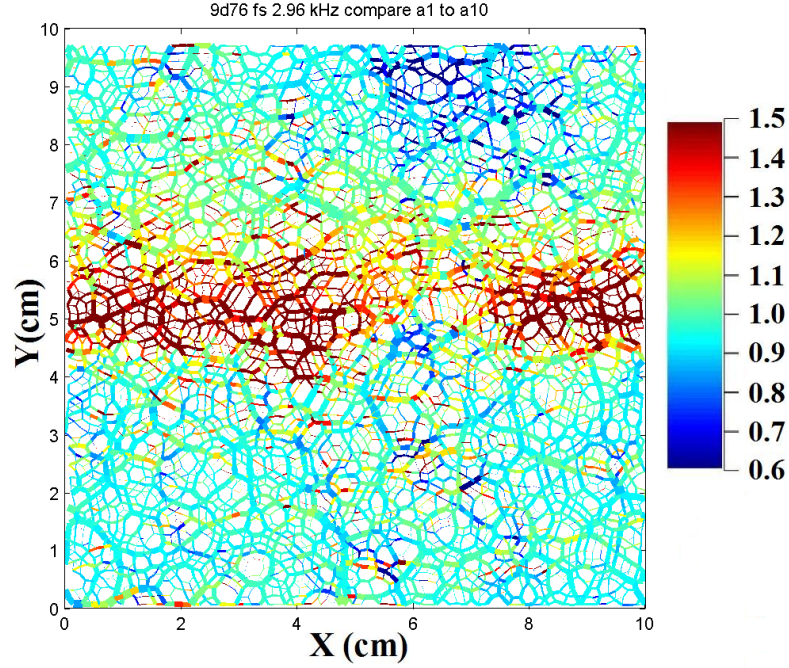


Figure 4.16: Relative increase of oscillation intensity of the whole contact force network

driven at 2.96 kHz (resonant frequency for amplitude 1). One can think of the contact force network as a stable structure of channels and a small displacement of the top wall creates a burst of perturbations, which act like a fluid flowing through those channels. For resonance condition, continuous disturbance from the top wall is just like a continuous source of flow. An interesting discovery is that statistically the wider the channel, the slower the flow. That is, the stronger the contact, the less oscillation of the force. Figure 4.16 indicates the ratios of dynamic intensities on every contact forces between amplitude $A = 10$ and $A = 1$. For each contact force, the width of the line is proportional to the magnitude of the force and the color code indicates the ratio of dynamic intensity (oscillation amplitudes squared and averaged over more than 20 periods).

First noticeable feature of figure 4.16 is that the relative increase of oscillation intensity is spatially non-homogeneous. Roughly speaking, the middle portion of the packing increases above average and the portions close to top and bottom walls increase below average.

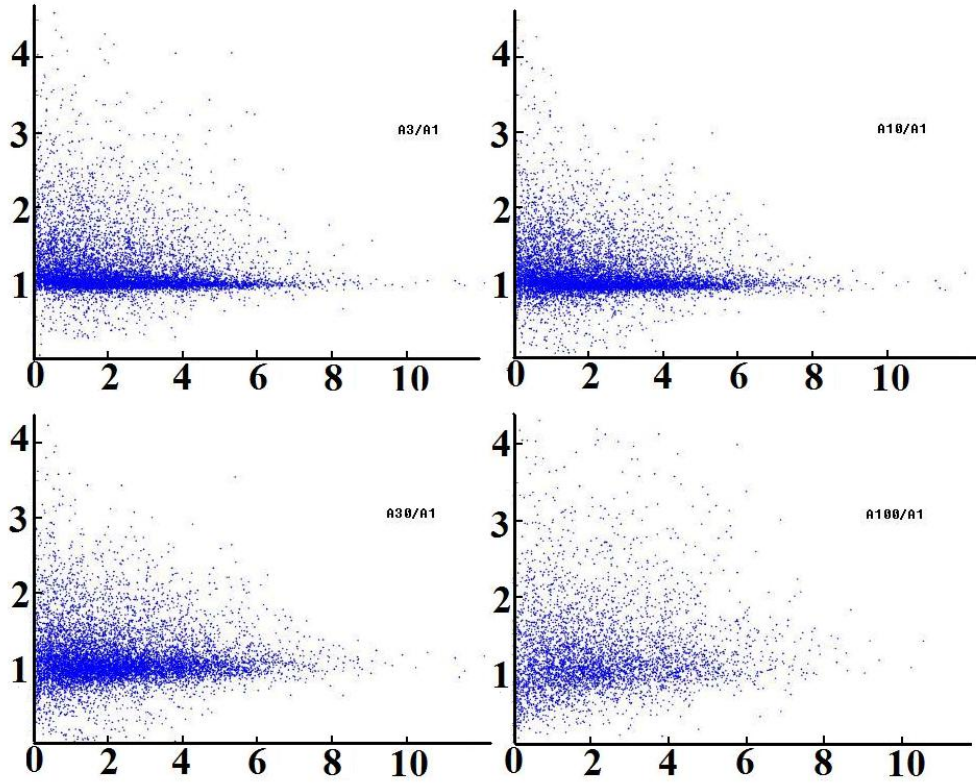


Figure 4.17: Oscillation intensity comparison of driving amplitude 3, 10, 30, 100 to 1

To study this feature more quantitatively, the ratios of the oscillation intensities between amplitude $A = 3$ and $A = 1$ are plotted as a function of the magnitudes of the contact forces, which is then repeated for all larger driving amplitudes ($A = 10$, $A = 30$ and $A = 100$). Figure 4.17 shows the distribution of the relative oscillation intensities⁶ as driving amplitudes increase.⁷

A clear trend of the relative increase of oscillation intensity is that the greater the driving amplitude the wider the scattering of the relative increase. This finding can provide an explanation for the resonant frequency shift if one can somehow relate the magnitude of the contact forces to the resonant mode of the system.

⁶Divided by the dynamic intensity on that contact force when amplitude $A = 1$.

⁷Each individual plot is given in appendix 6.3.

4.4 summary and brief report of ongoing studies

More data and analysis are needed to check if there is any change of waveform in order to determine which model provides a better energy dissipation mechanism for LAMMPS.

More analysis and theoretical work are needed to provide complete explanation for resonant frequency shift.

Chapter 5

Conclusions

In this thesis I studied three separate but closely related subjects.

In the low temperature fracture experiment, tremendous effort was spent to search for the velocity gap, a range of speed that no steady crack propagation is possible when the thermal energy was low enough (< 100 Kelvin). This is a feature solely due to the discrete nature of the fracture process. The data I gathered provided a good indication that the velocity gap does exist.

In the friction experiment, the data clearly overturned some commonly held understanding of static friction, which eventually led us to propose a modified rate- and state-equation and unified the mathematical description of friction as well as the physical understanding to it.

In the granular simulation, two different modes (pulse mode and resonance mode) of probing a confined granular system were conducted with a parametric study of the influence of the confining pressure as well as the driving amplitude. The pulse mode provided information on attenuation, which was used to distinguish between two widely accepted energy dissipation models. Due to the lack of change in the waveform of a single propagating sine wave, LAMMPS clearly favor the array of energy sinks model over the hysteretic model as the major energy dissipation mechanism in a confined granular medium. And, the resonance mode provided an intuitive explanation for the resonant frequency shift in terms of how dynamic loads were re-distributed through the contact force network.

Chapter 6

Appendix

6.1 Wafer preparation for the fracture experiment

Here is the procedure to prepare a wafer before it can be used in the fracture experiment.

A set of raw wafer (usually 5 pieces) is firstly baked in an oven under 1000 degree C for 16~18 hours. This is to grow an insulating layer of silicon dioxide. The purpose of that is to electrically isolate the wafer from its environment when it is held to the metal frame lately.

The next step is to put electrical leads on the wafer, which is bridged by a layer of aluminum. In order to properly position and shape the leads, a set of aluminum masks is designed. The baked wafers are approximately align with the mark on the mask and fixed to position by a small piece of adhesive tape. Then, the wafers and masks are carefully stacked together and bundled by two paper clippers. The stack should be so arranged that all the parts of wafers that need to be deposited by aluminum are facing the same side and as close to each other as possible. Then, the stack together with a vaporization bowl and a piece of crystal are delivered to the MBE (Molecular Beam Epitaxy) chamber on the 3rd floor to get a layer of 4000 Å aluminum deposition.

After the aluminum deposition, a second bake under 550 degree C for 3 hours is required to drive the aluminum atoms through the silicon dioxide layer and make a good ohmic contact to the single crystal silicon underneath it.

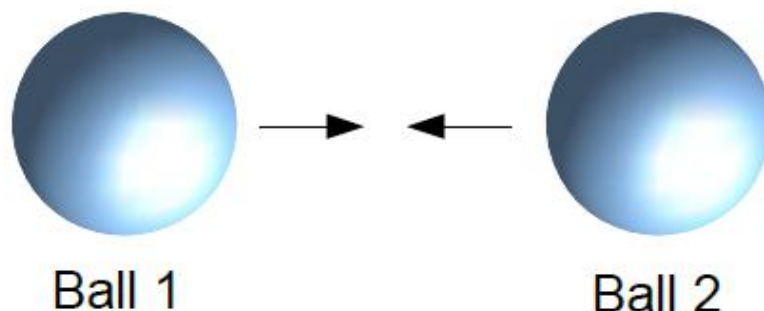


Figure 6.1: Two identical balls collide

Afterward, a set of wires and tabs (small pieces of copper sheet 2~3 mm X 2~3 mm) are prepared. The tabs are made from a piece of thin copper sheet, cut into small rectangular with desired dimensions and flattened by milling them between flat surfaces of two big pieces of bulk iron (one at a time to ensure the flatness of the tab). Then, wires are soldered to the tabs.

The last step is to wire the wafer, that is to connect the tabs to the leads. The agent that stick the tabs to the aluminum leads is some special purpose silver glue. The silver glue should be kept refrigerated till the moment it is used. A tiny amount of silver glue should be applied to the flat side of the copper tab and then small wire campers are used to hold the tabs firmly on the wafer. After all four tabs are carefully glued onto the leads of the wafer and firmly held by the campers, the wafer is briefly bake again under 175 degree C for about 4~5 minutes. The baking quickly solidified the silver glue, which makes the connection permanent (the campers can then be detached).

6.2 Bug report to LAMMPS admins

Dear LAMMPS admins,

I'm trying to illustrate here a bug within the granular package of LAMMPS.

I performed collisions between two identical balls, as indicated in figure 6.1.

In all the simulation, there is no gravity. Equal but opposite velocities are given to the balls as initial condition.

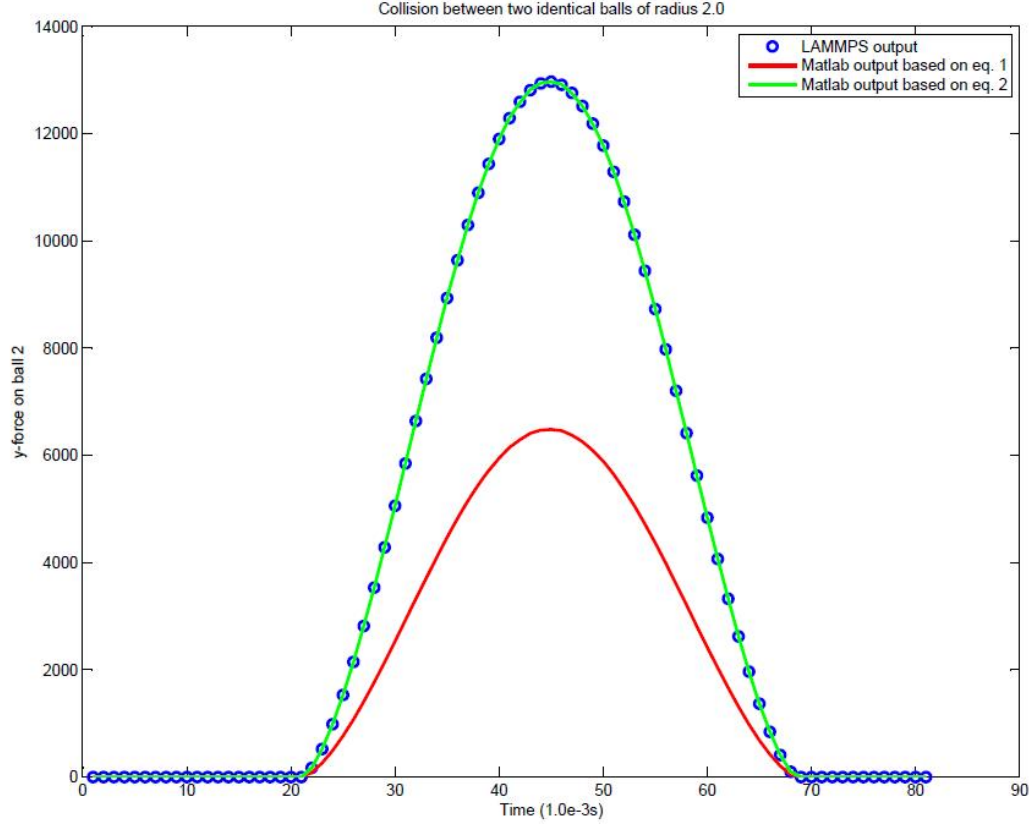


Figure 6.2: y-force on ball 2 with radius 2

The normal force on ball 2 is calculated in LAMMPS and compared to independent calculations by Matlab. For the first two simulations, γ_n is set to zero, that is, visco-elastic damping is turned off for the purpose of pinning down the problem.

The force calculation by Matlab is based on equation 6.1, which can be found on page 426, LAMMPS user manual:

$$F = \sqrt{\frac{d-r}{d}} (K_n(d-r) - \gamma_n m_{eff} V_n) \quad (6.1)$$

$d = R_1 + R_2$ is the contact distance between two balls of radius R_1 and R_2

r is the distance between the centers of contacting balls

K_n is the elastic constant for normal contact

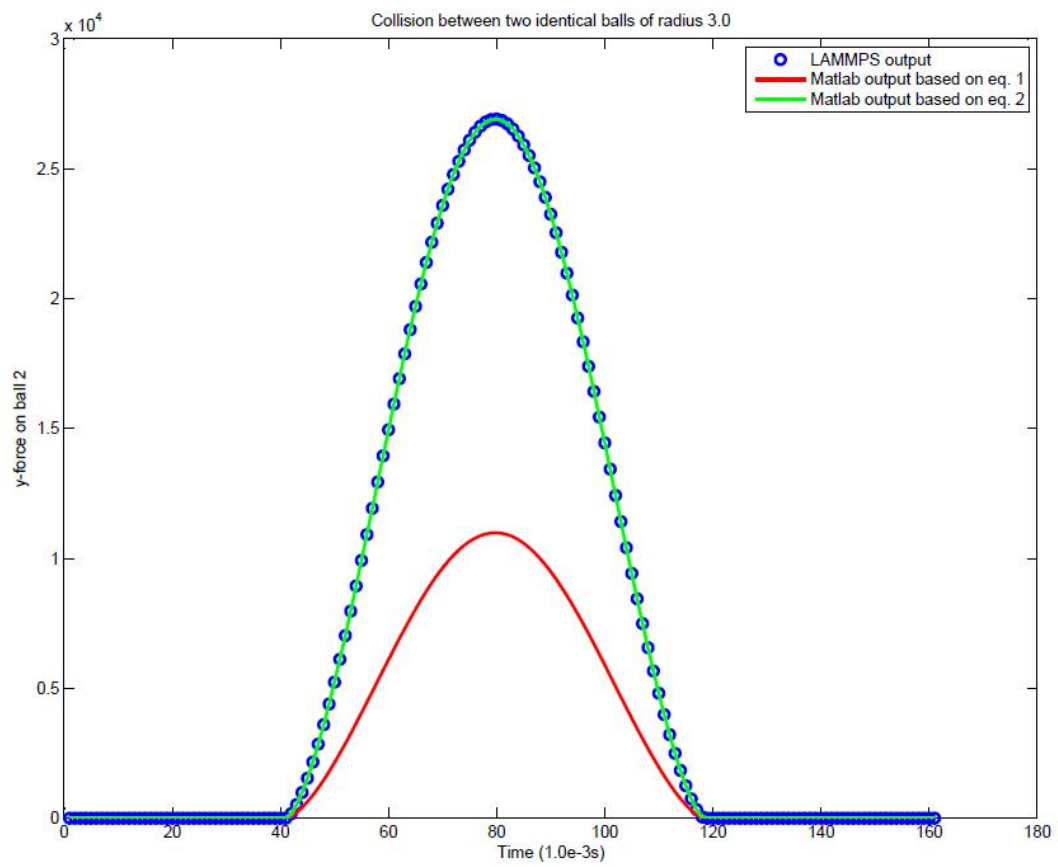


Figure 6.3: y-force on ball 2 with radius 3

γ_n is the viscoelastic constants for normal contact

$m_{eff} = m_i m_j / (m_i + m_j)$ is the effective mass of two balls of mass m_i and m_j

V_n is the normal component of the relative velocity of the two balls

To my surprise, the force calculated this way (the red curve) does NOT match the force calculated by LAMMPS (the blue circles). However, the forces calculated by LAMMPS can be matched by calculation based on equation 6.2(the green curve).

$$F = \sqrt{d-r}(K_n(d-r) - \gamma_n m_{eff} V_n) \quad (6.2)$$

It is believed that equation 6.1 is correct. It is listed in LAMMPS user manual, and it is also seen in literature, for example, the experimental paper by Laurent Labous[54], etc.

This finding is further confirmed by looking into the source code (pair_gran_hertzian.cpp, line 145-154):

```
// normal damping term
// this definition of DAMP includes the extra 1/r term
xmeff = rmass[i]*rmass[j] / (rmass[i]+rmass[j]);
if (mask[i] & freeze_group_bit) xmeff = rmass[j];
if (mask[j] & freeze_group_bit) xmeff = rmass[i];
damp = xmeff*gamman_dl*vnnr/rsq;
ccel = xkk*(radsum-r)/r - damp;
rhertz = sqrt(radsum - r);
ccel = rhertz * ccel;
```

To me, it is a bit surprised to find out that LAMMPS implemented normal contact force (for granular particles) by a single parameter K_n instead of Young's modulus E and Poisson's ratio ν . As this will impose an unnecessary restriction of mono-dispersity to the systems that LAMMPS can simulate, because K_n is actually a function of d , ($K_n = Ed$). Even for mono-dispersity, the forces so calculated are off by a factor of \sqrt{d} . So, please look into this matter and fix the bug.

Along this line of investigation, I also find the following paragraph misleading (page 198, LAMMPS user manual):

“IMPORTANT NOTE: Some models in LAMMPS treat particles as extended spheres or ellipsoids, as opposed to point particles. In 2d, the particles will still be spheres or ellipsoids, not circular disks or ellipses, meaning their moment of inertia will be the same as in 3d.”

What I found is that the mass of the balls is calculated differently for 2d and 3d simulations.

$$M = \pi r^2 \rho \text{ for 2d}$$

and

$$M = \frac{4}{3} \pi r^3 \rho \text{ for 3d.}$$

That is, for 2d simulations, mass of the balls IS calculated as circular disks with unit thickness.

To illustrate that, I did another 2 simulations with γ_n equal to 25, such that different ways of mass calculation could affect the force curve.

6.2.1 The input scripts are as following:

The collision.src file (used as ./lmp_serial < collision.src)

```
# collision test

dimension 3

atom_style granular

boundary p f p

newton off

read_data collision.in

# gamma_n set to zero, no visco-elastic damping

pair_style gran/hertzian 200000.0 0.0 0.5 0

timestep 0.000001

fix 1 all nve/sphere
```

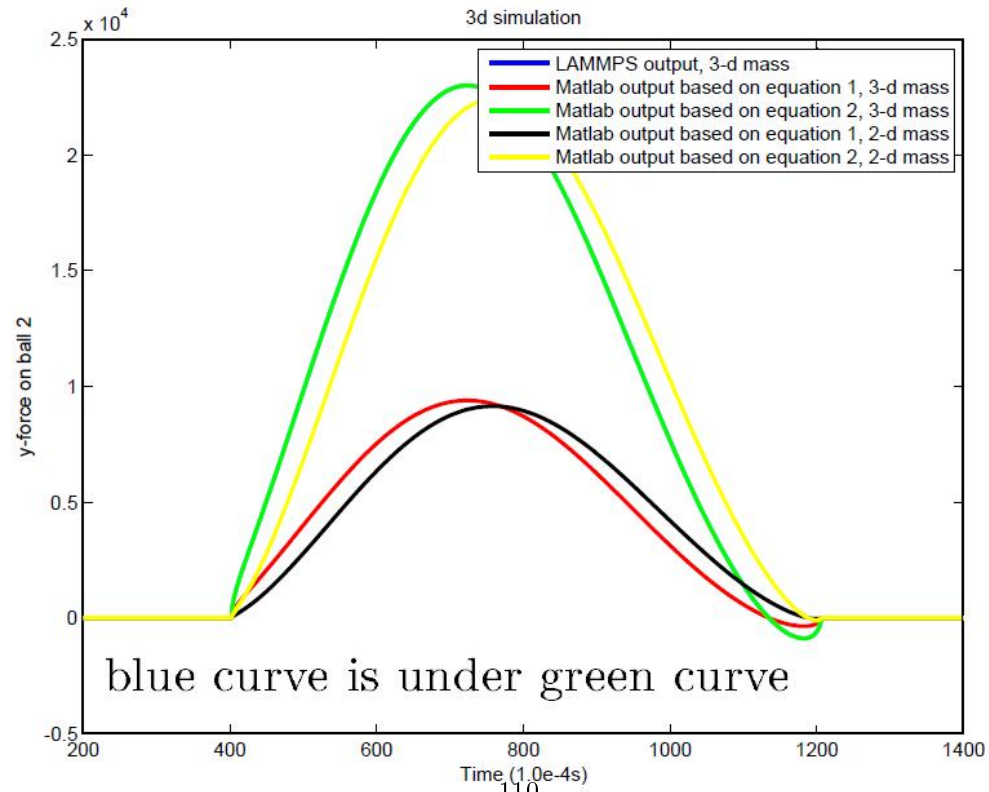
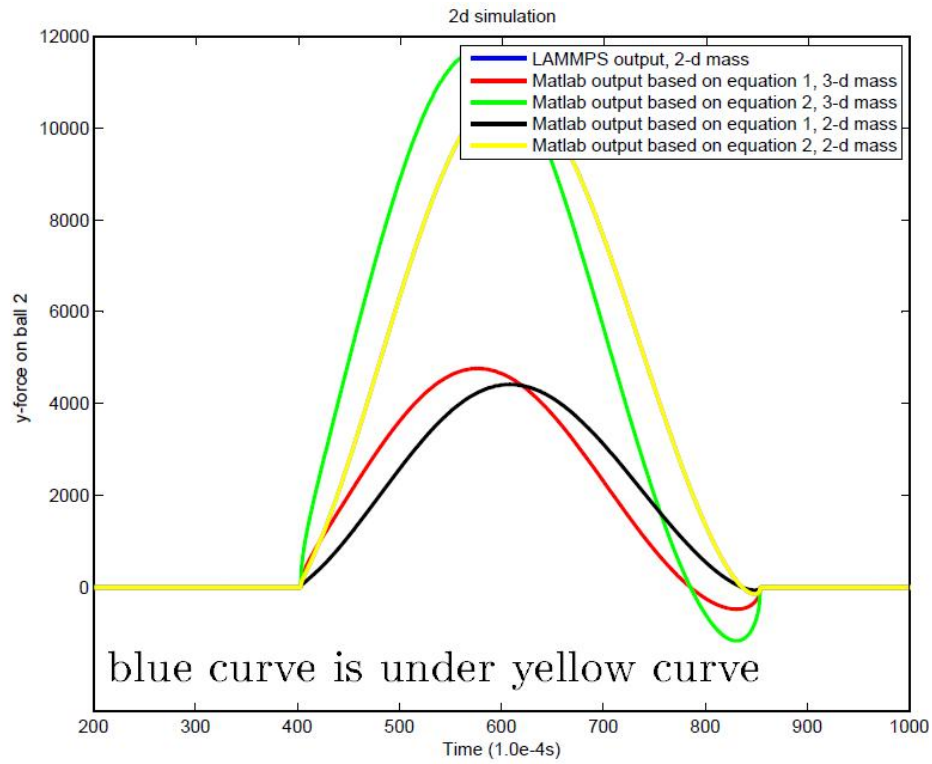


Figure 6.4: collision simulated in LAMMPS (2-d and 3-d)

```

fix ywalls all wall/gran yplane 0 100 50 0

dump 1 all custom 100 collision_gamma.out tag x y vx vy radius fx fy

run 1000000

```

The collision.in file

```

# first line will always be ignored.

# collision test of granular package of LAMMPS

# header section

2 atoms

1 atom types

0 40 xlo xhi

0 40 ylo yhi

-10 10 zlo zhi

# body section

Atoms

1 1 6.0 1.0 14.0 9.0 0.0

2 1 6.0 1.0 14.0 21.0 0.0

Velocities

1 0.0 5.0 0.0 0.0 0.0 0.0

2 0.0 -5.0 0.0 0.0 0.0 0.0

```

Matlab script

```

%collision between two identical balls

%parameters as in LAMMPS

kn = 200000.0;

dens=1.0;

gamma_n=0.0;

```



```

d=6.0; % twice the radius, R1+R2

r=ball2_y-ball1_y; % balls are lined up in x-direction

vn=ball2_vy-ball1_vy; % relative velocity

meff=0.5*(4.0/3.0*pi*(d/2.0)^3)*dens; %effective mass

fy=sqrt((d-r)/d).*(kn*(d-r)-meff*gamma_n*vn); % equation for calculate nor-
mal force as in page 426, LAMMPS manual

fy_m = sqrt(d)*fy;

plot(ball2_fy(5600:7200),'b')

hold on

plot(real(fy(5600:7200)), 'r')

plot(real(fy_m(5600:7200)), 'g')

xlabel('Time (1.0e-4s)')

ylabel('y-force on ball 2')

```

6.3 Graphs of Relative Increase of Oscillation Intensity

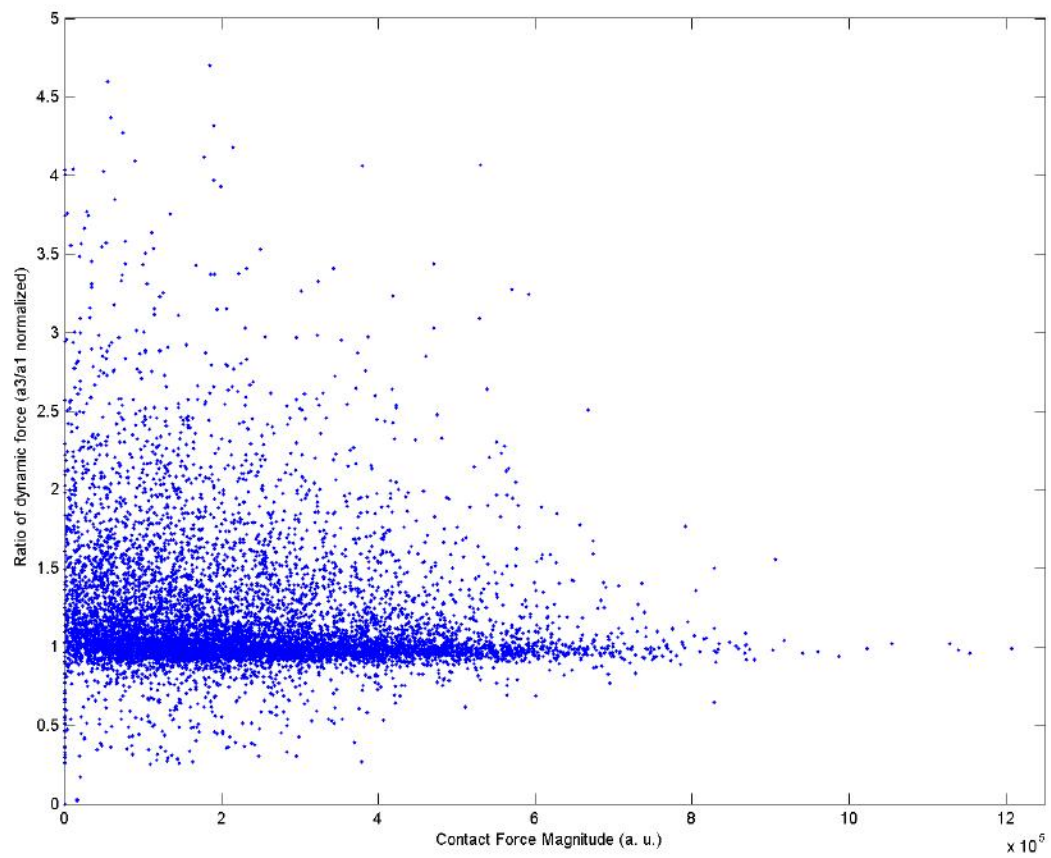


Figure 6.5: A_3/A_1

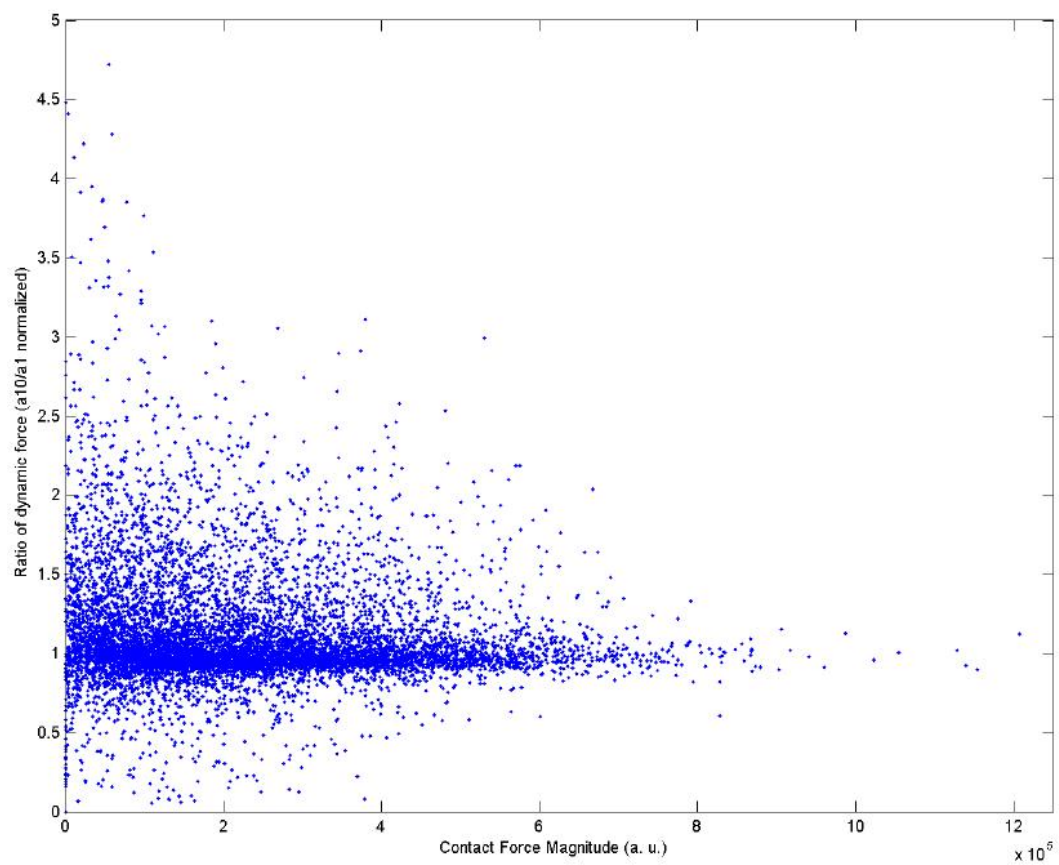


Figure 6.6: A_{10}/A_1

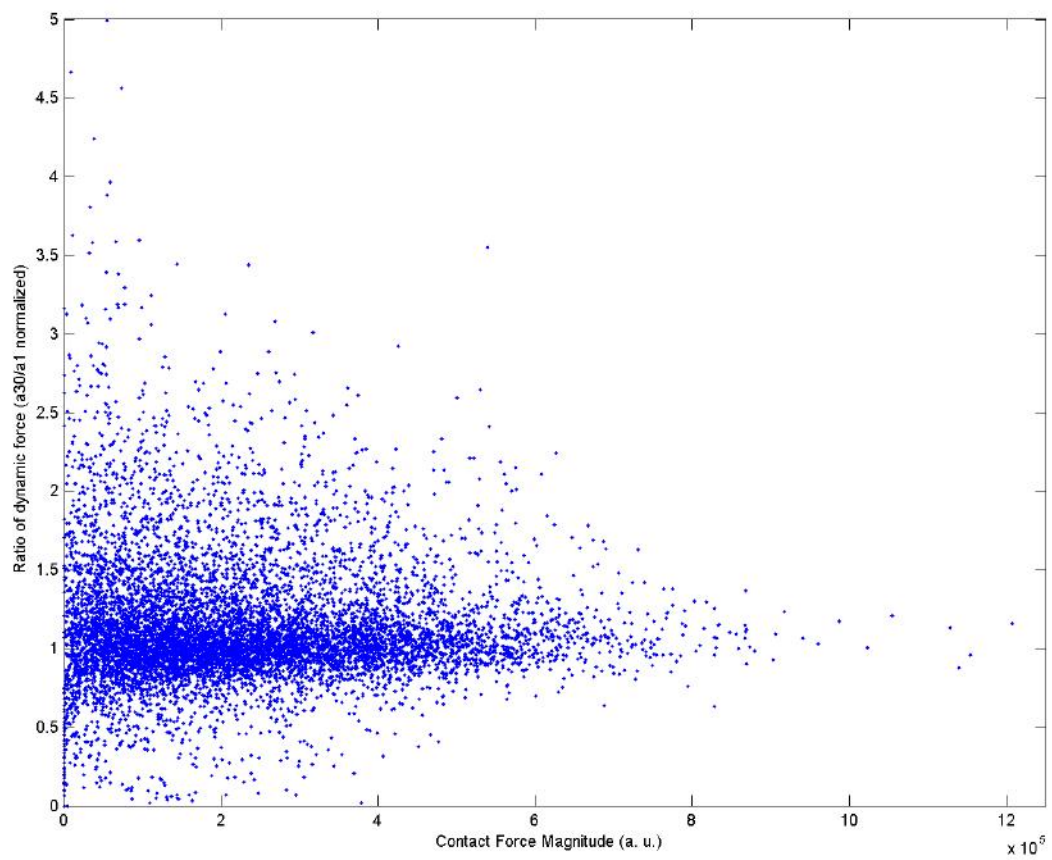


Figure 6.7: A_{30}/A_1

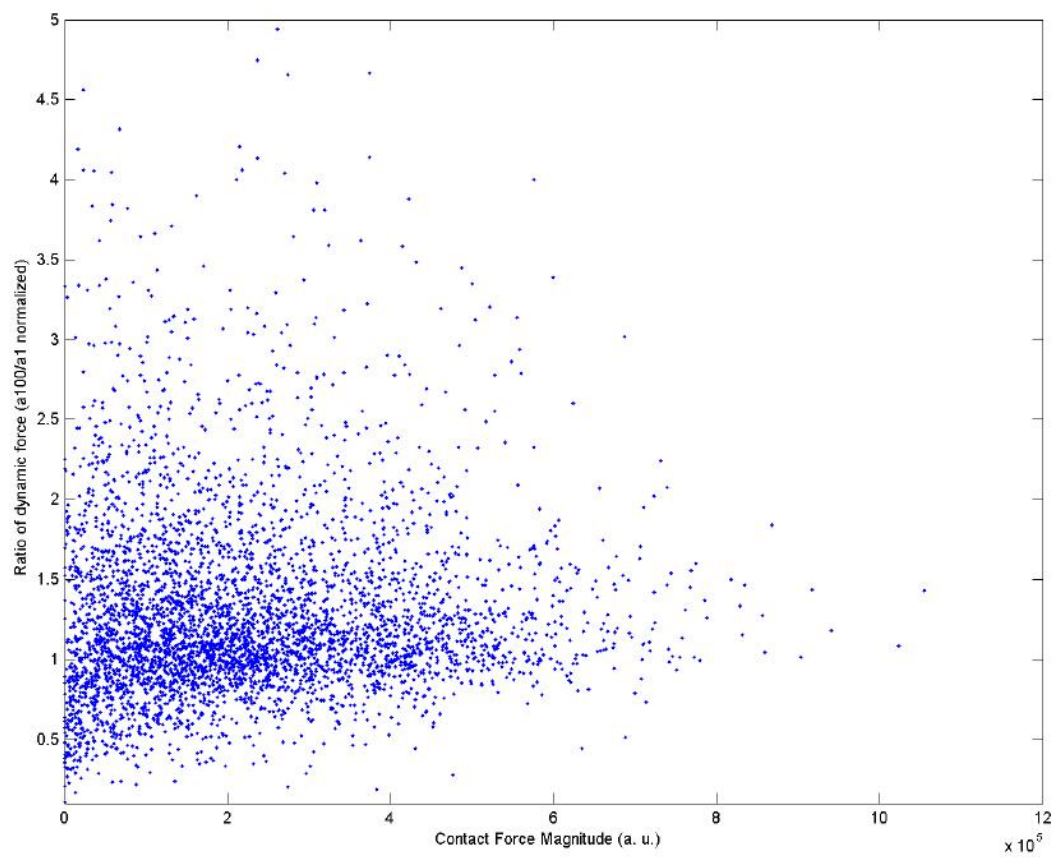


Figure 6.8: A_{100}/A_1

Bibliography

- [1] T. Baumberger A. Cochard, L. Bureau. Stabilization of frictional sliding by normal load modulation. *Trans. ASME*, 70:220–226, 2003.
- [2] F. F. Abraham. *Some new Directions in science on computers*. World Scientific, 1997.
- [3] T. L. Anderson. *Fracture mechanics: Fundamentals and applications*. CRC Press, 1995.
- [4] M. I. Baskes. Application of the embedded-atom method to covalent materials: A semiempirical potential for silicon. *PHYSICAL REVIEW LETTERS*, 59:2666–2669, 1987.
- [5] Martin Z. Bazant, Efthimios Kaxiras, and J. F. Justo. Environment-dependent interatomic potential for bulk silicon. *PHYSICAL REVIEW B*, 56:8542–8552, 1997.
- [6] T. S. Majmudar & R. P. Behringer. Contact force measurements and stress-induced anisotropy in granular materials. *Nature*, 435:1079–1082, 2005.
- [7] N. Bernstein and D. Hess. Multiscale simulations of brittle fracture and the quantum-mechanical nature of bonding in silicon. *Mat. Res. Soc. Symp. Proc.*, 653:Z2.7.1–Z2.7.6, 2001.
- [8] B. Bhushan, editor. *Modern Tribology Handbook*. CRC Press, 2001.
- [9] Michael L. Blanpied Brian D. Kilgore and James H. Dieterich. Velocity dependent friction of granite over a wide range of conditions. *GEOPHYSICAL RESEARCH LETTERS*, 20:903–906, 1993.

- [10] Michael J. Buckingham. Theory of acoustic attenuation, dispersion, and pulse propagation in unconsolidated granular material including marine sediments. *J. Acoust. Soc. Am.*, 102:2579–2596, 1997.
- [11] Andreas A. Polycarpou Chul-Hee Lee. Static friction experiments and verification of an improved elastic-plastic model including roughness effects. *Trans. ASME*, 129:754–760, 2007.
- [12] Murray S. Daw and M. I. Baskes. Semiempirical, quantum mechanical calculation of hydrogen embrittlement in metals. *PHYSICAL REVIEW LETTERS*, 50:1285–1288, 1983.
- [13] S. M. Day. Efficient simulation of constant q using coarse-grained memory variables. *Bulletin of the Seismological Society of America*, 88:1051–1062, 1998.
- [14] James H. Dieterich. Time-dependent friction in rocks. *JOURNAL OF GEOPHYSICAL RESEARCH*, 77:3690–3697, 1972.
- [15] James H. Dieterich. Modeling of rock friction 1 experimental results and constitutive equations. *JOURNAL OF GEOPHYSICAL RESEARCH*, 85:2161–2175, 1979.
- [16] JAMES H. DIETERICH and BRIAN D. KILGORE. Direct observation of frictional contacts: New insights for state-dependent properties. *PAGEOPH*, 143:283–302, 1994.
- [17] Duncan Dowson. *History of Tribology, 2nd Edition*. Wiley, 1998.
- [18] Jacco H. Snoeijer Martin van Hecke Ellak Somfai, Jean-Noel Roux and Wim van Saarloos. Elastic wave propagation in confined granular systems. *PHYSICAL REVIEW E*, 72:021301, 2005.
- [19] R A Rafey Farid F Abraham, D Brodbeck and W E Rudge. Instability dynamics of fracture: A computer simulation investigation. *PHYSICAL REVIEW LETTERS*, 73:272–275, 1994.
- [20] Richard P. Feynman. *The Feynman Lectures on Physics*. Addison Wesley Longman, 1970.

- [21] L. H. Seeley K. H. Kim E. A. Behne S. Zaranek B. D. Chapman S. M. Heald G. T. Seidler, G. Martinez and D. L. Brewster. Granule-by-granule reconstruction of a sandpile from x-ray microtomography data. *PHYSICAL REVIEW E*, 62:8175–8181, 2000.
- [22] E. E. Gdoutos. *Fracture Mechanics, an introduction*. Springer, 2005.
- [23] Eri Stendahl Gerde. *Fracture and Friction*. PhD thesis, The University of Texas at Austin, 2001.
- [24] Eric Gerde and M. Marder. Friction and fracture. *Nature*, 413:285–288, 2001.
- [25] Bruno Gilles and Christophe Coste. Low-frequency behavior of beads constrained on a lattice. *PHYSICAL REVIEW LETTERS*, 90:174302, 2003.
- [26] David L. Goldsby Terry E. Tullis Giulio Di Toro. Friction falls towards zero in quartz rock as slip velocity approaches seismic rates. *Nature*, 427:436–439, 2004.
- [27] A. A. Griffith. The phenomena of rupture and flow in solids. *Philosophical Transactions of the Royal Society of London A*, 221:163–198, 1921.
- [28] A. A. Griffith. The theory of rupture. *Proceedings of First International Congress of Applied Mechanics*, UNKNOWN:55–63, 1924.
- [29] S. P. Gross. *Dynamics of Fast Fracture*. PhD thesis, University of Texas at Austin, 1995.
- [30] R. A. Guyer, K. R. McCall, and G. N. Boitnott. Hysteresis, discrete memory, and nonlinear wave propagation in rock a new paradigm. *PHYSICAL REVIEW LETTERS*, 74:3491–3494, 1995.
- [31] Robert A. Guyer and Paul A. Johnson. Nonlinear mesoscopic elasticity: Evidence for a new class of materials. *Physics Today*, April:30–36, 1999.
- [32] Jen Andreas Hauch. *Dynamic Fracture in Brittle Materials*. PhD thesis, University of Texas at Austin, 1998.
- [33] H. Hertz. unknown. *J. reine angew. Math.*, 92:156–171, 1881.

- [34] Dominic Holland and M. Marder. Ideal brittle fracture of silicon studied with molecular dynamics. *PHYSICAL REVIEW LETTERS*, 80:746–749, 1998.
- [35] Dominic Holland and Michael Marder. Cracks and atoms. *ADVANCED MATERIALS*, 11:793–806, 1999.
- [36] Uri Lev Ilan Beery and Dov Sherman. On the lower limiting velocity of a dynamic crack in brittle solids. *JOURNAL OF APPLIED PHYSICS*, 93:2429–2434, 2003.
- [37] Inglis. Stresses in a plate due to the presence of cracks and sharp corners. *Transactions of the Institution of Naval Architects*, 55:219–230, 1913.
- [38] G. R. Irwin. Analysis of stresses and strains near the end of a crack traversing a plate. *Journal of Applied Mechanics*, 24:361–364, 1957.
- [39] M. I. Baskes J. G. Swadener and M. Nastasi. Molecular dynamics simulation of brittle fracture in silicon. *PHYSICAL REVIEW LETTERS*, 89:085503, 2002.
- [40] H Peerhossaini D. Bideau J. Lemaitre, A. Gervois and J. P. Troadec. An air table designed to study two-dimensional disc packings: preliminary tests and first results. *J. Phys. D: Appl. Phys.*, 23:1396–1404, 1990.
- [41] Francisco Guinea John Ferrante James H. Rose, John R. Smith. Universal features of the equation of state of metals. *PHYSICAL REVIEW B*, 29:2963–2969, 1984.
- [42] M. P. Marder Jens A. Hauch, Dominic Holland and Harry L. Swinney. Dynamic fracture in single crystal silicon. *PHYSICAL REVIEW LETTERS*, 82:3823–3826, 1999.
- [43] D. Gourdon M. Ruths J. N. Israelachvili Jianping Gao, W. D. Luedtke and Uzi Landman. Frictional forces and amontons law: From the molecular to the macroscopic scale. *J. Phys. Chem. B*, UNKNOWN:15, 2003.
- [44] K. L. Johnson. *Contact Mechanics*. Cambridge University Press, 1987.
- [45] Paul A. Johnson and Xiaoping Jia. Nonlinear dynamics, granular media and dynamic earthquake triggering. *Nature*, 437:871–874, 2005.
- [46] T. Johnson. Time dependent friction of granite: Implications for pre-cursory slip on faults. *JOURNAL OF GEOPHYSICAL RESEARCH*, 86:6017–6028, 1981.

- [47] David A. Kessler. A new crack at friction. *Nature*, 413:260–261, 20 SEPTEMBER 2001.
- [48] A. M. Khilla. Optimum continuous microstrip tapers are amenable to computer-aided design. *Microwave Journal*, unknown:221–224, 1983.
- [49] Alick C. Kibblewhite. Attenuation of sound in marine sediments: A review with emphasis on new low-frequency data. *J. Acoust. Soc. Am.*, 86:716–738, 1989.
- [50] Lior Kogut and Izhak Etsion. A static friction model for elastic-plastic contacting rough surfaces. *Journal of Tribology*, 126:34–40, 2004.
- [51] J. Kohanoff. *Electronic Structure Calculations for Solids and Molecules: Theory and Computational Methods*. Cambridge University Press, 2006.
- [52] J. Krim. Friction at macroscopic and microscopic length scales. *Am. J. Phys.*, 70:890–897, 2002.
- [53] G. MacDonald L. Knopoff. Attenuation of small amplitude stress waves in solids. *Reviews of Modern Physics*, 30:1178–1192, 1958.
- [54] Anthony D. Rosato Laurent Labous and Rajesh N. Dave. Measurements of collisional properties of spheres using high-speed video analysis. *PHYSICAL REVIEW E*, 56:5717–5725, 1997.
- [55] B. Lawn. *Fracture in Brittle Solids*. Cambridge University Press, 1993.
- [56] A. E. H. Love. *Treatise on the Mathematical Theory of Elasticity*. Cambridge University Press, 1927.
- [57] M. Urbakh M. G. Rozman and J. Klafter. Stick-slip motion and force fluctuations in a driven two-wave potential. *PHYSICAL REVIEW LETTERS*, 77:683–686, 1996.
- [58] D. H. Johnston M. N. Toksoz and A. Timur. Attenuation of seismic waves in dry and saturated rocks: I. laboratory measurements. *GEOPHYSICS*, 44:681–690, 1979.
- [59] Valentina Agostini Macro Scalerandi and Paul A. Johnson Pier Paolo Delsanto, Koen Van Den Abeele. Local interaction simulation approach to modelling nonclassical non-linear elastic behavior in solids. *J. Acoust. Soc. Am.*, 113:3049–3059, 2003.

- [60] M. Marder and Steve Gross. Origin of crack tip instabilities. *J. Mech. Phys. Solids*, 43:1–48, 1995.
- [61] M. Marder and Xiangming Liu. Instability in lattice fracture. *PHYSICAL REVIEW LETTERS*, 71:2417–2420, 1993.
- [62] Michael Marder. Energies of a kinked crack line.
- [63] MICHAEL MARDER. Molecular dynamics of cracks. *COMPUTING IN SCIENCE & ENGINEERING*, SEPTEMBER/OCTOBER:48–55, 1999.
- [64] Michael P. Marder. *Condensed Matter Physics*. Wiley-interscience, 2000.
- [65] Chris Marone. Laboratory-derived friction laws and their application to seismic faulting. *Annu. Rev. Earth Planet. Sci.*, 26:643–696, 1998.
- [66] Philip T. Metzger. Granular contact force density of states and entropy in a modified edwards ensemble. *PHYSICAL REVIEW E*, 70:051303, 2004.
- [67] Delphine Gourdon Jacob Israelachvili Michael Urbakh, Joseph Klafter. The nonlinear nature of friction. *Nature*, 430:29, 2004.
- [68] Mason W. P. Osmer T. F. Mindlin, R. D. and H. Dereciewicz. Effect of an oscillatory tangential force on contact surfaces of elastic spheres. *Proceedings of the First National Congress of Applied Mechanics*, unknown:203–228, 1952.
- [69] R. D. Mindlin. Compliance of elastic bodies in contact. *Journal of Applied Mechanics*, pages 259–268, 1949.
- [70] JULIA K. MORGAN. Particle dynamics simulations of rate- and state-dependent frictional sliding of granular fault gouge. *Pure appl. geophys.*, 161:1877–1891, 2004.
- [71] L. A. Ostrovsky and P. A. Johnson. Dynamic nonlinear elasticity in geomaterials. *RIVISTA DEL NUOVO CIMENTO*, 24:46, 2001.
- [72] Fabrice Barbe Stephane Bourles Xavier Thibault Patrick Richard, Pierre Philippe and Daniel Bideau. Analysis by x-ray microtomography of a granular packing undergoing compaction. *PHYSICAL REVIEW E*, 68:020301, 2003.

- [73] B. N. J. Persson. *Sliding Friction, Physical Properties and Applications*. Springer, 2000.
- [74] Carly M. Donahue Philip T. Metzger. Elegance of disordered granular packings: A validation of edward’s hypothesis. *PHYSICAL REVIEW LETTERS*, 94:148001, 2005.
- [75] S. J. Plimpton. Fast parallel algorithms for short-range molecular dynamics. *Journal of Computational Physics*, 117:1–19, 1995.
- [76] Lisa Patel M. Marder Robert D. Deegan, Shilpa Chheda and Harry L. Swinney. Wavy and rough cracks in silicon. *PHYSICAL REVIEW E*, 67:066209, 2003.
- [77] Andy Ruina. Slip instability and state variable friction laws. *JOURNAL OF GEOPHYSICAL RESEARCH*, 88:10359–10370, 1983.
- [78] R. J. Sanford. *Principles of Fracture Mechanics*. Pearson Education, Inc., 2003.
- [79] Gil Cohen Jay Fineberg Shmuel M. Rubinstein. Detachment fronts and the onset of dynamic friction. *Nature*, 430:1005–1009, 2004.
- [80] Leonid I. Slepyan. Dynamics of a crack in a lattice. *Sov. Phys. Dokl.*, 26:538–540, 1981.
- [81] Leonid I. Slepyan. *Models and Phenomena in Fracture Mechanics*. Springer, 2002.
- [82] Frank H. Stillinger and Thomas A. Weber. Computer simulation of local order in condensed phases of silicon. *PHYSICAL REVIEW B*, 31:5262–5271, 1985.
- [83] Robert D. Stoll and Robert E. Houtz. Attenuation measurement with sonobuoys. *J. Acoust. Soc. Am.*, 73:163–172, 1983.
- [84] M. Saadatfar T. Aste and T. J. Senden. Geometrical structure of disordered sphere packings. *PHYSICAL REVIEW E*, 71:061302, 2005.
- [85] H.J. Herrmann T. PÄoschel. A simple geometrical model for solid friction. *Physica A*, 198:441–448, 1993.
- [86] F. P. Bowden; D. Tabor. The area of contact between stationary and between moving surfaces. *Proceedings of the Royal Society of London. Series A, Mathematical and Physical Sciences*, 169:391–413, 1939.

- [87] Peter A. Thompson and Mark O. Robbins. Origin of stick-slip motion in boundary lubrication. *Science*, 250:792–794, 1990.
- [88] Christiane Caroli Tristan Baumberger and Olivier Ronsin. Self-healing slip pulses along a gel/glass interface. *PHYSICAL REVIEW LETTERS*, 88:075509, 2002.
- [89] Martin van Hecke. A tale of tails. *Nature*, 435:1041–1042, 2005.
- [90] L. R. Walker and N. Wax. Non-uniform transmission lines and reflection coefficients. *Journal of Applied Physics*, 17:1043–1045, 1946.
- [91] Martin H. Müser Ludgar Wenning and Mark O. Robbins. Simple microscopic theory of amontons laws for static friction. *PHYSICAL REVIEW LETTERS*, 86:1295–1298, 2001.
- [92] B. Velicky X. Jia, C. Caroli. Ultrasound propagation in externally stressed granular media. *PHYSICAL REVIEW LETTERS*, 82:1863–1866, 1999.
- [93] Hepeng Zhang Zhiping Yang and Michael P. Marder. Dynamics of static friction between steel and silicon. *Proceedings of National Academy of Sciences (PNAS)*, 105:13264–13268, 2008.

Vita

Zhiping Yang was born on October 26th, 1979 in Shanghai, China. He is the first son of Jinming Yang and Weiqiu Wang. He received his high school diploma from SongJiang No. 2 Senior High School in 1998. He spent his freshman year in Fudan University. He went to City University of Hongkong with full scholarship support from Jockey Club of Hongkong and acquired his Bachelors of Science in Applied Physics with first class honor in 2002. From fall 2002, he began graduate school at the University of Texas at Austin pursuing a Ph. D. in Physics. On June 8th of 2002, he engaged with Hongwei Shi before he left China. He married her on August 1st, 2004. Steven, his first son was born on May 26th, 2006.

Permanent Address: No. 1086, Jinwei Group 2, Jinshanwei Zheng, Jinshan Qu,
Shanghai, China, 201512

This dissertation was typeset with $\text{\LaTeX}2_{\epsilon}$ ¹ by the author.

¹ $\text{\LaTeX}2_{\epsilon}$ is an extension of \LaTeX . \LaTeX is a collection of macros for \TeX . \TeX is a trademark of the American Mathematical Society. The macros used in formatting this dissertation were written by Dinesh Das, Department of Computer Sciences, The University of Texas at Austin, and extended by Bert Kay, James A. Bednar, and Ayman El-Khashab.